NTNU – Trondheim
Norwegian University of
Science and Technology

Deformasjon av trykksatte rørledninger

Espen Jakobsen

Master of Science in Mechanical Engineering
Submission date: December 2013
Supervisor: Tore Børvik, KT
Co-supervisor: Martin Kristoffersen, KT
Magnus Langseth, KT

Norwegian University of Science and Technology
Department of Structural Engineering

Department of Structural Engineering
Faculty of Engineering Science and Technology
NTNU- Norwegian University of Science and Technology

ACCESSIBILITY

OPEN

MASTER THESIS 2013

SUBJECT AREA:	DATE:	NO. OF PAGES:
Computational Mechanics	30 December 2013	12+100+5

TITLE:

Deformation of Pressurized Pipelines

Deformasjon av trykksatte rørledninger

BY:

Espen Jakobsen

SUMMARY:
Offshore pipelines may be subjected to impact by anchor and trawl gear. An anchor impact will drag the pipeline out of its position, before it is released and the pipe straightens, due to the rebound and large axial forces. Damage and fracture may occur due to the highly complex stress and strain history in the pipe. This thesis is a continuation of work carried out in previous master theses on the subject and a part of an ongoing research program at SIMLab (NTNU) and Statoil ASA.

Three pipes were deformed quasi-statically with different horizontal loads applied in the stretch bending rig at SIMLab. A deformation rate of 25 mm/min was applied. A visual inspection after bending could not reveal any cracks.

An isotropic hardening material model was used as input for the numerical simulations in Abaqus/Explicit by the use of the SIMLab Material Model. A very good fit in the global response could be seen when comparing the numerical simulations with the corresponding experiments. When checking the strain evolution for the critical elements, a plastic hinge could be seen. It could also be seen that the largest strains were smaller in pipes with horizontal load compared to pipes without horizontal load.

Digital Image Correlation was utilized to validate the numerical simulations, by comparing strains close to the indentation zone. This gave a reasonably well compliance.

RESPONSIBLE TEACHER: Tore Børvik

SUPERVISOR(S): Tore Børvik, Martin Kristoffersen, Magnus Langseth

CARRIED OUT AT: Norwegian University of Science and Technology (NTNU)

Institutt for konstruksjonsteknikk
Fakultet for ingeniørvitenskap og teknologi
NTNU- Norges teknisk- naturvitenskapelige universitet

TILGJENGELIGHET

ÅPEN

MASTEROPPGAVE 2013

FAGOMRÅDE:	DATO:	ANTALL SIDER:
Beregningsmekanikk	30 Desember 2013	12+100+5

TITTEL:

Deformasjon av trykksatte rørledninger

Deformation of Pressurized Pipelines

UTFØRT AV:

Espen Jakobsen

SAMMENDRAG:
En offshore rørledning kan bli utsatt for støt og påvirkning fra anker og trålutstyr . Et anker kan ha den innvirkningen på et rør at det fester seg, for dermed å dra røret ut av posisjon før det løsner. Da vil store aksielle krefter føre til at røret retter seg opp. På grunn av en svært kompleks spennings- og tøyningshistorie ved en slik hendelse, kan skader og brudd oppstå. Dette kan bli svært kostbart og skadelig for miljøet. Denne oppgaven er en videreføring av arbeidet som har blitt utført i tidligere masteroppgaver på dette emnet. Oppgaven er en del av et pågående forskningsprogram ved SIMLab (NTNU) og Statoil ASA

Tre rør ble deformert kvasi-statisk i strekkbøyeriggen ved SIMLab med ulike horisontale laster. Deformasjonshastigheten var 25 mm/min. Ved en visuell inspeksjon etter bøying var det ikke tegn til utvendige sprekker.

En material modell med isotropisk fastning ble brukt som input til de numeriske simuleringene som ble utført i Abaqus/Explicit. SIMLab Material Model ble brukt for å implementere material modellen til Abaqus/Explicit. Når man sammenlignet de numeriske simuleringene med de tilsvarende eksperimentelle testene, var det en meget god likhet i global respons. Utviklingen for tøyningen i de kritiske elementene ble observert til å bevege seg som en «plastic hinge», etterhvert som deformasjonen fant sted. Det ble også observert at maksimal tøyning var høyere i rør uten horisontal last kontra rør med påført horisontal last.

«Digital Image Correlation» ble brukt til å validere de numeriske simuleringene, ved å sammenligne tøyningene ved rørets midtpunkt på bøyesiden. Dette ga et rimelig godt samsvar.

FAGLÆRER: Tore Børvik

VEILEDER(E): Tore Børvik, Martin Kristoffersen, Magnus Langseth

UTFØRT VED: Norges Teknisk Naturvitenskapelige Universitet (NTNU)

Institutt for konstruksjonsteknikk

FAKULTET FOR INGENIØRVITENSKAP OG TEKNOLOGI
NTNU – Norges teknisk-naturvitenskapelige universitet

MASTER THESIS 2013

for

Espen Jakobsen

Deformation of pressurized pipelines

Deformasjon av trykksatte rørledninger

Etter diskusjon med norsk offshoreindustri så er det et behov for ny kompetanse innen oppførsel, modellering og design av konstruksjoner på havbunnen utsatt for støtlaster fra blant annet tråll og fallende gjenstander. Metallurgiske undersøkelser har vist at slike støt kan medføre brudd i rørveggen der objektet treffer, noe som kan være vanskelig å oppdage. Slike brudd kan gi store økonomiske og miljømessige konsekvenser. I denne master-oppgaven skal deformasjon av rørledninger som et resultat av støtlaster studeres ved å gjøre idealiserte forsøk på trykksatte rør i en ny testrigg utviklet til dette formålet. Forsøkene skal utføres i kombinasjon med numeriske beregninger. Gode modeller vil kunne si noe om sannsynligheten for brudd, og her vil noe av hovedfokuset i arbeidet ligge. Oppgaven er en del av et pågående forskningsarbeid ved SFI SIMLab.

Oppgaven kan inneholde følgende aktiviteter:

1. Litteraturstudium: Tidligere arbeider på støt-på-rør, regelverk, ulike numeriske metoder og modeller, material- og bruddmodeller.
2. Laboratorieforsøk: En ny testrigg skal benyttes for å gjøre idealiserte forsøk på rør med og uten indre overtrykk. I denne oppgaven vil kun rør uten indre overtrykk testes. Forsøkene skal senere brukes til validering av numeriske simuleringer.
3. Materialforsøk: Nødvendige materialdata fra tidligere masteroppgaver skal framskaffes med tanke på kalibrering av egnet materialmodell for FE analyser.
4. Numeriske analyser: Ikke-lineære analyser av forsøkene skal utføres ved bruk av ulike numeriske modeller.
5. Validering og rapportering: Simuleringene skal valideres mot forsøksdata.

Besvarelsen organiseres i henhold til gjeldende retningslinjer.

Veileder(e): Tore Børvik, Magnus Langseth og Martin Kristoffersen

Besvarelsen skal leveres til Institutt for konstruksjonsteknikk innen 31.12. 2013.

NTNU, 30. august, 2013

Tore Børvik
Faglærer

Acknowledgements

I want to thank Professor Tore Børvik and PhD Candidate Martin Kristoffersen that have been my supervisors during this master's thesis. Their guidance and support through weekly meetings have been very appreciated. They have allways been very eager to help me and it has never been any problem to get help during my work with the thesis.

The experimental testing were carried out with great help from Trond Auestad. Big thanks to him and Tore Wisth who prepared the pipes for the testing. Håvard Ilstad is acknowledged for providing the pipe specimens to the experimental testing.

A great thank to Egil Fagerholt for helping out with the Digital Image Correlation. He was of great support both for carrying out DIC measurements during the experiments and for the guidance with the in-house DIC software. I would also like to acknowledge the help from David Morin with the SIMLab Metal Model and its implementation to Abaqus/Explicit.

Fredrikstad, December 30, 2013

Espen Jakobsen

Abstract

In this thesis, deformation of offshore pipelines have been studied. As a pipeline may be subjected to impact or anchor hooking, it can be dragged out of position, creating a complex stress and strain history in the pipe. This can in worst case lead to fracture. This thesis is a continuation of work carried out in previous theses on the subject, and part of an ongoing research program at between SIMLab and Statoil ASA.

It was performed quasi-static deformation of three scaled pipes applied to various horizontal loads in a stretch bending rig at SIMLab, Department of Structural Engineering, NTNU. A deformation rate of 25 mm/min were applied. No cracks were detected by visual inspection.

Numerical simulations with shell elements were carried out in Abaqus/Explicit to recreate the experiments. An isotropic hardening material model calibrated in a previous thesis was implemented by the use of SIMLab Material Model. A very good agreement could be seen when comapring the global response from the simulations and experiments.

When the strain evolution in the most critical elements were examined, a plastic hinge could be seen. It could also be observed that the largest strains were smaller in pipes with horizontal loading applied, than for pipes without horizontal loading. A reasonably well compliance was seen when comparing strains from numerical simulations and Digital Image Correlation.

Contents

Chapter 1

Background and Motivation

On 1^{st} November 2007 Statoil ASA discovered that an anchor had dragged a gas pipeline at the Kvitebjørn oil field out of its original position, which can be seen in Figure 1.1. The production was shut down, before it reopened in January 2008 after Statoil found it safe to run production temporarily until a scheduled maintenance in 2009. However, in August 2008 a small gas leak was found during a routine inspection, and the operation of the Kvitebjørn field was immediatly shut down [1]. It reopened in January 2009 after being repaired.

This scenario, which is of highly interest, is when a pipeline is exposed to an impact by a hooking object and then dragged out of its position along the seabed. This means that large axial forces will occur in the pipe, so when the object detach, the pipeline will straighten up, due to rebound and the axial forces. A scenario like this will make the material undergo a complex strain and stress history, which in worst case can lead to damage and failure of the pipe.

Guidelines on how to design pipelines in areas with possibility of impact between trawl gear and pipelines have been worked out by Det Norske Veritas (DNV). A missing part in these guidelines is that they dont say anything about the residual strength in a pipeline subjected to damage, and especially the case when the trawl gear gets stuck under the pipe and the pipe gets dragged out of its position. It is therefore of interest to gain more knowledge about the residual strengt in offshore pipelines, as a failure is both expensive and a risk for the surrounding environment.

The accident at the Kvitebjørn oil field and the interest from the offshore industry to get better knowledge of impact on offshore pipelines have motivated this thesis, which is an ongoing research programme at the Structural Impact Laboratory (SIMLab) at NTNU in collaboration with Statoil ASA.

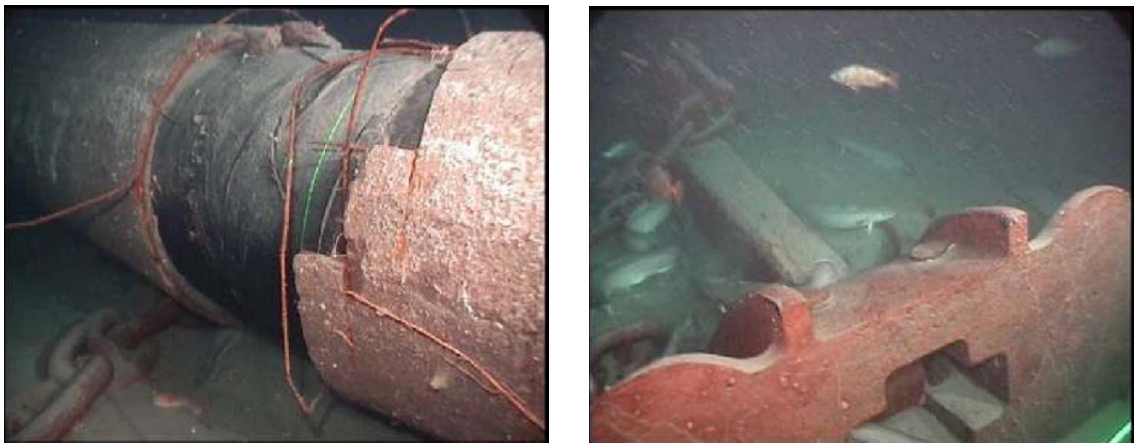

(a) Pipeline after impact. *(b) The anchor that dragged the pipeline.*

Figure 1.1: The impact on a pipeline at Kvitebjørn oil field [2].

The work in this thesis is a continuation of four previous master thesis [3, 4, 5, 6]. The first thesis on this subject was written by Slåttedalen and Ørmen [3]. As the scenario with the pipeline at Kvitebjørn is a very complex event, it was necessary to simplify the problem, making it is possible to carry out experimental testing.

It was therefore decided to split the event into one dynamic step and one stretch step. Then the experimental testing could be conducted on these two steps, independently. For the material X65 they conducted uniaxial tension test and dynamic tests so an isotropic hardening material model and a fracture criterion could be established. The numerical simulations showed a good compliance for the impact step, but the numerical simulations failed to recrate the stretch step.

Further, Fornes and Gabrielsen [4] carried out tension-compression material tests, so a combined isotropic-kinematic hardening material model could be established. They also did component test on pipes filled with water. A kinematic behaviour in the X65 material was seen, but the numerical results were reasonably similar when compared to the results from Slåttedalen and Ørmen [3].

Aune and Hovdelien [5] did impact testing against empty pipes to investigate incipient fracture by subsequent metallurgical testing. They investigated the damage behavior of X65 steel at large strains. As a consequence, they did material testing at large compression before stretching to fracture. A material model based on these tests, was then established to see if the global response of the pipes could be recreated in a better way, than in the previous thesis.

Asheim and Mogstad [6] conducted quasi-static bending of pipes in the stretch bending rig, followed by stretching. Metallurgical investigations, where the main interest was incipient fracture, of the stretched pipes were carried out and compared to the impacted pipes.

Since the experimental testing carried out by Asheim and Mogstad [6] did not go quite as planned, regarding the applied horizontal loads, it was of interest to do similar testing in this thesis. So testing in the stretch bending rig on three pipes with different horizontal load was conducted. These experiments were then used to validate the numerical simulations with the material model that was obtained from Slåttedalen and Ørmen [3]. It has also been conducted a thorough review of previous work in the four earlier thesis [3, 4, 5, 6].

The outline of the thesis is given below.

Chapter 2 presents the most relevant theory that have been used in this thesis.

Chapter 3 gives a review of the most important work and research that has been carried out in the previous thesis and papers related to the work in this master thesis.

Chapter 4 presents the SIMLab Material Model with the most important theory. It also provides the theory and background for the establishment of the parameters used as input for establishing the isotropic hardening material model used in the numerical simulations. In the end the material parameters are summarized.

Chapter 5 presents the experimental setup of the stretch bending rig and bending of pipes in this. Further it has been conducted some initial strength calculations of pipes. The main part is the modeling of a basis numerical model and the different numerical simulations that have been carried out with different horizontal loading conditions. The effect of applying inner pressure to numerical models has also been looked into.

Chapter 6 summarize the measurements of the pipes. Further, a brief introduction to Digital Image Correlation (DIC), that have been utilized in the experimental testing, is given. Then a review of the experimental testing of the pipes and the results are presented.

Chapter 7 first has a comparison of the preliminary studies with the experimental testing. Then there is a parameter study, that in combination with experiments and preliminary numerical studies have been used to establish optimized numerical models for each of the three different pipes used in the experimental testing. Further, it has been carried out final numerical simulations on theseoptimized models. At last, the results from the preliminary and final simulations have been compared to the experimental results.

Chapter 2

Theory

2.1 Isotropic Hardening

As a material is deformed plastically, they will in general work-harden and thus the strength increases. To describe the evolution of the yield surface during the work-hardening, hardening rules are used. Isotropic hardening implies that the elastic region expands (while keeping its shape) in stress space during plastic deformation [7]. This can be seen in Figure 2.1.

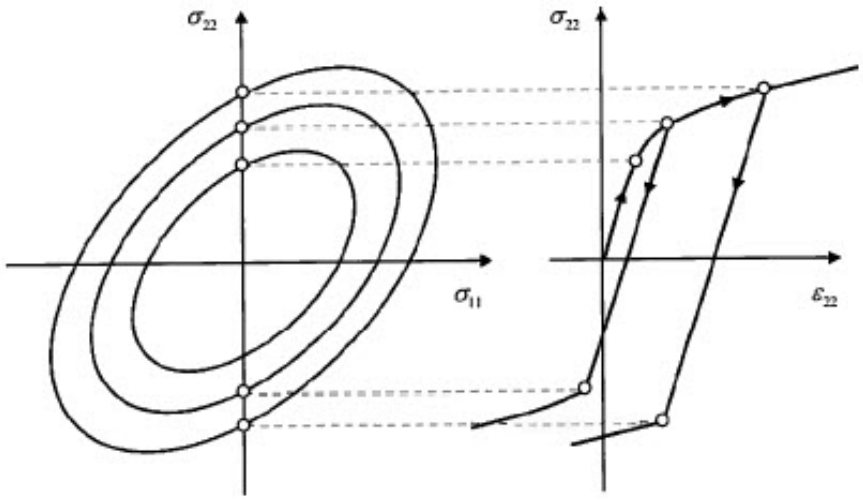

Figure 2.1: Isotropic hardening: the yield surface expands in stress space as the material work-hardens [7].

The isotropic hardening variable R, depending on the plastic strain p, is introduced to account for isotropic hardening. This variable will account for the expansion of the elastic domain as seen in Figure 2.1. So for an elastic-plastic material with isotropic

hardening the yield criterion can be expressed in the form

$$f(\sigma, R) = \varphi(\sigma) - \sigma_Y(R) = \sigma_{eq} - (\sigma_0 + R(p)) \tag{2.1}$$

where $\varphi(\sigma) = \sigma_{eq}$ is the equivalent stress and $\sigma_Y(R) = \sigma_0 + R(p)$ is the flow stress of the material. σ_0 is the initial yield stress.

Generally the isotropic hardening rule is definedon rate form as

$$\dot{R} = H_R \dot{\lambda} \tag{2.2}$$

with the assumption that the hardening modulus H_R depends somehow on the state of the material. If the associated flow rule is assumed, the equivalent plastic strain $\dot{p}$ is equal to the plastic parameter $\dot{\lambda}$.

The Power law and the Voce rule are two isotropic hardening rules given in Equation (2.3) and Equation (2.4), respectively. Here the work-hardening is defined uniquely by the equivalent plastic strain.

$$R(p) = Kp^n \tag{2.3}$$

$$R(p) = Q_i(1 - \exp^{-b_i p}) \tag{2.4}$$

where K, n, Q_i and b_i are hardening parameters determined from material tests.

2.2 Deformation of Simply Supported Thin-Walled Tubes Loaded at Midspan

The pipes in this thesis will be deformed quasi-statically and they will be compared with pipes deformed with a dynamic impact. It is therefore of interest to understand the different modes of deformation.

2.2.1 Quasi-static Deformation

Thomas et al. [8] examined the behaviour of simply supported circular tubes under the action of transverse loading of a wedge-shaped indenter, up to the point of maximum load. The test was carried out quasi-statically on simply supported aluminium tubes

with a span of 178 mm. The ratio of the initial diameter of the tube D_0 and the thickness of the tube wall T was $27 < D_0/T \leq 37$.

During the test three phases of deformation could be identified [8].

- *Pure crumpling - Phase 1*
  Initially there will be a localized crumpling of the top surface of the tube. The force will increase rapidly until the bottom of the tube will start to deflect. The associated load when this deflections begins is the maximum pure crumpling load.
- *Crumpling and bending - Phase 2*
  There will be further crumpling combined with global bending of the tube up to P_{max}. The slope of the force-displacement curve will decrease.
- *Structural collapse - Phase 3*
  When P_{max} is reached the tube will collapse. A characteristic of this phase is that the ends of the tube will have large rotations and the phase consists of pure bending of the tube. The force will decrease significantly.

The three phases can be seen in Figure 2.2.

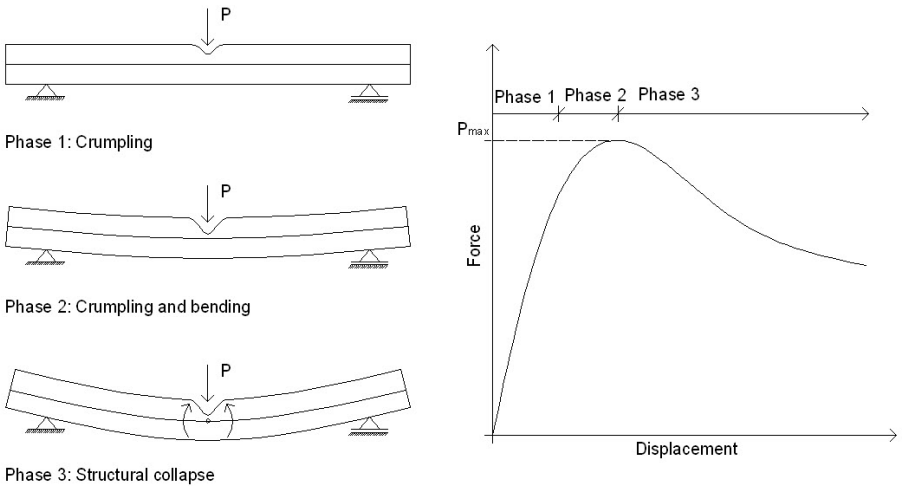

Figure 2.2: Phases of deformation [3].

2.2.2 Dynamic Impact

For the case of a dynamic impact, several studies carried out on the problem shows that the deformation progress is quite complex. The impact can be divided into two phases, namely the transient phase and global mode phase, that can be seen in Figure 2.3.

The first phase is the transient, where elastic and plastic waves travels away from the point of impact. An important factor in the transient phase is the weight of the object hitting the pipe. If the ratio between the weight of the striker and the pipe is small, will this favor the transient phase.

In the global mode, that starts when the elastic and plastic waves reach the end supports of the pipe, a global deformation of the pipe will be seen. This phase is favoured by a large striker mass compared with the mass of the pipe. In the case of a heavy striker, the transient phase can be neglected and the problem can be assumed static.

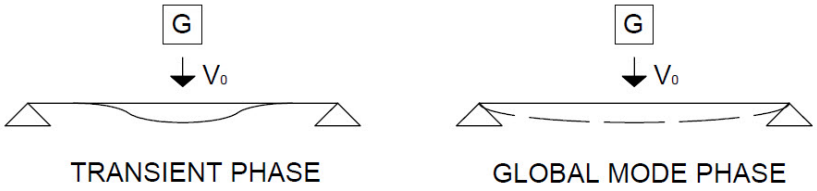

Figure 2.3: Two phases of dynamic impact [9].

Chapter 3

Previous Work

This master thesis is a continuation of four previous master theses that have been written on the topic *Impact Against Offshore Pipelines*. These master theses have been written by Slåttedalen and Ørmen [3], Fornes and Gabrielsen [4], Aune and Hovdelien [5] and Asheim and Mogstad [6] in the respective order. This chapter is mainly a presentation of the previous work that has been carried out in these theses.

The main topics that have been covered in these theses are material tests on the steel grade X65 that are used in the offshore pipelines. On the basis of these tests material models have been established. Further it has been done different component test on small scale pipes and numerical simulations have been carried out to recreate the component tests and verify the material models.

3.1 Material Tests

In the three previous theses [3, 4, 5] there has been carried out a number of different material tests. Slåttedalen and Ørmen [3] performed uniaxial quasi-static tensile tests to study the strain hardening effect and they investigated anisotropy and homogeneity in the material. They also conducted dynamic tensile tests to determine the effect of strain rates. Fornes and Gabrielsen [4] conducted uniaxial compression-tension tests and vice versa to investigate the effect of reversed loading and the possibility of kinematic hardening. Notched compression-tension tests were conducted by Aune and Hovdelien [5] to examine how large strains will influence the materials behaviour. They also performed a metallurgical investigation on the specimen from the notched compression-tension tests.

3.1.1 Quasi-Static Tensile Tests

The specimens used in the quasi-static tensile tests performed by Slåttedalen and Ørmen [3] were taken from the pipe wall at four different locations. At one location they were taken in three directions. An overview of locations and directions can be seen in Figure 3.1.

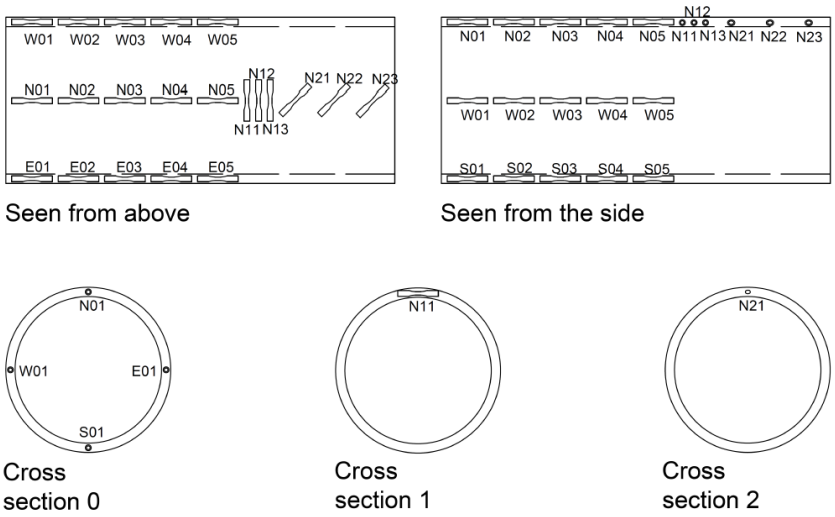

Figure 3.1: Overview of where the material test specimens were taken [3].

The quasi-static tensile tests were conducted in a deformation controlled Zwick test machine at room temperature. The rate of deformation was kept constant at 0.3 mm/min which is equal to an initial strain rate of $\dot{\varepsilon} = 10^{-3}s^{-1}$. Laser equipment was used to measure the diameter reduction in two perpendicular directions. After necking there will be a triaxial stress state in the neck and the equivalent stress σ_{eq} has to be corrected according to the Bridgman analysis [10], which is a simplified mathematical model. Figure 3.2 shows a test with the corrected equivalent stress plotted with the uncorrected stress.

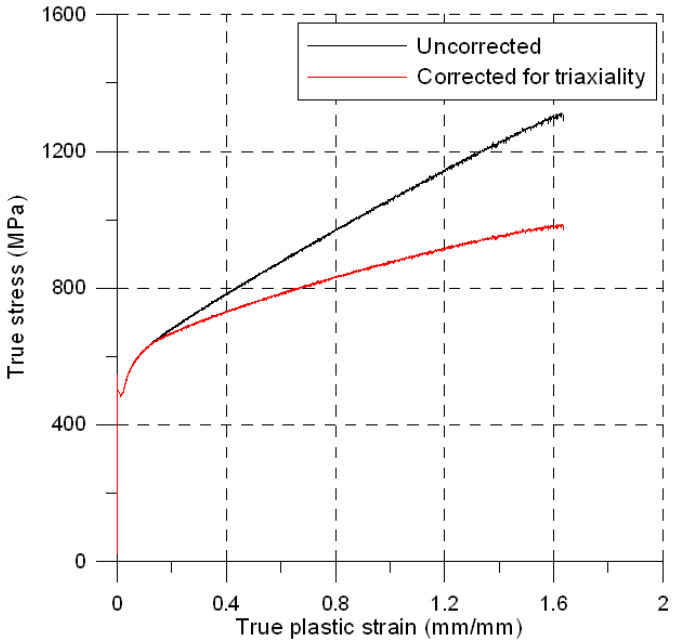

Figure 3.2: Bridgman correction of the equivalent stress [3].

There were performed two parallel test at each location to highlight any differences between the specimens. Figure 3.3a shows the true stress-true strain curves from the four different locations. It can be seen that they are almost identical, indicating that the material is homogenous over the cross-section. Figure 3.3b shows the true stress-strain curves taken in the different directions; 0°, 45° and 90° with respect to the longitudinal axis. Some small deviations can be seen, but this is insignificant when compared to some of the differences in the parallel tests that have been shown by Slåttedalen and Ørmen [3]. The material can therefore be assumed to be isotropic, an assumption that is further supported by the almost perfectly circular fracture surfaces, shown in Figure 3.4.

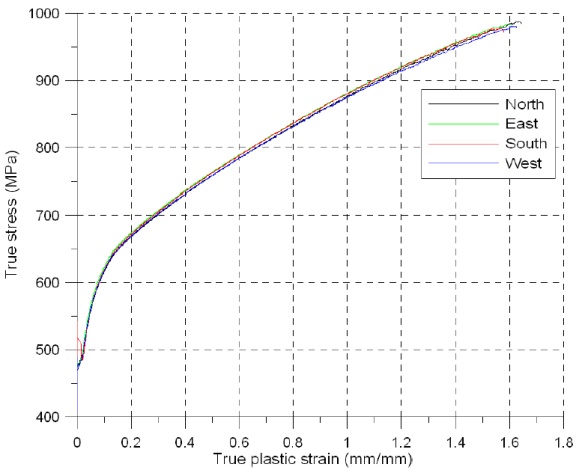

(a) Different positions of the cross-section.

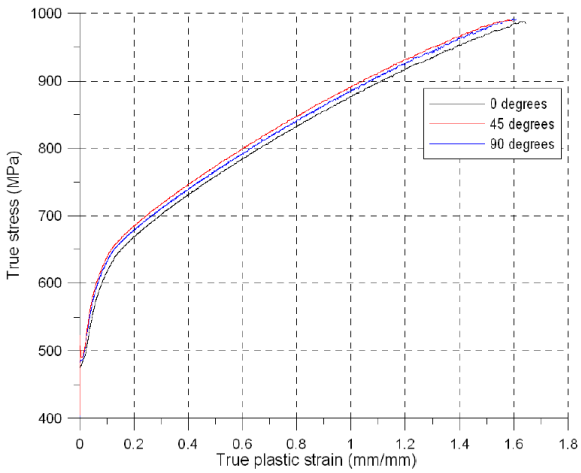

(b) Different specimen orientations.

Figure 3.3: True stress-true strain curves from specimens taken in different locations and orientations on the specimen [3].

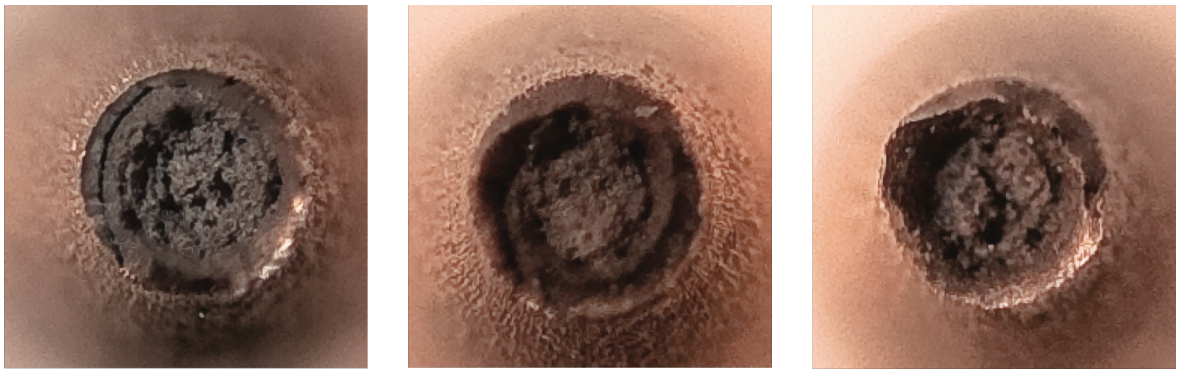

(a) 0° (b) 45° (c) 90°

Figure 3.4: Fracture surfaces on the tensile test specimen [3].

3.1.2 Dynamic Tensile Tests

Slåttedalen and Ørmen [3] performed dynamic tensile tests by using a Split-Hopkinson Tension Bar (SHTB) to obtain stress-strain curves for the material at high strain rates, making it possible to examine material behaviour at high strain rates. It was carried out two tests at three different true strain rates, namely $\dot{\varepsilon} = 240\ s^{-1}$, $\dot{\varepsilon}$ = 535 s^{-1} and $\dot{\varepsilon}$ = 830 s^{-1}. For more knowledge regarding the SHTB and the experimental setup it is referred to Slåttedalen and Ørmen [3]. Figure 3.5a shows the charachteristic curves for the different true strain rates plotted together with a quasi-static tensile test $\dot{\varepsilon}$ = 0.001 s^{-1}.

It can be seen from the curves that the flow stress, and to a certain degree, that the fracture strain is dependent on the strain rate. In Figure 3.5a it is shown that the flow stress increases when the strain rate increases, while the fracture strain is negligibly decreasing when the strain rates increase as shown in Figure 3.5b.

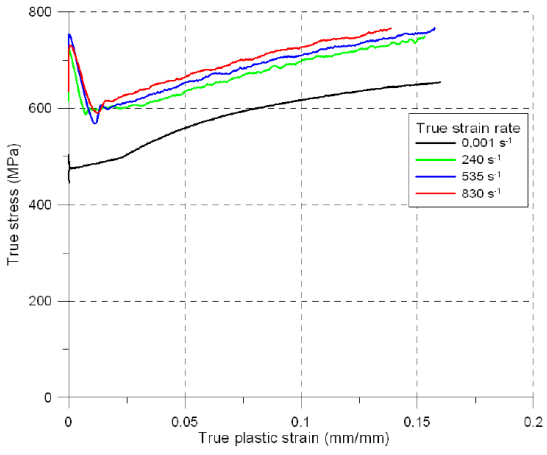

(a) Characteristic true stress-true plastic strain curves.

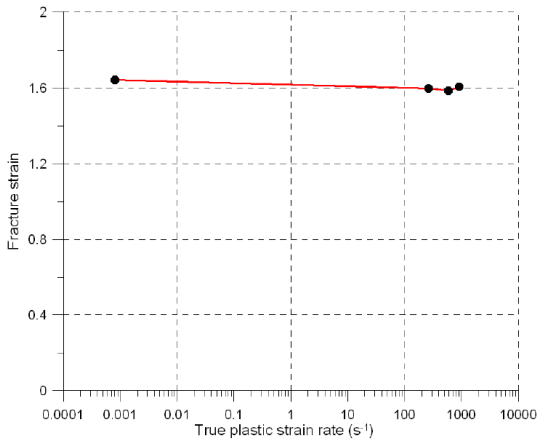

(b) Fracture strain.

Figure 3.5: The effect of increased strain rates [3].

3.1.3 Uniaxial Tests With Reversed Loading

The uniaxial tests with reversed loading were performed by Fornes and Gabrielsen [4] to examine whether it is a difference in the behaviour of the material in tension and compression. Because of the problems regarding buckling, these tests are easier to perform if tension is applied first. Since the pipes that are studied will experience compression before tension in the critical areas it is important to examine whether the material behaviour is independent of the initial direction of loading. The decision was therefore made to carry out both compression tests and tension tests with reversed loading. The machine used for performing the experiments was a Dartek 20 kN Universal testing machine. The experiments were perfomed under deformation control with a deformation rate of 0.225 mm/min, equivalent to a strain rate of $\dot{\varepsilon}$ = 5 · $10^{-4}s^{-1}$. To monitor the tendency of buckling, double-sided extensometers were applied and it was observed that the measured strains did not differ significantly. For more details regarding the experimental tests and the geometry of the specimen, see Fornes and Gabrielsen [4].

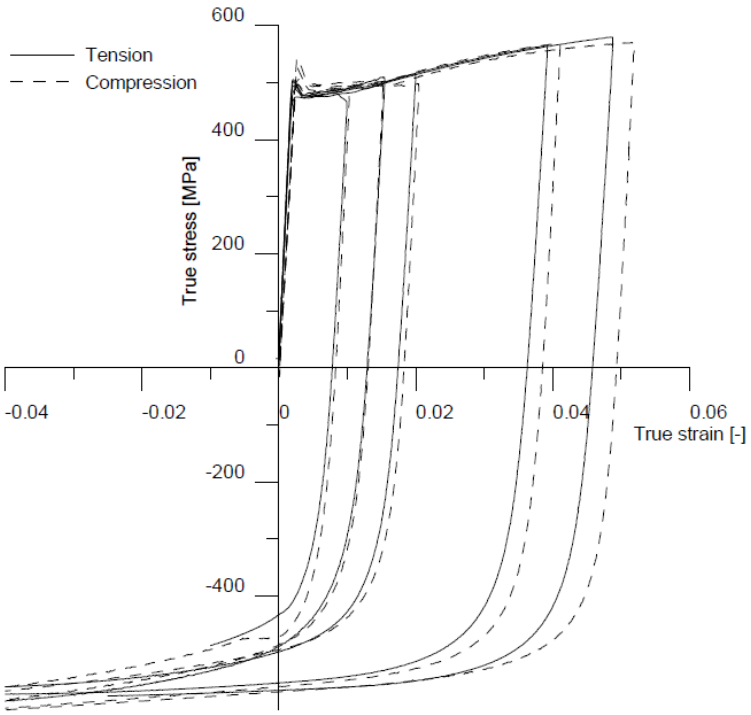

Figure 3.6: Comparison of true stress-true strain curves for initial loading in both tension and compression [4].

Figure 3.6 shows a comparison of stress-strain curves for both initial loading directions, where the curves initially loaded in tension have been multiplied by -1 to make comparison easier. No significant difference can be seen between the specimens initially loaded in tension and compression. For the largest strains, the point of unloading, and hence the reloading curves, are somewhat different. The reason for this is that the

unloading was done manually by the operator, based on the measurements from the two extensometers. It was difficult to unload at the desired largest compressive strains since the measurements from the extensometers varied. It should be pointed out that the tests were only carried out for small strains so the material behaviour is only valid up to strains of 10 %. The yield strength was found to be σ_0 = $480\ MPa$ [4], which is the average value from the experiments.

3.1.4 Notched Tests With Reversed Loading

The notched compression-tension tests with reversed roading in tension was performed by Aune and Hovdelien [5] to examine the behaviour of the material when exposed to large strains in compression. It was of interest to investigate how this influenced the fracture strain, ductility and kinematic behaviour. Reference is made to Aune and Hovdelien [5] for more information about the geometry of the specimen and experimental setup.

Two test series were conducted; the first with compression up to 40 % strain, and then reversed loading in tension until failure. The second test serie was in compression only, up to 80 % strain. In the first test series one specimen was loaded in tension to act as a reference.

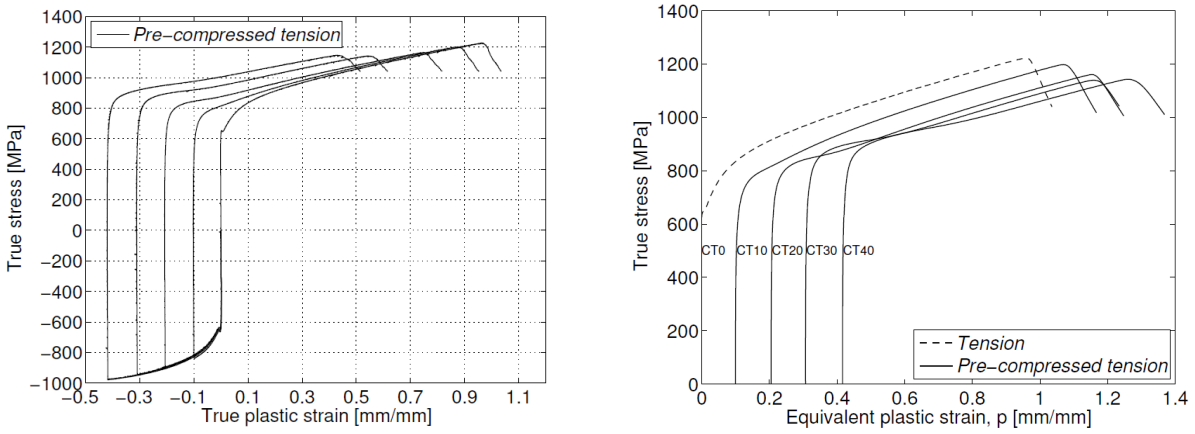

(a) Whole sequence.

(b) A close view on the tension part.

Figure 3.7: True stress - true strain for notched compression tests with reversed loading for test series 1 [5].

A distinct Bauschinger effect is clearly evident in Figure 3.7a. The Bauschinger effect is characterized by a reduction in yield stress when the material is loaded in the reverse direction (here tension) [7]. The work-hardening of the material loaded in tension after compression deviates from what was experienced in tension only. This can be seen in Figure 3.7b, which shows the true stress-true strain curves of the material in

compression-tension and tension only. In the reversed curves, a work-hardening stagnation is clearly seen, since the work-hardening rate stays below the forward one. The results from test series 2 are used for metallurgical investigation.

A test with the specimens loaded to 40 %, 60 %, 80 % and 90 % true strain in compression before stretched in tension until fracture was conducted by Kristoffersen et al. [11]. The true stress-true strain curves from this experiment can be seen in Figure 3.8. This test shows a even more significant work-hardening stagnation than what could be seen in the previous test. Especially, for the specimen loaded to 90% true strain in compression, the reduction in ductility is very evident. The mode of fracture was also altered to a 45° shear mode. A test with the specimen compressed to 100 % true strain before stretched in tension to fracture was also performed. This created a slightly barreling effect, and the specimen became widest at the centre. The fracture was 45° shear mode. Compared to the specimen in 90 % it had a much less indication of cleavage and almost entirely ductile fracture. When the specimen is widest at its centre, a shear fracture or a fracture at the cross-section with lowest area is more likely to occur. This lead to a questioning of the results from the 90 % specimen as a similar fracture mode was observed by Kristoffersen et al.[11].

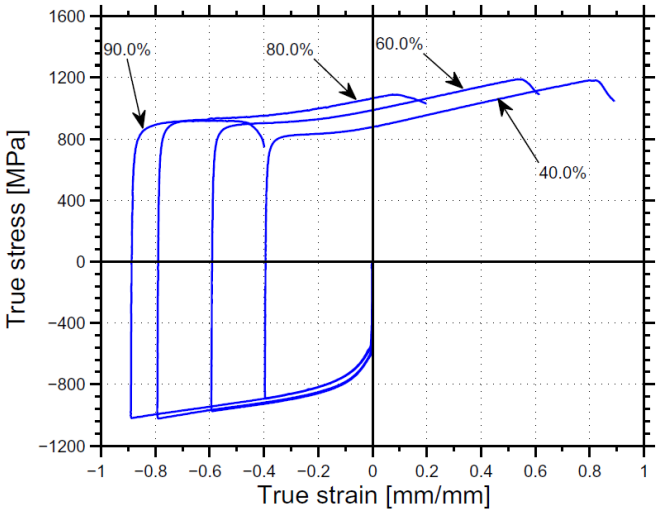

Figure 3.8: Results from the test series of notched tests with reversed loading [11].

3.1.5 Metallurgical Investigation

Aune and Hovdelien [5] studied the fracture surface and the matrix and particle composition in the material of the compression-tension test. An important finding is that at high magnification, selected particles, seen in Figure 3.9, appear to be crushed and rather large voids are surrounding them. This will lower the fracture strength of the material. They also observed that the fracture surfaces seemed relatively isotropic, which supports the results from Slåttedalen and Ørmen [3].

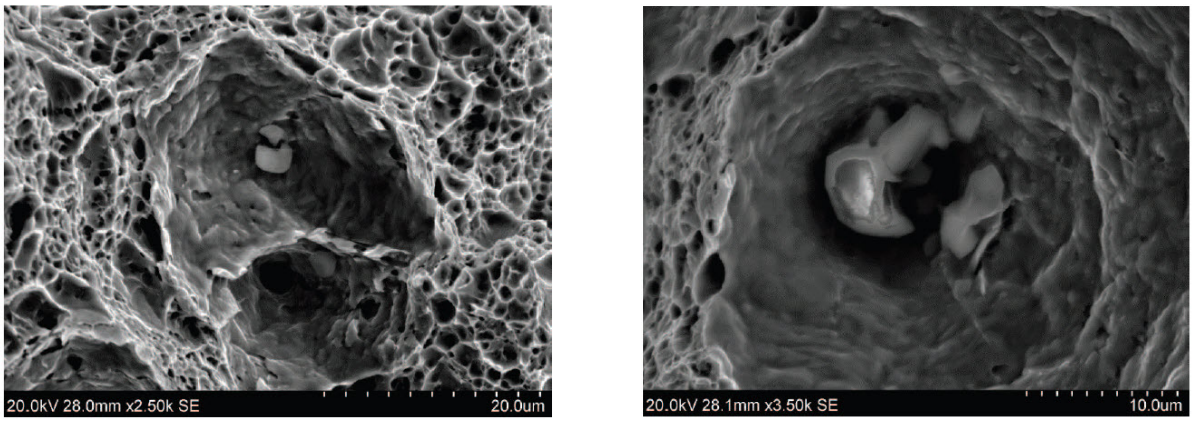

(a) Magnification x 2500.

(b) Magnification x 3500

Figure 3.9: Cracked particles for compression-tension test (40%) at different magnification levels [5].

3.2 Material Models

Calibrations of different material models and fracture criterions have been conducted by Slåttedalen and Ørmen [3], Fornes and Gabrielsen [4] and Aune and Hovdelien [5]. In this section there is a review of this work and a summary of the different parameters of the different models.

Slåttedalen and Ørmen [3] calibrated a material model based on the Johnson-Cook constitutive relation [12] with temperature dependence excluded. The strain-hardening term was calibrated by using the Bridgman corrected results from the quasi-static uniaxial tensile tests 3.1.1 by using the method of least squares. Results from the dynamic tensile tests 3.1.2 was used to calibrate the strain rate term.

Two different fracture criterions based on the Johnson-Cook fracture criterion [13] were established by Slåttedalen and Ørmen [3]. The Cockroft-Latham Johnson-Cook criterion (CL-JC) was calibrated using the results from the quasi-static uniaxial tension test while the test-based Johnson-Cook criterion (TB-JC) was calibrated based on the notched tests.

The Johnson-Cook material model calibrated by Slåttedalen and Ørmen [3] is only able to express isotropic hardening. Since the pipes experience a reversed loading in some areas, the material model might need a kinematic hardening part. Fornes and Gabrielsen [4] therefore introduced a non-linear combined isotropic-kinematic hardening material model. Material behaviour at large strains needs to be considered by the material model. Experimental tests conducted by Fornes and Gabrielsen [4] did not contain valid data for high strains, therefore test data from Slåttedalen and Ørmen [3]

was used to extend the model by extrapolating it up to failure strain. The method of least squares was used to calibrate the combined hardening material model.

Aune and Hovdelien [5] examined the combined isotropic and kinematic hardening material model calibrated by Fornes and Gabrielsen [4] by using it in numerical simulations of the compression-tension tests at large strains, as seen in Section 3.1.3. The numerical simulations revealed interesting results as both in the compression and tension step the simulations failed to recreate the load levels. A deviation between the experiments and constitutive relation in terms of the gradient at reversed loading was found, when the material model was studied closer. Aune and Hovdelien[5] therefore decided to calibrate a new material model. The calibration was based on the the results from the uniaxial tension-compression test at 5 % strain and the method of least squares. Aune and Hovdelien [5] also conducted an inverse modeling optimization in LS-OPT. An inverse modeling approach was preferred due to the triaxial stress state in the notched specimen.

An overwiev of the material parameters for the different material models are summarized in Table 3.1 and Table 3.2. The parameters for the fracture criterions are summarized in Table 3.3.

Table 3.1: Isotropic hardening material model.

Material parameters	**A**	**B**	**n**	**C**	$\dot{\varepsilon}_0$
Direct calibration [3]	465.5	410.83	0.4793	0.0104	0.000806

Table 3.2: Combined isotropic/kinematic hardening material models.

	Isotropic					Kinematic			
Material parameters	σ_0	Q_1	b_1	Q_2	b_2	C_1	γ_1	C_2	γ_2
Direct calibration [4]	330.3	703.6	0.47	50.5	34.7	115640.0	916.0	2225.0	22.0
Direct calibration [5]	310.3	35.30	223.20	846.8	0.42	67440.30	425.10	716.30	9.30
Inverse calibration [5]	299.0	160	25	400	0.25	50401	390.7	1279.0	12.8

Table 3.3: Fracture criterions.

Material parameters	D_1	D_2	D_3	D_4	D_5	$\dot{\varepsilon}_0$
Cockroft-Latham based Johnson-Cook (CL-JC) [3]	0.7	1.79	1.21	-0.00239	0	0.000806
Test Based Johnson-Cook (TB-JC) [3]	0.42	2.25	1.87	-0.00239	0	0.000806

3.3 Component Tests

Component tests have been carried out in all the four previous theses. Slåttedalen and Ørmen [3] and M. Kristoffersen [11] conducted dynamic impact, followed by stretching

of empty pipes. The same experiment were carried out on open and closed pipes filled with water by Fornes and Gabrielsen [4]. Aune and Hovdelien [5] performed dynamic impact on pipes to be able to do metallurgical investiagations of them. Quasi-static bending followed by stretching were performed by Asheim and Mogstad [6].

3.3.1 Impact and Stretching of Empty Pipes

Slåttedalen and Ørmen [3] performed component tests on four pipes, named A, B, C and D, while M. Kristoffersen [11] carried out component tests on two pipes, named E and F. The experimental testing consisted of two steps. First an impact against the pipes were conducted in the pendulum accelarator [14] at Department of Structural Engineering, NTNU, Trondheim. In the second step of the experiments the impacted pipes were stretched at Statoil's Laboratory in Trondheim.

In the impact part the pipes were simply supported with a free span of 1.0 m. The trolley used to impact the pipes had a weight of 1472 kg with an indenter radius of 10 mm [15]. A photo series of the dynamic impact on pipe A can be seen in Figure 3.11.

The stretch step was conducted quasi-statically on a standard 1200 kN Instron testing machine. For details about the experimental setup see Slåttedalen and Ørmen [3]. Impact and stretching was first performed on pipe A and B to get insight of the problem, so that the result could be used to determine the input parameters for the experiments on pipe C, D, E and F.

A comparison between the video and the data from the load cell revealed that the load cell understimated the displacement in the impact test for pipe A and B. No video was available for pipe C, so an estimate of the corrected displacement was found.

The force-displacement curves for pipes A-F are shown in Figure 3.10a and Figure 3.10b for the impact and stretch step, respectively. For pipe B and E the trolley hits the aluminum buffers before all kinetic energy has been absorbed by the pipe, therefore they have matching maximum displacement. The curves are almost identical, indicating that the dynamic effects seem to have little significance on the experiments in this velocity range.

By visual inspection during the stretch step, fracture was observed in all pipes at very different load levels.

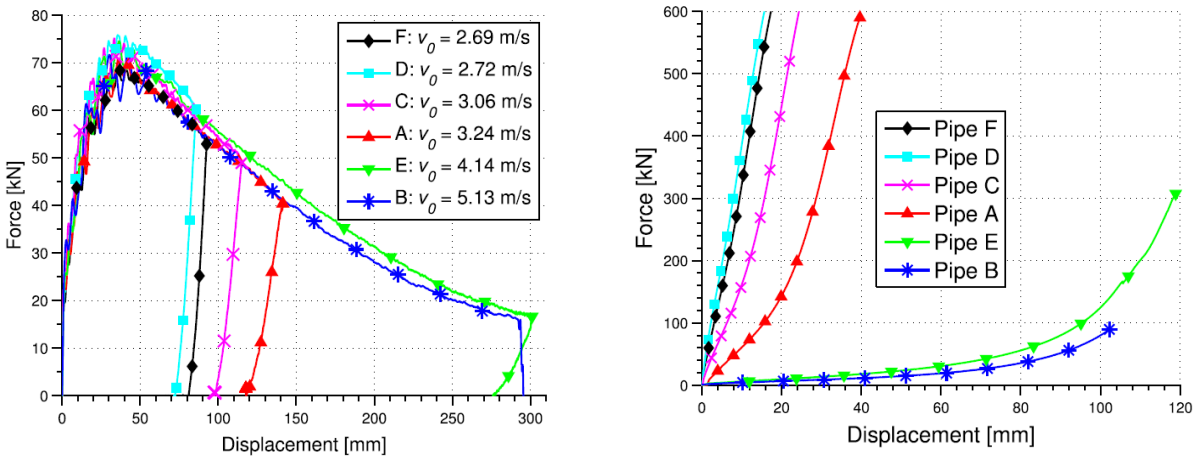

(a) Impact step. *(b) Stretch step.*

Figure 3.10: Experimental results from the impact and stretch step of the pipes A-F [11].

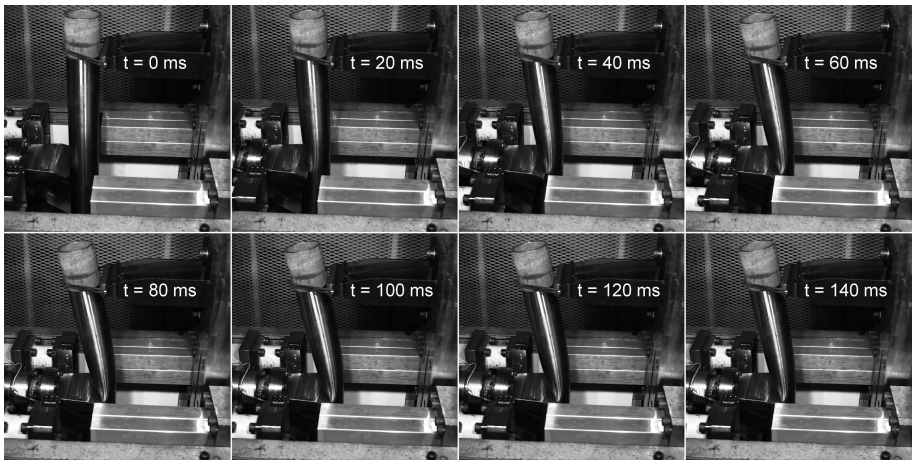

Figure 3.11: Photo series from the video capturing the impact on pipe A, v = 3.24 m/s [3].

3.3.2 Impact on Pipes Filled With Water

Fornes and Gabrielsen [4] conducted experimental impact testing on four pipes in the pendulum accelerator. Pipes named G and H were filled with water and open in the ends while pipes named I and J were filled with water and closed in the end with a membrane. A photo series of the dynamic impact on pipe I can be seen in Figure 3.12.

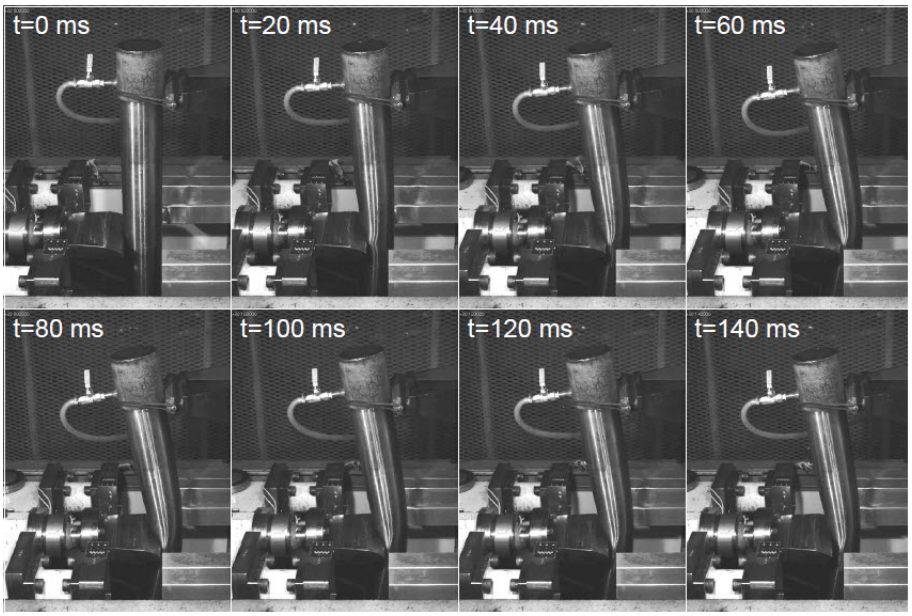

Figure 3.12: Photo series from the video capturing the impact on pipe I, v = 3.22 m/s [3].

The average thickness t_{avg} have been used to plot nondimensional force-displacement curves for the impact that excludes the effect of the thickness variation between the pipes. The plots can be seen in Figure 3.13. The contact force is lower for the pipes filled with water compared to the empty pipes, which seems illogical. Experimental inaccuracies might be a part of the explanation, but uncertainties in the thickness is probably the reason for this behaviour.

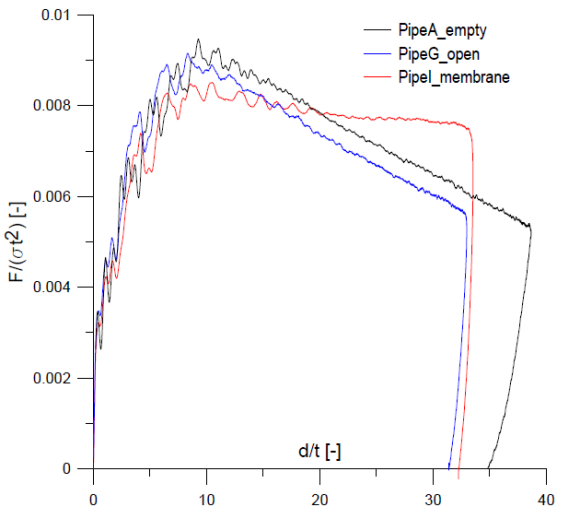

(a) Pipe A (v = 3.24 m/s), G (v = 3.21 m/s) and I (v = 3.22 m/s)

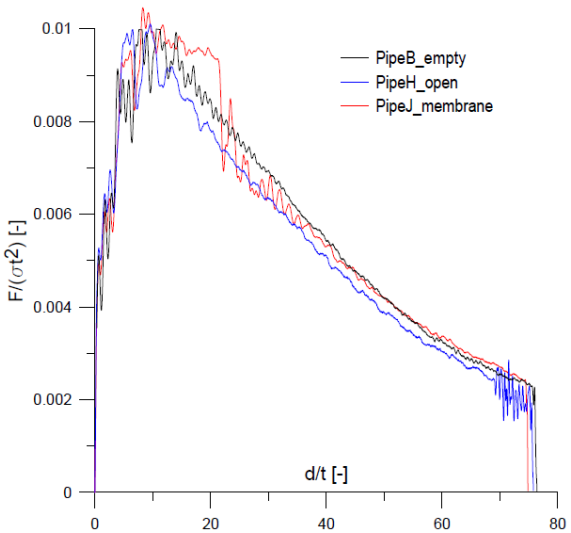

(b) Pipe B (v = 5.13 m/s) , H (v = 5.11 m/s) and J (v = 5.04 m/s).

Figure 3.13: Nondimensional force-displacement curves for all the experiments [4].

3.3.3 Bending and Stretching of Pipes

Quasi-static bending experiments of pipes were carried out by Asheim and Mogstad [6]. The experiments consisted of a bending step and a stretching step for three pipes named pipe 1, 2 and 3. The experiments were performed in a stretch bending rig, (see Section 5.1.1).

An indenter velocity of 25 mm/min was used in all experiments. Pipe 1 was bent to a vertical displacement of 282.6 mm without being subjected to any horizontal force. After bending, the pipe was stretched with a linearly increasing force up to 120.7 kN. Pipe 2 had a pre-bending horizontal stretch force of 55 kN which was kept constant throughout the bending step. It was bent to a vertical displacement of 208.1 mm. After bending, the pipe was stretched with a linearly increasing force up to 139.5 kN. The experiments on pipe 3 did not go as planned. In the bending step the pipe was supposed to be subjected to a linearly increasing force from 0 to 55 kN, instead it increased linearly with an offset of 43.9 kN from 43.9 kN to 101.9 kN. It was bent to a vertical displacement of 198.6 mm. Also, the stretch step did not go as planned as the horizontal force reached its maximum capacity almost immediately and simultaneously as the removal of the indenter. It was stretched with a force of 322.0 kN.

Figure 3.14a shows the force-vertical displacement curves for the bending step. It is seen that the larger average pipe thickness for pipe 1 may contribute more to the initial stiffness than the applied horizontal force to pipe 2.

The force-displacement path for pipe 1 after the peak force was expected since the experimental tests done in the master theses [3, 4, 5] showed similar behaviour. The force level flattens out and then increases slightly for pipe 2. The stretching of pipe 1 and 2 can be seen in Figure 3.14b.

No cracks were visible after the bending step, and some emerged during stretching.

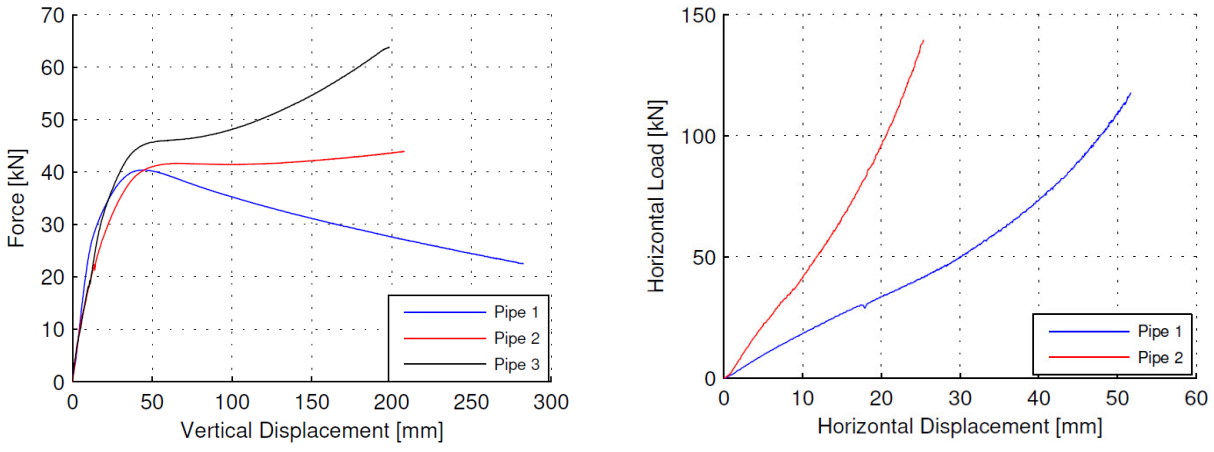

(a) Bending step. *(b) Stretch step.*

Figure 3.14: Force-vertical displacement curves for bending and stretching step [6].

3.3.4 Metallurgical Investigations

There has been carried out metallurgical investigations of the pipes that were subjected to impact followed by stretching and impact only. The pipes exposed to impact followed by stretching were obtained from Slåttedalen and Ørmen [3]. Two pipes named K and L were subjected to impact only in experiments conducted by Aune and Hovdelien [5]. The impact was carried out in the same way as Slåttedalen and Ørmen [3] did their impact testing. Asheim and Mogstad [6] performed metallurgical investigations of the pipes that were quasi-statically bent and then stretched.

Metallurgical investigations of pipe K revealed one external and one internal crack, that both ran through 75 $\%$ of the wall thickness as seen in Figure 3.15. The external crack was found in the dent where the trolley's nose hit the pipe by a macroscopic investigation while the internal crack was found at the outer edge of the dent was the surface crack were no longer visible. Pipe L had an intact surface and no internal cracks were seen, neither by visual inspection nor by optical microscope, however at higher magnification cracks of approximately length of 300 μm could be seen. Asheim and Mogstad [6] studied specimens extracted from the indentation zone, were fracture and the largest strains were observed in the previous thesis. After stretching, surface cracks were visible, and in pipe 1 and pipe 3 rather large surface cracks could be seen. The largest crack was found to be approximately 12 % of the initial thickness of pipe 3. Further metallurgical investigations showed that fracture seemed to be initiated in the bottom of the lathing groves. Photos of investigation of specimen from bend for pipe 1 can be seen in Figure 3.16.

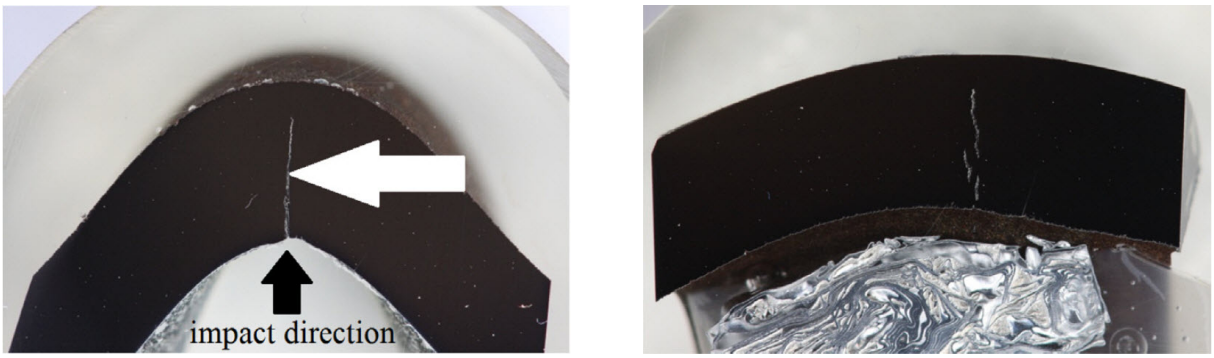

(a) External crack. *(b) Internal crack.*

Figure 3.15: External and internal crack found in pipe K subjected to an impact at 5.18 m/s [11].

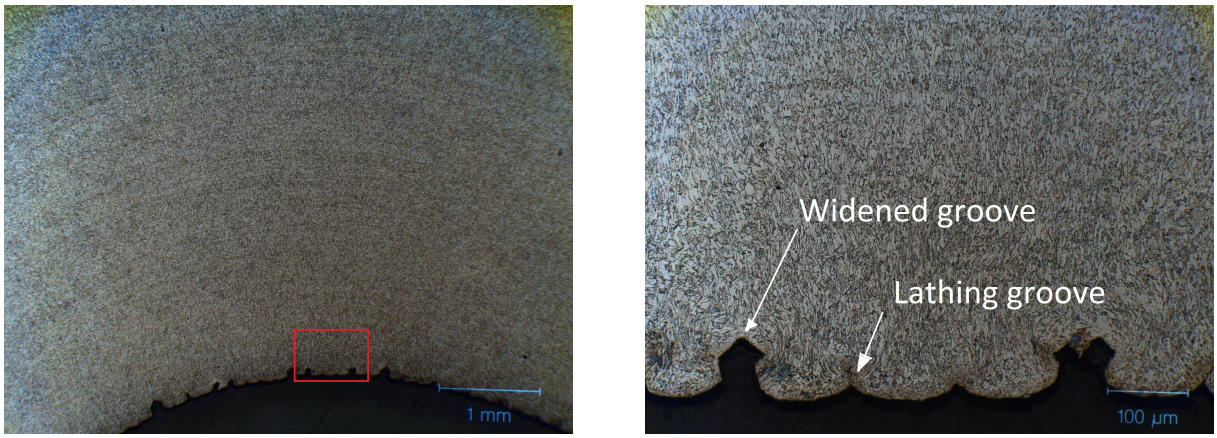

(a) Photo of bend for pipe 1. *(b) Photo of bend for pipe 1.*

Figure 3.16: Investigation of specimen from bend for pipe 1 [6].

3.4 Numerical Simulations

This section will give a brief summary of the numerical pipe simulations that have been performed in the four previous master theses written by by Slåttedalen and Ørmen [3], Fornes and Gabrielsen [4], Aune and Hovdelien [5] and Asheim and Mogstad [6]. The numerical simulations consist of parametric studies and simulations using different material models.

Shell basis models were established by Slåttedalen and Ørmen [3] for pipes A-D and a volume model was established for pipe B to check the validity of the global response from the shell element analyses. The graphical pre/post-processor Abaqus/CAE was used to establish these models. An overview of the shell model can be seen in Figure 3.17 with the impact step presented in Figure 3.17a and the stretching step in Figure 3.17b.

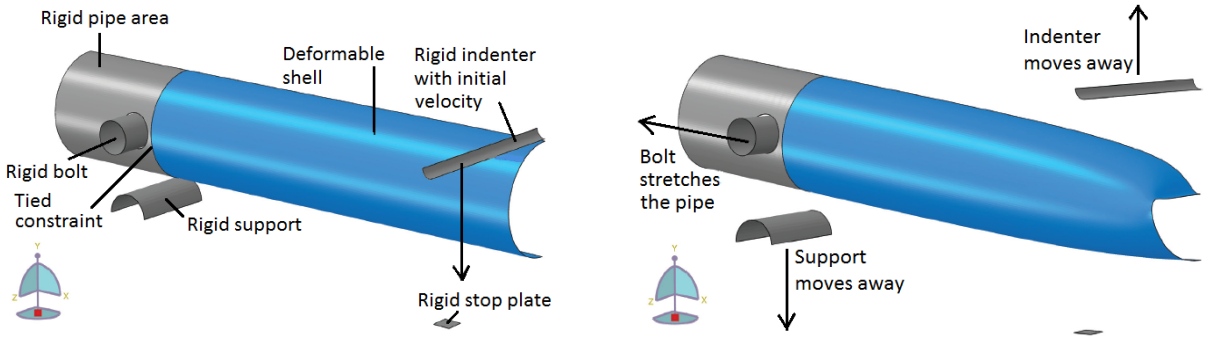

(a) Impact step. *(b) Stretch step.*

Figure 3.17: Shell model provided by Slåttedalen and Ørmen [3].

Force-displacement curves for the base shell model of pipe A, displaying the impact

and stretch step can be seen in Figure 3.18a and Figure 3.18b, respectively. The numerical results are plotted together with the experimental results. For the impact step it can be seen that the numerical simulation is overestimating the forces and the final deformation is slightly too small. It was also performed a volume element analysis to validate the numerical results of the global response from the shell element models. The global response is fairly similar, however the energy absorption is a little lower for the volume element model [3].

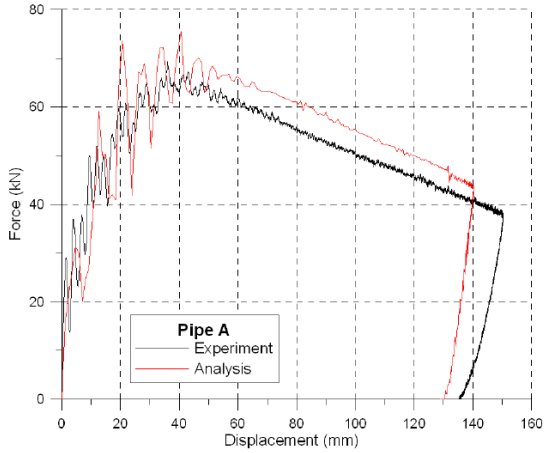

(a) Numerical simulation and experimental results of impact step for pipe A.

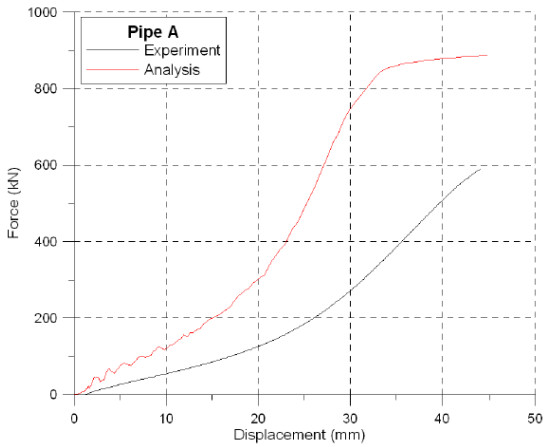

(b) Numerical simulation and experimental results of stretch step for pipe A.

Figure 3.18: Comparison between the global response from simulations with base shell model for pipe A and the response from the experiments [3].

It was decided to use shell element for most of the parametric studies since the computational cost is smaller and the global response were fairly similar when comparing shell element models with volume element models.

Shell model A mesh sensitivity analysis were carried out with 2 mm, 5 mm and 10 mm elements on the model representing pipe B. Force-displacement curves can be seen in Figure 3.19a while the absorbed energy is plotted against the mesh refinement in Figure 3.19b. It can be concluded that the global response is not very sensitive to the mesh size below a certain element size on the basis of this results. In Figure 3.20 equivalent plastic strains after the impact is shown for various mesh sizes. From this, it can be seen that the local plastic strains are clearly sensitive to the size of the mesh, since a refinement of the mesh gives an considerable increase of the plastic strain. Violating the condition that a shell element is defined with a small thickness to surface area relation may give a inaccurate response. It is pointed out by Slåttedalen and Ørmen [3] that the smallest elements had already short lengths compared to the thickness, so the mesh was not further refined and convergence could therefore not be found.

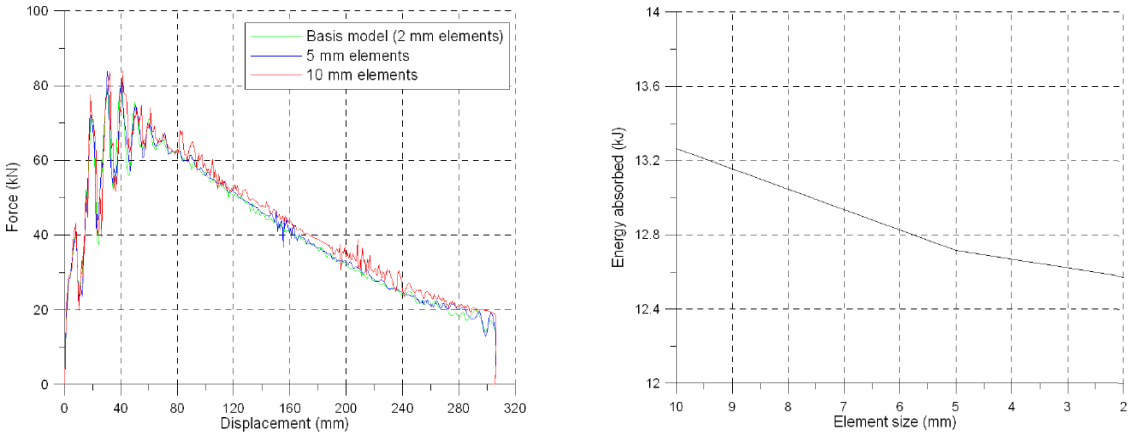

(a) Force-displacement curves. *(b) Energy absorption.*

Figure 3.19: Mesh sensitivity study for the shell element model of pipe B [3].

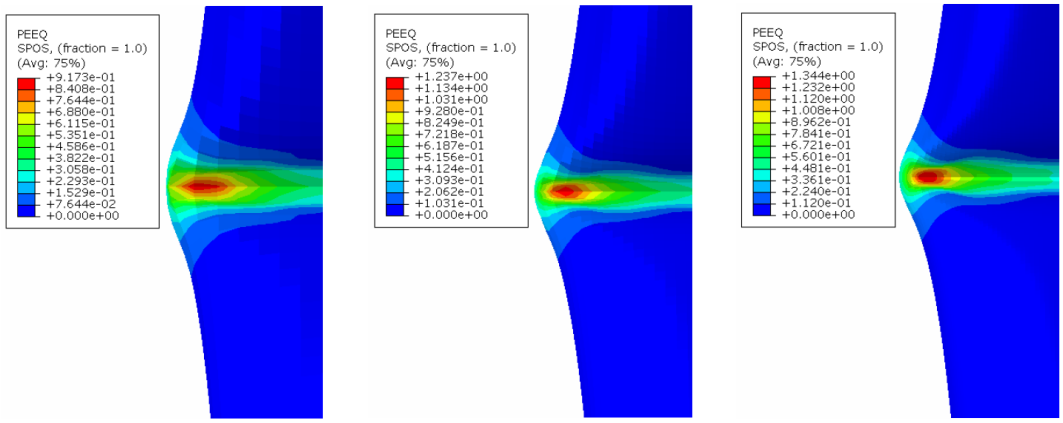

(a) 10 mm elements *(b) 5 mm elements* *(c) 2 mm elements*

Figure 3.20: Equivalent plastic strain from simulation of pipe B [3].

Further it was performed a thickness sensitivity analyses on pipe A. The force-displacement curve can be seen in Figure 3.21a, and the energy absorption in Figure 3.22b. The maximum and minimum values of the thickness in the analyses were taken as the extreme values from the measurements of the pipe. The global response in the impact step and stretch step is highly sensitive to the thickness as indicated by the force-displacement curves since a thicker pipe gives a significant stiffer system. To find appropriate thicknesses for the analyses, trial and error were used for the shell element model. These adjusted thicknesses were close to the average measured thicknesses of the pipes, indicating that they are correct. The analyses with the adjusted thicknesses gave a very good fit for the impact step with a little deviation in the final deformation while the results for the stretch step did not improve much.

Fornes and Gabrielsen [4] carried out simulations using Abaqus/Explicit on open and closed pipes filled with water by using shell models. The numerical results compared to the experimental results for the open pipes G and H, can be seen in Figure 3.22. As seen, the curves shows mostly a good agreement, except for an impulse force in the

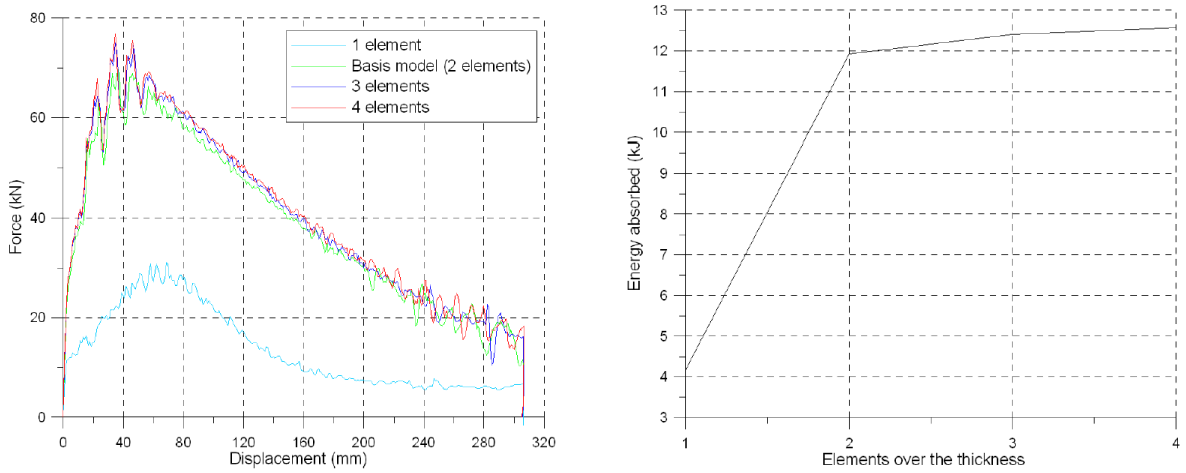

(a) Force-displacement curves. *(b) Energy absorption.*

Figure 3.21: Thickness sensitivity study for the solid element model on pipe A [3].

beginning of the analyses. This is believed to have something to do with the contact between the pipe and the support.

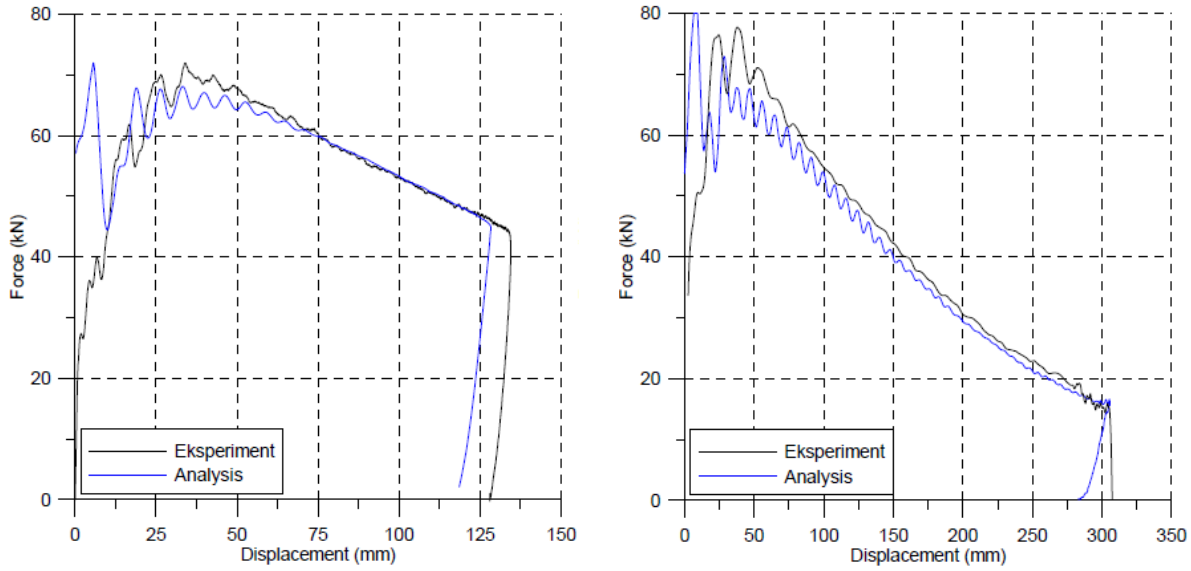

(a) Pipe G, v =3.21 m/s. *(b) Pipe H, v = 5.11 m/s.*

Figure 3.22: Force-displacement curves of experiments and analyses of water filled pipes with open ends [4].

The numerical result compared to the experimental result for the closed pipe I, can be seen in Figure 3.23. No numerical result are available for pipe J since the membrane closing the pipe had a fracture during the experimental test. It can be observed that the analysis is too stiff, which gives a higher load and shorter displacement, when compared to the experiment. It can however be noted that the distinct plateau in the force-displacement curve has been recreated. The reason for the too stiff behaviour is believed to be due to computational error and/or incorrect assumptions when making the model.

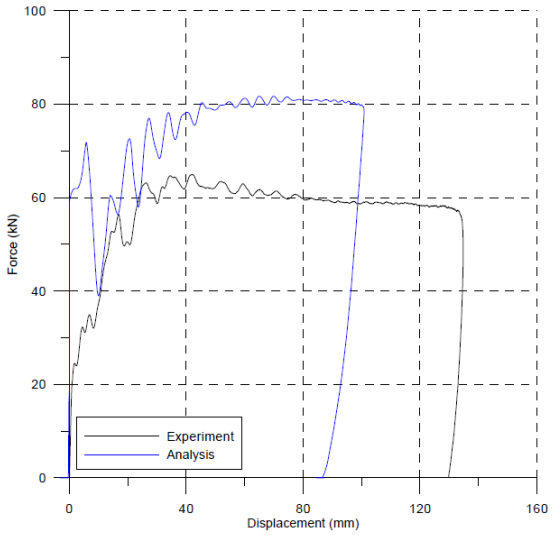

Figure 3.23: Force-displacement curves of the experiment and analysis for pipe I, v = 3.22 m/s [4].

Aune and Hovdelien [5] calibrated a material model by inverse modeling. Then, an analysis on pipe A was performed in Abaqus/Explicit. The global results from the analysis can be seen in Figure 3.24, where it has been plotted with the numerical results of pipe A carried out with the different material models obtained by Slåttedalen and Ørmen [3] and Fornes and Gabrielsen [4]. The experimental result on pipe A has also been plotted as a comparison. The impact step is recreated well in the numerical simulations, however the numerical results for the stretch step shows an overly stiff behaviour.

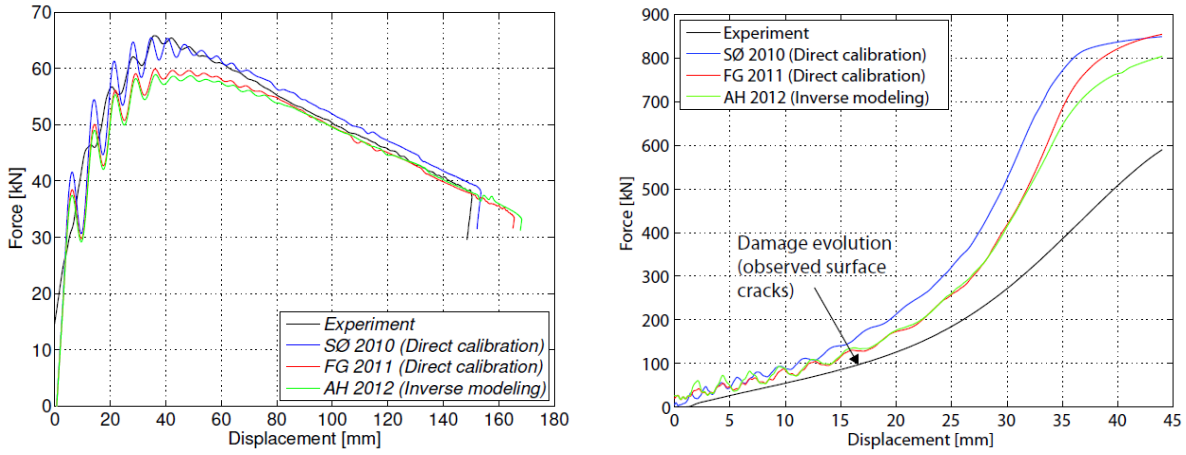

(a) Impact. *(b) Stretching.*

Figure 3.24: Global response with various material models. Numerical simulations in ABAQUS/Explicit of pipe A (v = 3.24 m/s) [5].

Asheim and Mogstad [6] used Abaqus/Explicit to carry out numerical simulations, which featured a bending step and a stretch step with shell and solid models. Figure 3.25a and Figure 3.25b depicts the bending of pipe 1 and 2, respectively. For pipe 1 both

models corresponds well with the experiments, while the numerical results deviates from the experimental data for pipe 2, by being stiffer up to peak force. After peak force the numerical curves show a better fit with the experimental data and the shell model seems to be marginally stiffer than the solid model and experimental data for both pipe 1 and 2. This was expected as the solid model has a refined mesh, softening the behavioiur of the numerical model.

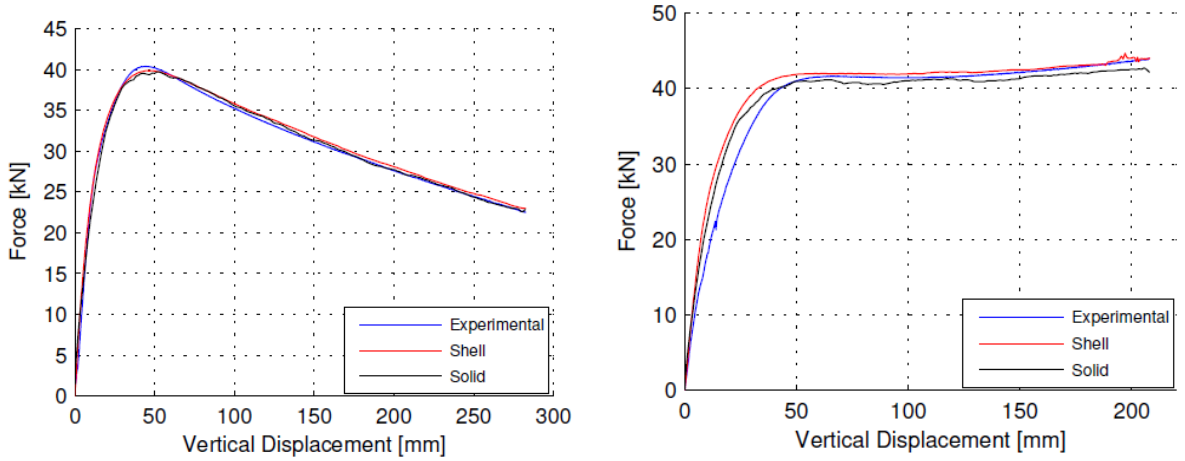

(a) Bending step pipe 1. *(b) Bending step pipe 2.*

Figure 3.25: Force-displacement for the indenter using shell and solid models [6].

In Figure 3.26a the stretch step for pipe 1 can be seen carried out with shell and solid models and the experimental result. The results from the shell and solid models are identical, but they are much stiffer than the experimental result. The stretching of pipe 2 can be seen in Figure 3.26b. No result obtained for the stretching of pipe 2 with a solid model, due to a high computational demand. However, the shell model shows the same, much stiffer behaviour, as for pipe 1.

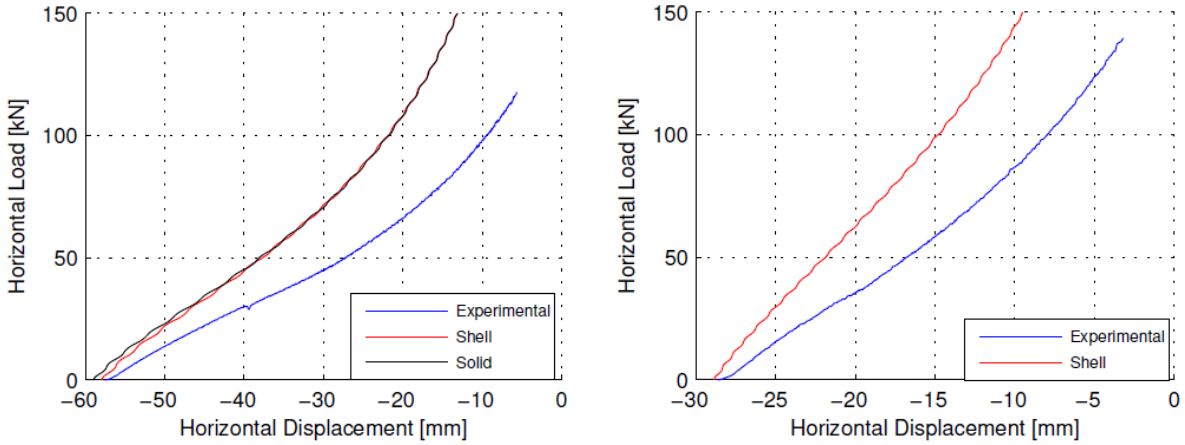

(a) Stretch step pipe 1. *(b) Stretch step pipe 2.*

Figure 3.26: Force-displacement for the indenter using shell and solid models [6].

Chapter 4

Material

This chapter first presents the SIMLab Material Model (SMM) and some of its theory, before the material parameters of the X65 steel used in the numerical simulations are established and presented. The material parameters are passed by a material card into the finite element numerical simulations.

In this thesis it has been used an isotropic material model for all the numerical simulations, as this has shown to capture the global response of the bending step in the previous theses in a good way. A damage criterion has also been presented.

4.1 SIMLab Metal Model

SIMLab Metal Model makes it possible to define a number of constants for material models used in finite element simulations. MatPrePost works in combination with SMM and is used to process experimental data into material parameters. In the following sections the SMM theory regarding isotropic hardening, damage and fracture and transverse shear stiffness is presented. For more details about SMM and MatprePost it is reffered to Asheim and Mogstad [6] and the theory manual for SMM [16].

4.1.1 Isotropic Hardening

From the theory manual of SIMLab Metal Model [16] it is stated that the isotropic hardening variable R is defined by

$$R = \sum_{i=1}^{N_R} R_i \tag{4.1}$$

where N_R is the number of isotropic hardening terms. R_i is expressed as

$$R_i = \theta_{Ri}(T) r_i \tag{4.2}$$

where the initial hardening moduli are $\theta_{Ri} = \theta_{Ri}(T)$. The evolution equations for r_i are defined as

$$dr_i = (1 - \frac{R_i}{Q_{Ri}(T, \dot{p})}) dp \tag{4.3}$$

where $Q_{Ri} = Q_{Ri}(T, \dot{p})$ is the saturation value of term R_i at given values of $\dot{p}$ and T. A special case is when the temperature T is constant and the plastic strain rate $\dot{p}$ is constant. Assuming $p = 0$ and $R_i = 0$ as initial values, combining Equation (4.3) with Equation (4.2) and integrating analytically we obtain

$$R_i = Q_{Ri}(1 - \exp(-\frac{\theta_{Ri}}{Q_{Ri}} p)) \tag{4.4}$$

which is a Voce hardening term as seen in Equation (2.4). Finally, the isotropic hardening contribution can be expressed as

$$R = \sum_{i=1}^{N_R} R_i = \sum_{i=1}^{N_R} Q_{Ri}(1 - \exp(-\frac{\theta_{Ri}}{Q_{Ri}} p)) \tag{4.5}$$

which is a summation of Voce hardening terms. The saturation value of R , R_{sat} is reached when $p \to \infty$

$$R_{sat} = \sum_{i=1}^{N_R} Q_{Ri} \tag{4.6}$$

4.1.2 Damage and Fracture

The damage in this thesis is uncoupled with the constitutive equation. This means damage evolves based on the stresses and the plastic strain rates but the damage has no influence on the constitutive response before fracture occurs [16].

From the theory manual of the SMM the uncoupled version of the Extended Cockroft-Latham (ECL) criterion is defined as

$$\dot{D} = \langle \frac{\phi \hat{\sigma}_I + (1 - \phi)(\hat{\sigma}_I - \hat{\sigma}_{III})}{S_0} \rangle^{s_0} \dot{p} \tag{4.7}$$

where $\langle a \rangle$ = $max(a, 0)$ for any scalar a, $S_0 > 0$, $s_0 > 0$ and $0 \leq \phi \leq 1$ are constants that are identified from available experimental data and $\hat{\sigma}_I \geq \hat{\sigma}_{II} \geq \hat{\sigma}_{III}$ are the ordered eigenvalues of the Cauchy stress tensor.

One special case of this criterion is obtained by setting s_o = 1 and $\phi = 1$ in Equation (4.7) which gives the Cockroft-Latham criterion as

$$\dot{D} = \frac{\langle \hat{\sigma}_I \rangle}{S_0} \dot{p} \tag{4.8}$$

D equals its critical value D_C at fracture, so

$$\int_0^{p_f} \langle \hat{\sigma}_I \rangle dp = D_C S_0 \tag{4.9}$$

where p_f is the equivalent plastic strain at fracture. The Cockroft-Latham parameter W_C is

$$W_C = D_C S_0 \tag{4.10}$$

Element erosion describes the fracture and crack propagation. As one or several of the fracture criteria applied are reached in an integration point, the stress tensor is set to zero, and this integration point can no longer carry load [16].

When the damage variable D reaches its critical value $D_C \geq 1$ the critical damage criterion implies that an integration point fails. It should be noted that if uncoupled damage is assumed, as in this thesis, the critical value of the damage parameter may be set to unity without loss of generality.

4.1.3 Transverse Shear Stiffness

When using shell elements the transversal shear stiffnesses are required as input in ABAQUS. When using SMM in combination with ABAQUS, the initial transverse shear stiffness has to be inserted manually into the input file for the numerical simulations. The transverse shear stiffnesses are calculated by

$$K_{11}^{ts} = K_{22}^{ts} = \frac{5}{6} G t \qquad\qquad K_{12}^{ts} = 0 \tag{4.11}$$

where G is the shear moduli of the material in the out-of-plane direction and t is the element thickness [17].

4.2 Material Constants

4.2.1 Material Model

As mentioned in Section 3.2 Slåttedalen and Ørmen [3] calibrated the Johnson-Cook constitutive relation. This is a phenomenological model used for modeling the mechanical response of the pipe when carrying out numerical simulations. The Johnson-Cook model [12] is given by the formula

$$\sigma_{eq} = (A + B\varepsilon_{eq}^{n})(1 + C\ln\dot{\varepsilon}_{eq}^{*})(1 - T^{*m}) \tag{4.12}$$

where σ_{eq} is the equivalent stress, ε_{eq} is the equivalent plastic strain, $\dot{\varepsilon_{eq}}$ is the dimensionless equivalent plastic strain rate and T is the temperature. Further the dimensionless strain rate is given as

$$\dot{\varepsilon_{eq}^{*}} = \frac{\dot{\varepsilon}_{eq}}{\dot{\varepsilon}_{0}} \tag{4.13}$$

where ε_0 is the reference strain rate and the homologous temperature is given as

$$T^{*} = \frac{T - T_r}{T_m - T_r} \tag{4.14}$$

where T_m is the melting temperature and T_r is the room temperature. A, B, C, n and m are material constants that have to be found by conducting material testing [17].

4.2.2 Isotropic Hardening

In this thesis the simulations will be carried out with isotropic hardening. When using SMM a material card has to be established as input to the numerical simulations. The input of the isotropic hardening parameters have to be on Voce form according to the SMM Voce rule in Equation (4.5).

When Slåttedalen and Ørmen [3] calibrated the Johnson-Cook relation they only looked into the effects of strain-hardening and strain-rate effects, as isothermal conditions are assumed. Then Equation (4.12) reduces to

$$\sigma_{eq} = (A + B\varepsilon_{eq}^{n})(1 + C\ln\dot{\varepsilon}_{eq}^{*}) \tag{4.15}$$

The material parameters from the calibration of Johnson-Cook can be seen in Table 3.1 and are presented here in Table 4.1 for simplicity.

Table 4.1: Isotropic hardening material model.

Material parameters	**A**	**B**	**n**	**C**	$\dot{\varepsilon}_0$
Direct calibration [3]	465.5	410.83	0.4793	0.0104	0.000806

Since the material card for SMM requires the isotropic hardening on Voce form, the Johnson-Cook relation has to be transformed to this form. From Section 4.1.1 the Voce form of the SMM is given as

$$R = \sum_{i=1}^{N_R} R_i = \sum_{i=1}^{N_R} Q_{Ri}(1 - exp(-\frac{\theta_{Ri}}{Q_{Ri}}p)) \tag{4.16}$$

and from Section 2.1 the defined Voce form can be seen as

$$R(p) = Q_i(1 - exp^{-b_i p}) \tag{4.17}$$

The relations between the parameters in Equation (4.16) and Equation (4.17) are given as

$$Q_{Ri} = Q_i \qquad\qquad \theta_{Ri} = bQ_{Ri} \tag{4.18}$$

4.2.3 Fracture Criteria

A very simple fracture criterion is the Cockroft-Latham ductile fracture criteria, which is based on plastic work per unit volume [5]. The ductility of a material depends on the stress state (stress triaxiality), strain rate and temperature [3]. The criterion is given by

$$\int_0^{\varepsilon_f} \langle \sigma_1 \rangle d\varepsilon_{eq} = W_{cr} \tag{4.19}$$

where σ_1 is the maximum principal stress, W_{cr} is the Cockroft-Latham parameter and $\langle \sigma_1 \rangle$ means that $\langle \sigma_1 \rangle = \sigma_1$ when $\sigma_1 > 0$ and $\langle \sigma_1 \rangle = 0$ when $\sigma_1 < 0$.

The Cockroft-Latham parameter W_{cr} was found by Slåttedalen and Ørmen [3] to be 1595 MPa by an approximation using the area under the true average stress-strain curve seen in Figure 3.2. The Cockroft-Latham criterion can be used in Abaqus directly when using SMM, see Section 4.1.2.

4.2.4 Properties of Steel Grade X65

As mentioned in Section 3.1.1, the almost identical true stress-true strain curves from different locations, in Figure 3.3a, indicates that the material is homogenous over the cross-section. Further the material can be assumed isotropic as the true stress-true strain curves from different directions, which can be seen in Figure 3.3b, has only insignificant deviations.

The X65 steel consists of, given in weight percent, 0.10 % carbon, 1.5 % Manganese, 0.35 % silicon, 0.005 % sulfur, 0.15 % phosphorus, nitrogen 0.015 % in addition to iron [18]. Vanadium and titanium can be added for extra toughness. X65 has very good weldability and it is a quite though steel, which is its best physical properties. The reason why X65 is an attractive steel, primarily used in the oil and gas industry, is its combination of high strength and low cost. This makes it very convenient to use it e.g. as pipelines, as these usually extends over several miles.

The Young's modulus E = 208000 MPa [3].

4.3 Material Card

The isotropic hardening variables were obtained by calibrating a Voce rule, seen in Equation (4.16), by using the method of least squares and the Johnson-Cook relation, seen in Equation (4.15), as a basis. Since the experimental tests were to be carried out quasi-statically, the strain-rate sensitivity was disregarded. The Voce hardening parameters compared with the Johnson-Cook parameters can be seen in Figure 4.1. There is a very good fit between the curves.

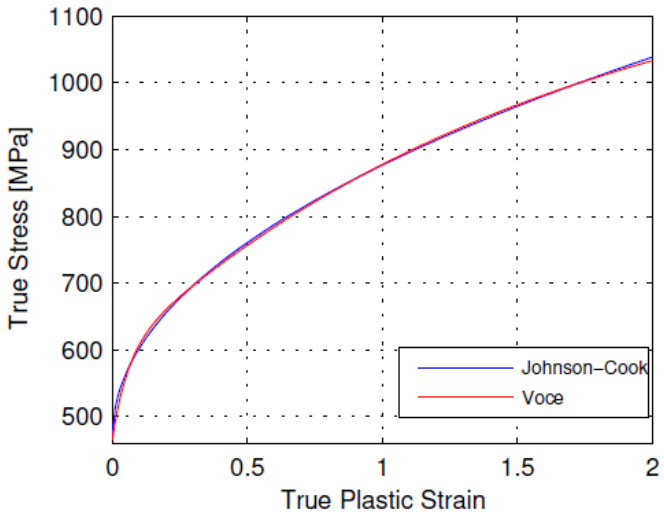

Figure 4.1: Voce hardening function fitted to rate independent Johnson-Cook [6].

The transverse shear stiffness was calculated by the use of Equation (4.11) in Section 4.1.3.

A Cockroft-Latham damage criterion was implemented and the fracture parameter S_0 = W_{cr} is presented in Section 4.2.3.

A summary of the material parameters that have been used for the numerical simulations can be seen in Table 4.2. The material card in its original appearance is presented in Appendix B.

Table 4.2: Material parameters used as input for numerical simulations.

Isotropic Hardening $[MPa]$	σ_0 465.5	Q_{R1} 627.1	θ_{R1} 379.5	Q_{R2} 127.1	θ_{R2} 2207
Transverse Shear Stiffness $[N/mm]$	K_{11}^{ts} $2.67 \cdot 10^5$	K_{22}^{ts} $2.67 \cdot 10^5$	K_{12}^{ts} 0		
Damage	S_0 1595 $[MPa]$	D_c 1	s_0 1	ϕ 1	β 0
Properties	E $208000[MPa]$	ν 0.3	ρ $7.85 \cdot 10^{-9}[tons/mm^3]$		

Chapter 5

Preliminary Studies

5.1 Experimental setup

In this section a short introduction to the stretch bending rig is given. This rig will be used to bend the pipes, while simultaneously applying different horizontal loads. Further it will be given a review of bending of the pipes in the stretch bending rig.

5.1.1 Stretch Bending Rig

To perform the bending of the pipes, a stretch bending rig will be used. The rig is situated in the test laboratory of SIMLab at Department of Structural Engineering, NTNU. A report on the strech bending rig has been written by A.H. Clausen [19]. This report gives an in-depth explanation of the strectch bending rig and its instrumentation. This section is mainly a brief recap of this report.

An overview of the stretch bending rig can be seen in Figure 5.1. It should be noted, that for the experiments conducted in this thesis an indenter will replace the bending die. The laser seen in the overview will not be used. The rig is built up by a steel frame consisting of two columns made of cross-section HE 450-B and one horizontal beam of cross-section HE 240-B. It is important to avoid deflections in the steel frame, as these will influence the displacement measurements of a test specimen, which explains the use of relatively large columns.

The main components of the rig are three HYDRONIC actuators that are servo controlled with a maximum load capacity of $\pm$ 330 kN. The two horizontal servohydraulic actuators are of the type CAV 180/90-300, with a total stroke length of 300 mm. The vertical actuator are of the type CAV 160/100-500, with a total stroke length of 500 mm. The horizontal actuators have the purpose to introduce the desired axial force in

the test specimen. The vertical actuator is controlling the vertical displacement of the indenter.

The grip for the specimens are joined to the end of the horizontal actuator's cylinder by a hinged joint. With this hinge the specimen are free to rotate independently of the actuator's position. The specimens ends are simply supported i.e. no bending moment.

Both load and displacement control may be used for tests in the rig. Load control can be used to e.g. stretch the specimen to a specific tensile force and keep it constant while the indenter move to a prescribed position in displacement control.

The vertical actuator and one of the horizontal actuators are provided with load cells. The other horizontal actuator acts as a displacement controlled slave with regard to the completely instrumented horizontal actuator. Symmetric geometry and equal displacements in the horizontal actuators ensure that the forces in the two actuators are equal.

The vertical load cell can only measure compressive forces while the horizontal load cells can measure both tensile and compressive forces. Displacements are measured independently in all three actuators by means of resistive displacements transducers supplied with the actuators. The resolution of the displacement measurements are 0.1 mm. Measurements of the rotational angles at both of the hinged joints are also performed with one clinometer at each support. The clinometers have a range from -60° to +60°.

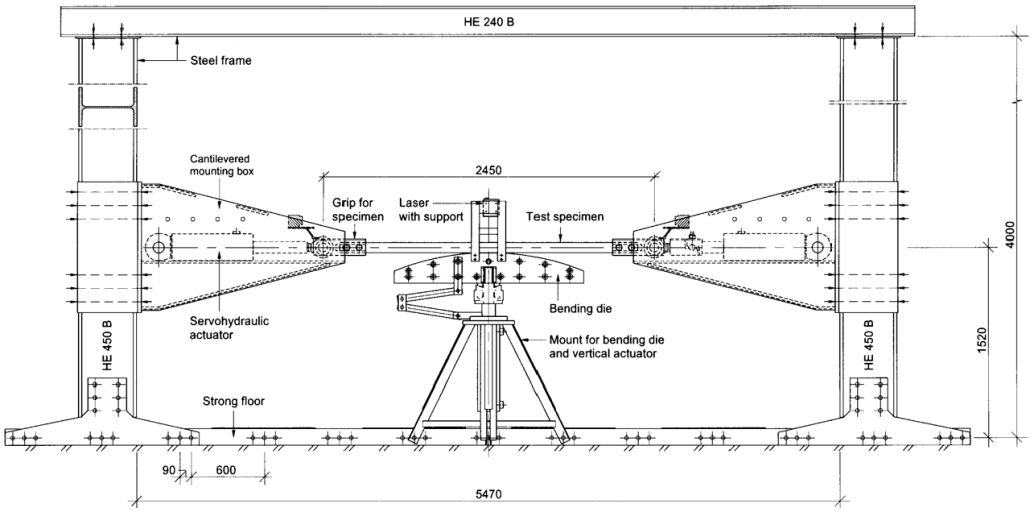

Figure 5.1: Overview of the stretch bending rig [19].

5.1.2 Bending of Pipes in the Stretch Bending Rig

The bending of the pipes will be carried out in the stretch bending rig described in Section 5.1.1. A machine drawing of the pipes that are going to be bent can be seen in Figure 5.2. The initial pipe has a thickness of $9.5\ mm$. A midpart of length $925\ mm$ was then lathed down to a thickness of $4\ mm$, while the ends of the pipe keeps the original thickness. The reason for lathing is to reduce the bending strength of the pipe so the stretch bending rig can be used and to achieve a D/t-ratio of approximately 30 [20] as is common in many pipes. The total length of the pipe is $1250\ mm$ and the inner diameter is $123\ mm$.

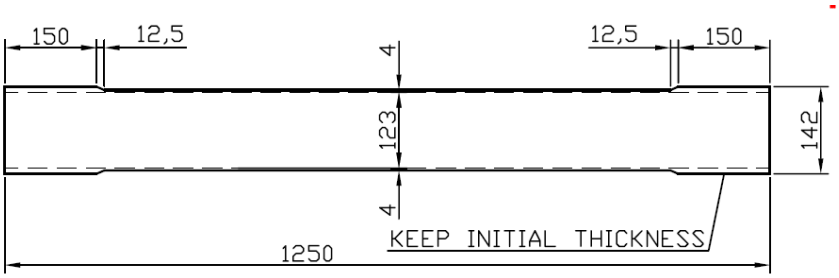

Figure 5.2: Machine drawing of the pipe.

To connect the pipes to the horizontal actuators there has been made some special parts for this experimental testing. The reason for making these new parts is so the pipes can be fastened to the grips at the horizontal actuators. The new parts can be seen in Figure 5.3. The parts are a flange, a fork and a block bearing. To mount the pipe to the actuator the pipes will be welded to the flange. The flange will then be bolted to the fork with 12 bolts. A shaft is used to fasten the block bearing to the fork. A grip that is mounted to the horizontal actuator is fastened to the block bearing. The final assembly of the connection between the pipe an the horizontal actuator can be seen in Figure 5.4.

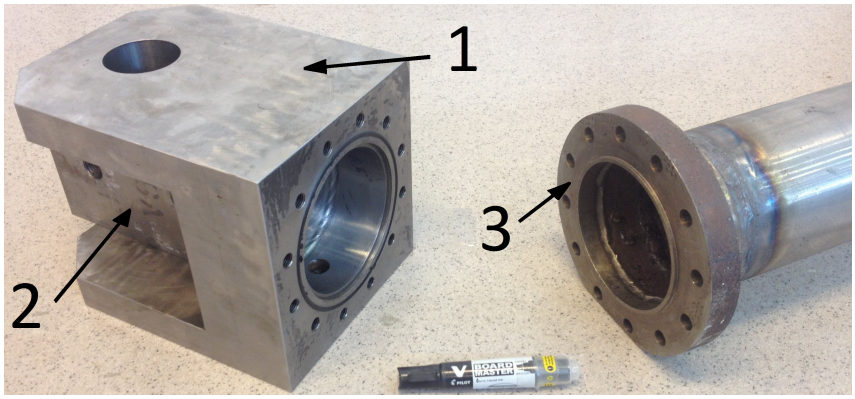

Figure 5.3: Parts of the connection between the pipe and the horizontal actuator. Fork (1), block bearing (2) and flange (3) [6].

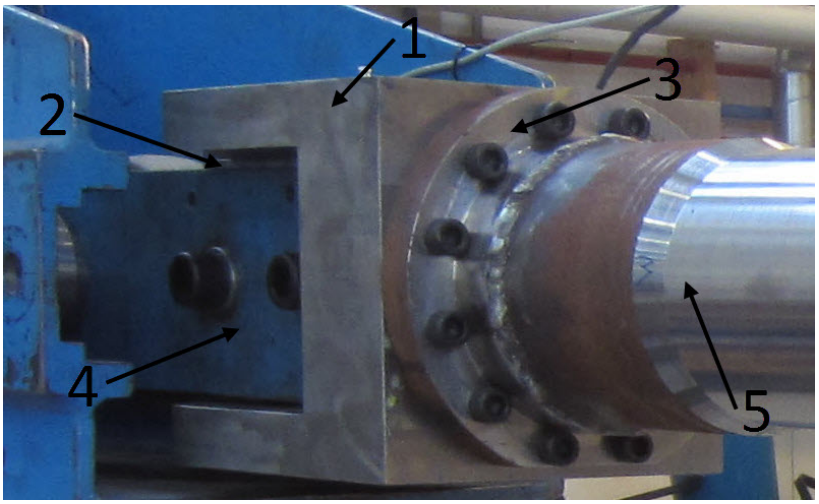

Figure 5.4: Final assembly of the pipe-rig connection. Flange (1), block bearing - not visible (2), flange (3), grip (4) and the pipe (5).

In Figure 5.5 a machine drawing of the pipe-rig connection, showing a vertical cut, can be seen. RP is the rotational point which is the hinged joints that the pipes will rotate about. From the drawing it can be seen that the distance from the RP to the end of the weld between the flange pipe is 478 mm. With 30 mm of the pipe inserted into the flanges before welding, the total length between each RP is 2146 mm.

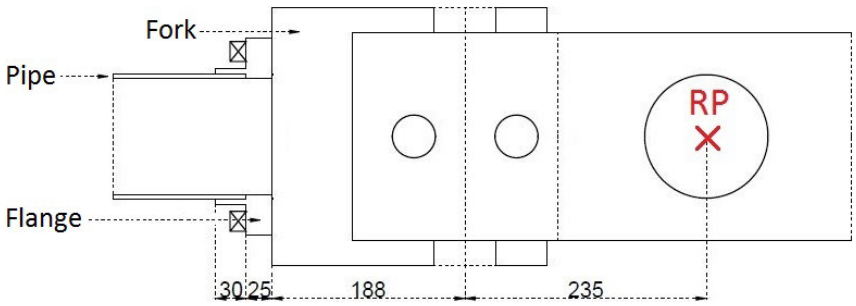

Figure 5.5: Machine drawing of the pipe-rig connection, measurements in mm [6].

The die that was used by A. H. Clausen in [19] is replaced with an indenter that has been used in the four previous master theses [3, 4, 5, 6]. The indenter seen in Figure 5.6, has a wedge shape with a tip radius of 10 mm, which is recommended by DNV [15]. This recommendation is done for dynamic testing but it was decided to use it also in the quasi-static tests. This was also done by Asheim and Mogstad [6].

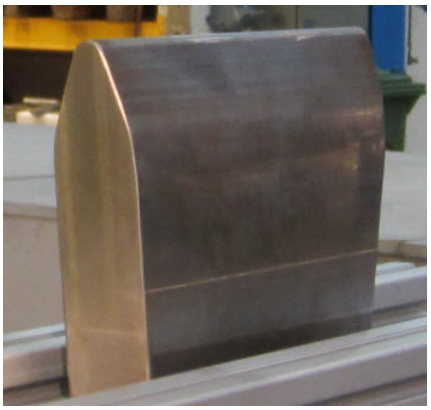

Figure 5.6: Indenter.

5.2 Initial Strength Calculations

In this section there has been conducted initial strength calculations of the pipes. The elastic axial capacity and plastic bending capacity and the stresses in a pipe with inner pressure have been calculated. The measurements of the pipe used for the calculations can be seen in Section 6.1.

5.2.1 Elastic Axial Capacity

Figure 5.7 shows the cross section of the pipe specimen with thickness t and the average diameter R_{m}.

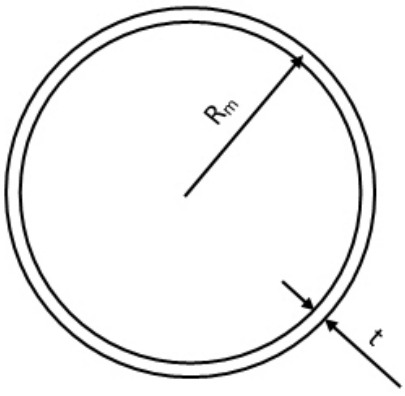

Figure 5.7: Cross-section of pipe with average radius R_m and thickness t.

The axial stress in the pipe is given by Equation (5.1) where A_p is the cross-sectional area and N_p is the elastic axial capacity.

$$\sigma_{N,y} = \frac{N_p}{A_p} \tag{5.1}$$

The area of the pipe is $A_\mathrm{p} = 2\pi R_\mathrm{m} t$ so the elastic axial capacity is given as

$$F = 2\pi R_m t \sigma_{N,y} \tag{5.2}$$

With R_m = 63.22 mm, t = 4.15 mm and $\sigma_{N,y}$ = 472 MPa determined by Slåttedalen and Ørmen [3], the elastic axial capacity is F = 778.1 kN. The maximum loads of the horizontal actuators are 330 kN. With a length from the rotational joint to the mid of the pipe of 1073 mm and a maximum vertical deformation of 500 mm, will give an angle of 27.8°. This gives a maximum axial load in the pipe of 373 kN which is far below the elastic axial capacity of the pipe.

5.2.2 Plastic Bending Capacity

The pipes are simply supported in the experimental testing in the stretch bending rig. The vertical actuator is acting like a point load at the midpoint, when deforming the pipes vertically as seen in Figure 5.8.

Figure 5.8: Simply supported pipe with a point load P at the midpoint.

The point load P will induce a bending moment at the midpoint given as

$$M = \frac{PL}{4} \tag{5.3}$$

The plastic moment capacity is given by

$$M_\mathrm{p} = W_\mathrm{p} \sigma_\mathrm{y} \tag{5.4}$$

where σ_y is the yield strength and W_p is the plastic section modulus. Equation (5.3) combined with Equation (5.4) gives the plastic bending capacity expressed as

$$P_\mathrm{p} = \frac{4 W_\mathrm{p} \sigma_\mathrm{y}}{L} \tag{5.5}$$

The plastic section modulus of a pipe is [21]

$$W_{\mathrm{p}} = \frac{4}{3}(r_o^3 - r_i^3) \tag{5.6}$$

where r_o and r_i is the outer and inner radius, respectively. The final expression for plastic bending capacity of the pipe is found by combining Equation (5.5) with Equation (5.6), which gives

$$P_p = \frac{16(r_o^3 - r_i^3)\sigma_y}{3L} \tag{5.7}$$

With $r_o = 65.3\ mm$, $r_i = 61.15\ mm$, $\sigma_y = 472\ MPa$ and $L = 2146\ mm$, the plastic bending capacity of the pipes are $P_P = 58.4\ kN$. This is well below the capacity of the vertical actuator with a capacity of $330\ kN$.

5.2.3 Stresses in Pipes with Inner Pressure

Figure 5.9 gives an overview of a pipe with radius r, thickness t and inner pressure p. When assuming the pipe to be thin-walled there will be two stresses in the pipe, namely the longitudinal stress σ_{l} and the circumferential hoop stress σ_{h}.

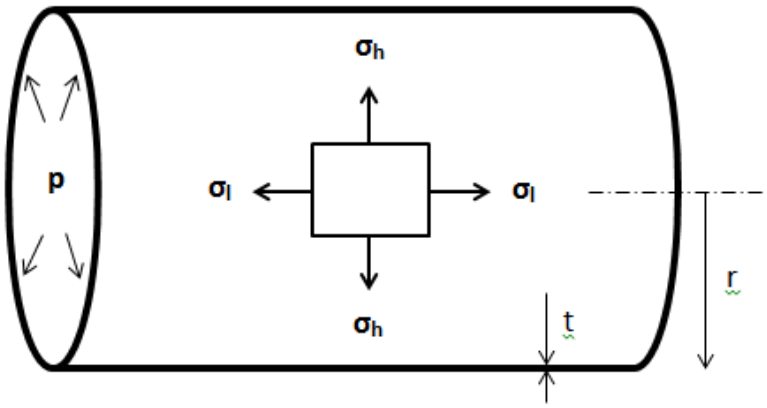

Figure 5.9: Pipe with inner pressure p.

The longitudinal stress is given by the equation

$$\sigma_{\mathrm{l}} = \frac{r}{2 * t} * p \tag{5.8}$$

With $r = 61.15\ mm$, $t = 4.15\ mm$ and $p = 100\ bar = 10\ MPa$ the longitudinal stress is σ_{l} = 73.7 MPa. This gives an axial force of 121.5 kN.

The hoop stress is given by the equation

$$\sigma_{\text{h}} = \frac{r}{t} * p \tag{5.9}$$

With $r = 61.15\ mm$, $t = 4.15\ mm$ and $p = 100\ bar = 10\ MPa$, gives this a hoop stress of σ_{h} =147.3 MPa.

5.3 Modeling of Basis Models

To perform the numerical simulations there has been established two basis numerical models. One basis model for the non-pressurized pipes and one basis model for the pipes with inner pressure. Shell models have been used for the preliminary studies. The experimental setup described in Section 5.1 in combination with the basis models used by Asheim and Mogstad [6] has been used as a basis for the establishment of the shell basis models.

5.3.1 Geometry

The model consists of three parts. A deformable part representing the pipe and two discrete rigid parts representing the indenter and the pipe-rig connection respectively. An overview of the basis model can be seen in Figure 5.10. Only one quarter of the model has been modeled as symmetry has been utilized to decrease the computational time of the numerical simulations.

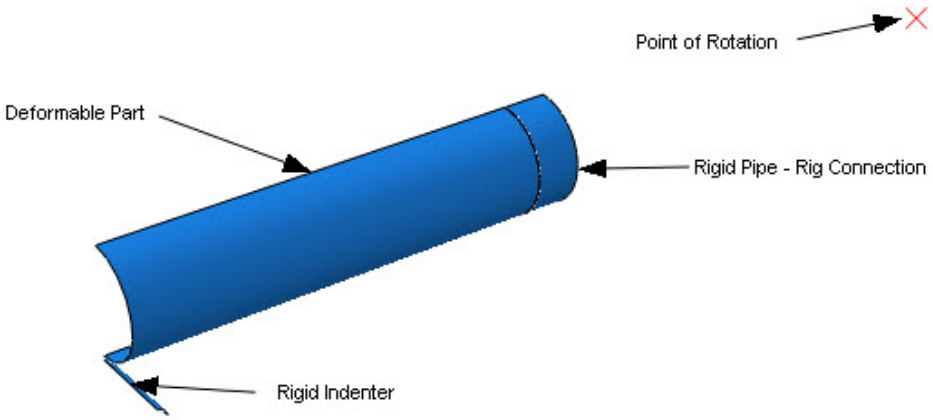

Figure 5.10: The different parts of the shell basis models.

The deformable part of the pipe is taken to be the lathed area, as the rest of the pipe and the pipe-rig connection have been assumed to be rigid. The length of the deformable

part is found by taking the total length of the pipe which is 1250 mm, minus the length of the unlathed area of 150 mm, as seen in Figure 5.2, giving a length of 475 mm. A shell thickness of 4.15 mm and an inner diameter of 122.3 mm was chosen. These values are the average of the measured values of the pipes that are going to be used in the experiments, described in Section 6.1.

To model the parts between the horizontal actuator and up to the unlathed area, there has been chosen to use a discrete rigid part with an arbitrary length of 50 mm [6]. This part was given an offset reference point (RP), seen in Figure 5.11, to represent the rotational joint. This was done so the loads from the horizontal actuator could be applied to the pipe according to the experimental setup.

The discrete rigid part of the basis model for pressurized pipes also have a cap modeled in the end, as this is in accordance with the experimental setup. The diameter of this part was set to be 122.3 mm.

The indenter was modeled as discrete rigid with a radius of 10 mm and given a reference point, to where the vertical deformation of the indenter will be applied.

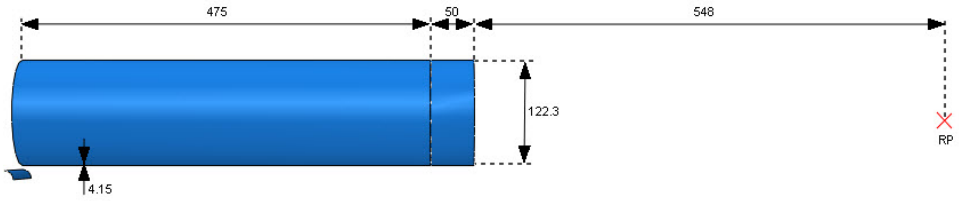

Figure 5.11: The dimensions for the basis shell models in mm.

5.3.2 Isotropic Hardening Material Model

For the numerical simulations, an isotropic hardening material model has been used. The material model and its parameters was implemented into Abaqus by the use of SIMLab Metal Model that was presented in Section 4.1. An overview of the material parameters can be seen in Table 4.2 and the material card can be seen in Appendix B.

5.3.3 Assembly and Contact

The pipe-rig connection part was tied to the deformable part as seen in Figure 5.11. The indenter was placed just below the midpoint of the deformable part.

There has to be applied an interaction between the pipe and the indenter to deform the pipe with the indenter. A surface to surface interaction was chosen with penalty method as the mechanical constraint formulation. In combination with rigid bodies the

penalty method is more flexible than the other methods [17]. Tangential behaviour was chosen as the contact property. No friction was assumed between the indenter and the pipe, so the friction coefficient was set to zero.

5.3.4 Boundary Conditions

In Figure 5.12 the applied boundary conditions can be seen. To ensure that symmetry is retained, x-symmetry of the pipe edge and z-symmetry of the mid-end of the pipe have been applied. The indenter was restricted to only translate in y-direction. The reference point (RP) of the rigid end part was restricted to translation in z-direction and rotation about x-direction, so the shell basis model will be simply supported such as in the experimental setup. The different loads in the simulations will be applied to the reference point acting in the horizontal direction and will therefore not rotate with the pipe.

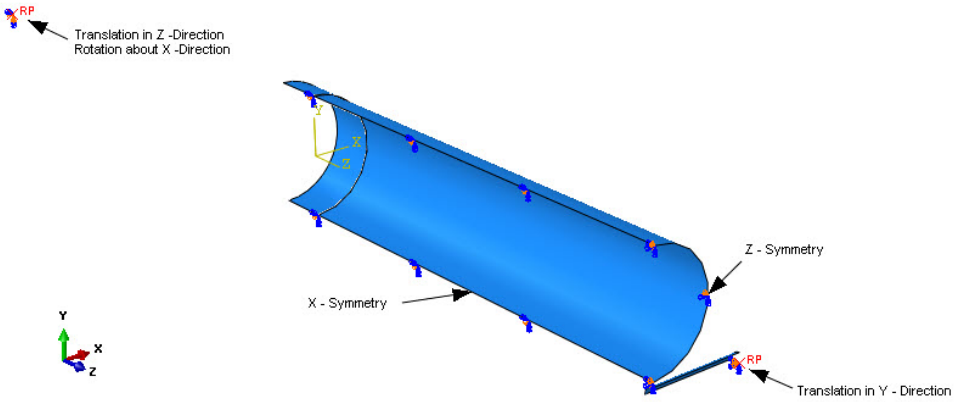

Figure 5.12: The boundary conditions applied to the basis shell model.

5.3.5 Mesh

The deformable part was meshed with quadratic 4 mm S4R shell elements which is the same as Asheim and Mogstad [6] used. This discretization gave 5712 elements. The S4R element is a 4-node general-purpose shell, reduced integration with hourglass control and finite membrane strains [17].

5.3.6 Steps

The different simulations that have been carried out have different loading and pressure conditions. The number of steps are therefore varying for the different simulations. The possible steps applied are

1. Pressure will be applied and kept constant during step 2 and 3.
2. Possible constant horizontal loads are applied and will be kept constant during the next step.
3. The indenter deforms the pipe 200 mm vertically. A possible linearly increasing load is applied during this step.

The last step, the bending step, is the step of interest in the numerical simulations. Step 1 and 2 are only preparation before step 3. The numerical simulations are based on quasi-static experiment that takes several minutes. To increase the computational efficiency of the numerical simulations they will be time-scaled. When using time-scaling it is important to check the kinetic energy of the system compared with the internal energy to assure inertia forces are insignificant. The kinetic energy of the deforming material should not exceed a small fraction of its internal energy throughout the majority of a quasi-static analysis [22]. In the beginning of an analysis this is usually not possible since the deformable body will have some motion before it deforms significantly.

In step 3, the bending step, a step time of 1 s was applied. This gives the indenter a velocity of 200 mm/s. A smooth amplitude has been applied for the loading of the linearly increasing load and to the deformation of the pipe with the indenter. This amplitude has derivatives that are zero at the start and end of the step. The reason for using this amplitude is because it decreases numerical noise in the results from the simulations.

5.4 Numerical Simulations

Abaqus/Explicit which is a finite element analysis product has been used to perform the numerical simulations. The preliminary numerical simulations have been carried out with the two basis models established for non-pressurized pipes and pressurized pipes in Section 5.3. The numerical simulations have been carried out with different boundary conditions, applied load levels, and with and without internal pressure. This has been done to get a sense of how the experiments in the stretch bending rig will behave. An overview of the performed simulations can be seen in Table 5.1 where the simulations are labeled 1 to 9. C is constant applied horizontal load and LI is linear increasing applied horizontal load. 50 and 100 is the load level given in kN. The applied vertical deformation of the indenter is 200 mm in all simulations. It should be noted that the loads applied in the simulations are the half of the load levels given here due to modeling only half of the pipes cross-section. So the 50 kN and 100 kN analysis have been run with 25 kN and 50 kN, respectively. All simulations were run with isotropic hardening and the material parameters can be seen in Table 4.2 in

Section 4.3. The force, in the force-vertical displacement curves, is taken from the indenter in the y-direction.

Table 5.1: Overview of the preliminary numerical simulations. C - constant and LI - linear increasing.

Simulation	**1**	**2**	**3**	**4**	**5**	**6**	**7**	**8**	**9**
Horizontal BC	Free	Free	Free	Free	Free	Free	Free	Free	Fixed
Applied horizontal load [kN]	-	C 50	C 100	LI 50	LI 100	-	C 50	LI 50	-
Internal Pressure [MPa]	-	-	-	-	-	10	10	10	-

As noted in Section 5.3.6, the kinetic energy should only be a small fraction, up to 5 %, of the internal energy for the deforming material. This has been checked for all the numerical analysis and have proved to be satisfying for all analysis. An example can be seen in Figure 5.13 where the kinetic and 5 $\%$ of the internal energy of simulation 2 have been plotted as a function of the step time. The internal energy has been multiplied with 0.05 to get 5 $\%$ that the kinetic energy should be below. It can be seen that the kinetic energy is well below the 5 $\%$ fraction throughout the whole analysis, meaning that the step time could be shorter to increase the computational effiency.

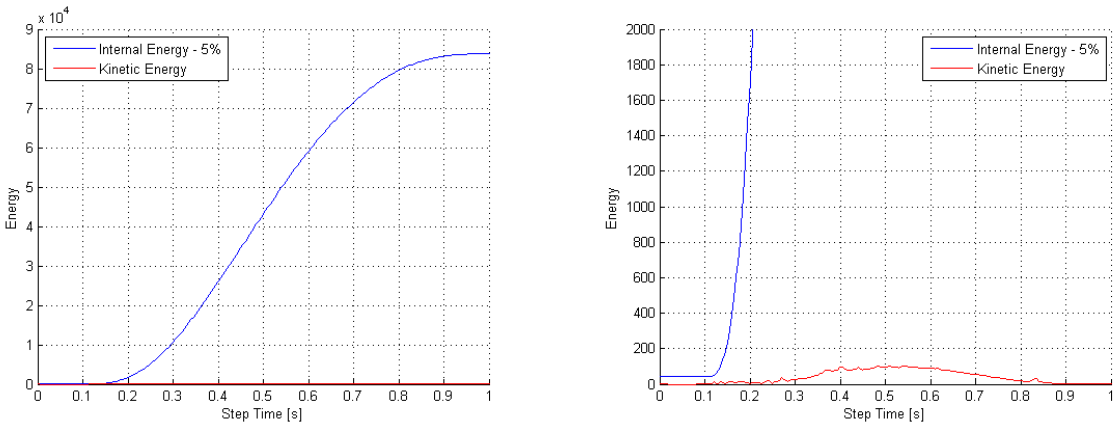

(a) Whole plot. *(b) Partial plot for simplicity.*

Figure 5.13: 5 % of the internal energy vs the kinetic energy for simulation 2.

5.4.1 Non-Pressurized Pipes

In Figure 5.14 vertical force-displacement plots of all the numerical simulations of the non-pressurized pipes can be seen.

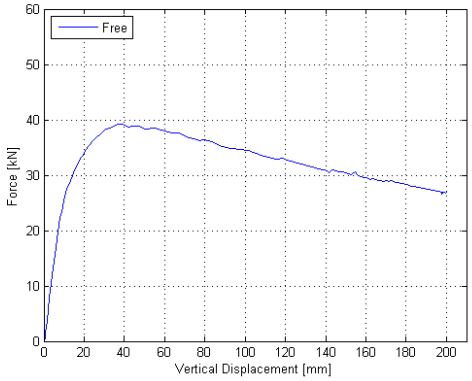

(a) Simulation 1.

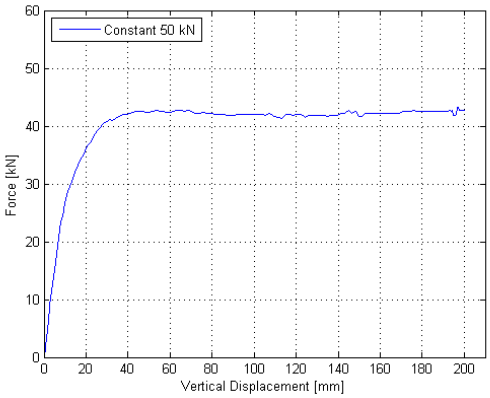

(b) Simulation 2.

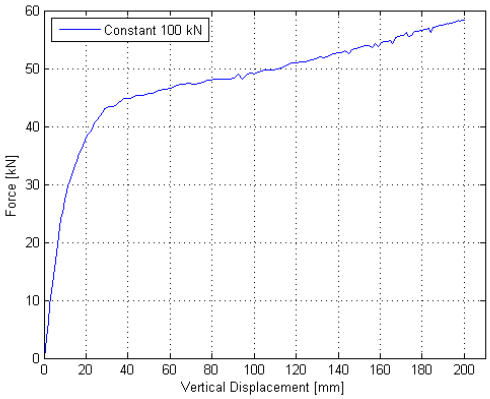

(c) Simulation 3.

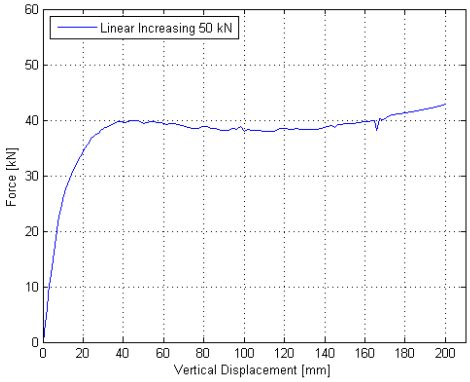

(d) Simulation 4.

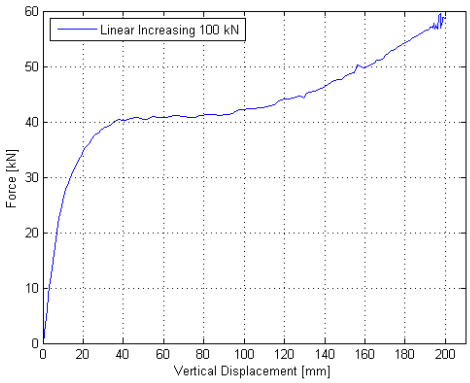

(e) Simulation 5.

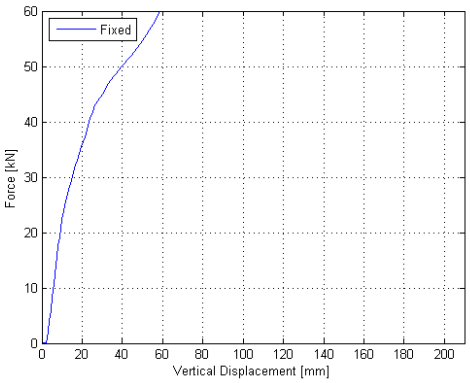

(f) Simulation 9.

Figure 5.14: Non-pressurized simulations. Simulations 1-5 and 9.

In Figure 5.15 the vertical force-displacement plots of all the non-pressurized pipes can be seen plotted together in one graph. Due to the symmetry of the modeled pipe, the force from the numerical simulations have been multiplied with 4 to get the real load.

The peak forces of the different simulations can be seen in Table 5.2. Simulation 1, 4 and 5 that are the free , linear increasing 50 kN and linear increasing 100 kN pipes, respectively, have the lowest peak force. Then simulation 2 that are the constant 50 kN have somewhat higher peak force than simulation 1, 4 and 5. The highest peak force

does simulation 3 have, which is the constant 100 kN simulation. Simulation 9 that is the fixed pipe is following the curves of the other simulations in the beginning but then it just continues to rise. The peak force of simulation 9, the fixed pipe, is not included as this is a somewhat unrealistic simulation considering its boundary condition. Its peak force is higher than what it is possible to apply with the actuators.

At the end of the deformation it is simulation 1 that has the lowest force level. This is expected as it dont have any horizontal forces as the other simulations have. It is of interest to compare the simulations with linear increasing and constant load of the same magnitude. Simulation 2 and 4 have the same force level in the end. This is expected as the horizontal load level here is equal (50 kN). The peak force and the force level for simulation 2 is higher from the peak until the end. This is expected as the constant force applied in simulation 2 give the pipe a higher horizontal load and therefore higher resistance against bending. It is necessary with higher force to get the same displacement level.

The same behaviour is seen for simulation 3 and 5. The constant 100 kN has higher peak force and higher force until the final deformation is reached, where they have equal load levels. It can be seen that the difference between simulation 3 and 5 are bigger than the difference between simulation 2 and 4. This indicates that the pipe is more sensitive to a constant load than a linear increasing load.

It should be noted that simulation 2 has higher peak force than simulation 5 which indicates that a constant load has much greater influence on the peak force than a linear increasing load level.

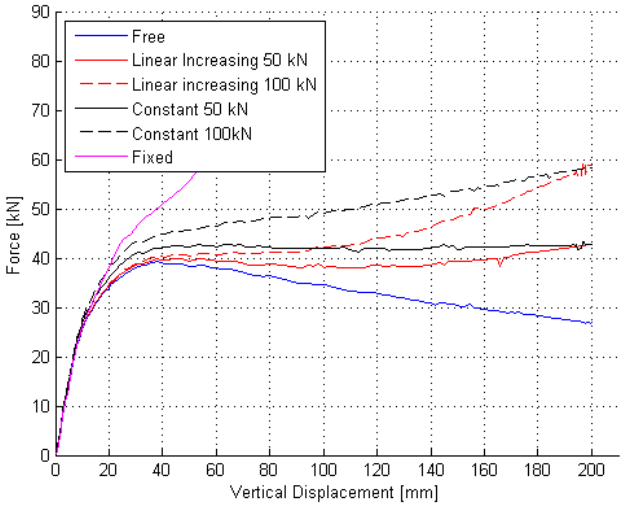

Figure 5.15: Simulation 1-5 and 9.

Table 5.2: Peak forces for simulation 1-5 and 9 and the percentage difference with simulation 1 as a reference.

Simulation	**1**	**2**	**3**	**4**	**5**	**9**
Peak Force [kN]	39.2	42.7	47.3	39.9	40.7	-
Difference	-	8.9 %	20.7 %	1.8 %	3.8 %	-

In Figure 5.16 the horizontal displacement is plotted against the vertical displacement for simulation 1, 2 and 4. Figure 5.16a shows the horizontal displacement-vertical displacement plots for the entire displacement domain, while Figure 5.16b shows a partial area of the domain. It can be seen in both figures that simulation 1, the free pipe, is the upper one. Simulation 4, the linear increasing 50 kN, is in the middle and simulation 2, the constant 50 kN, is the lower one. This behaviour is expected and is similar to that which could be seen in Figure 5.15. At a given vertical displacement the free pipe has the highest horizontal displacement. This is because it doesn't have any horizontal loads applied compared to simulation 2 and 4. It can also be seen that this difference in horizontal displacement is increasing as the vertical displacement increases. It should be noted that the constant load curve is adjusted for the initial negative horizontal displacement due to the applied constant load before bending.

It can be seen that the difference in horizontal displacement between simulation 2 and 4, increases before it decreases. This is as seen in Figure 5.15 and is because simulation 4 has a linear increasing load, where its magnitude of horizontal load is not equal to the one for simulation 2 before final deformation.

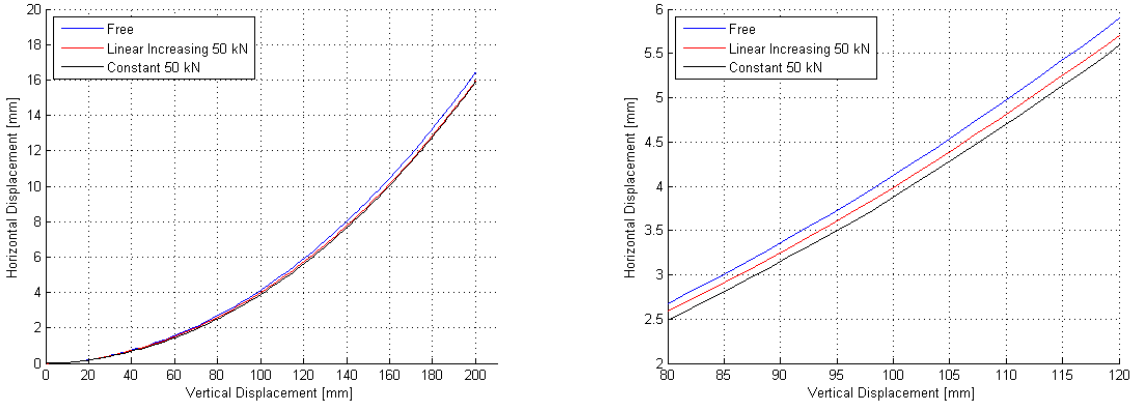

(a) Entire displacement domain. *(b) Partial area of the displacement domain.*

Figure 5.16: Horizontal displacement - vertical displacement for simulations 1, 2 and 4.

5.4.2 Pressurized Pipes

It was first conducted a test where the pipe was only subjected to the pressure load to check that the application of pressure in the pipe was working satisfying. The average von Mises stresses on a pressurized model can be seen in Figure 5.17. It is of interest to compare the stresses and the axial force found analytically in Section 5.2.1 and Section 5.2.3, respectively, with the ones that are found in the numerical simulation.

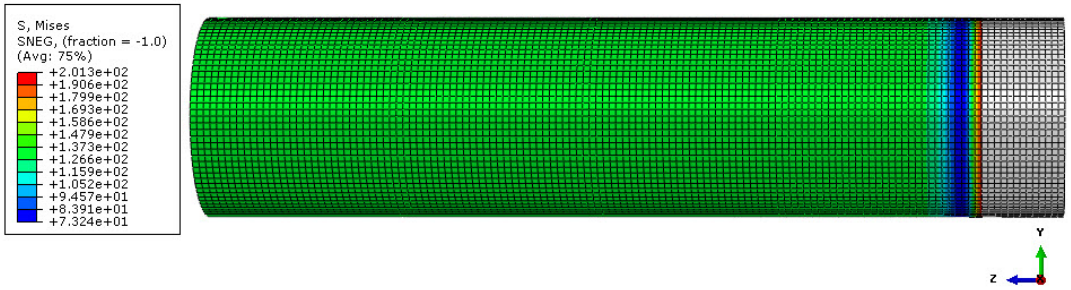

Figure 5.17: Stresses in the pipe due to 10 MPa internal pressure.

The stresses and axial force found analytically and numerically can be seen in Table 5.3. From the numerical simulations σ_{11} is the longitudinal stress σ_l and σ_{22} is the hoop stress σ_h. As can be seen, the stresses and forces have a very good match. This shows that the basis shell model for pressure is working satisfactorily.

Table 5.3: Comparison between numerically and analytically stresses and force from the pressurized pipe.

	Numerical	**Analytical**
Longitudinal stress [MPa]	73.7	73.7
Circumferential stress [MPa]	147.4	147.3
Axial force [kN]	121.5	121.5

In Figure 7.11 vertical force-displacement plots for all the numerical simulations of the pressurized pipes can be seen.

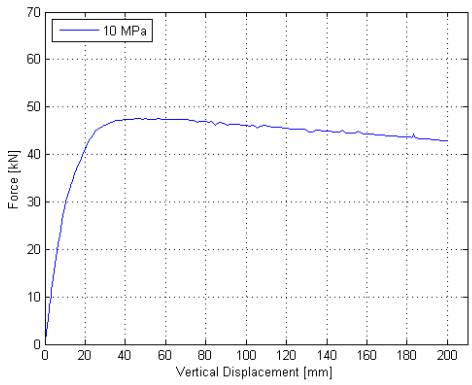

(a) Simulation 6.

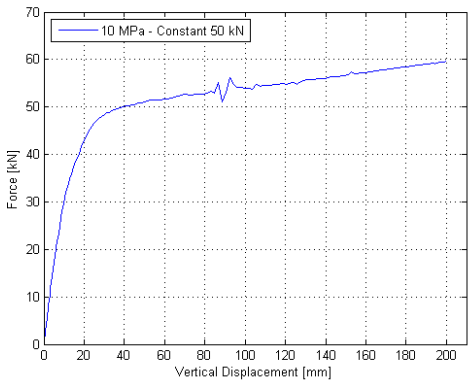

(b) Simulation 7.

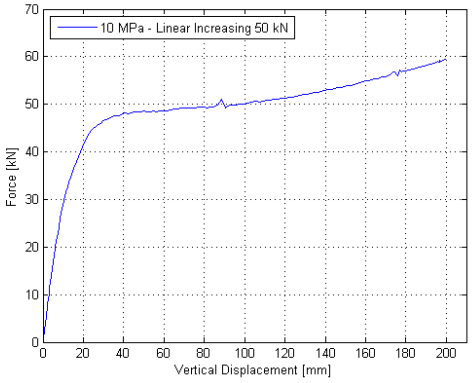

(c) Simulation 8.

Figure 5.18: Force-vertical displacements curves for pressurized simulations. Simulations 6-8.

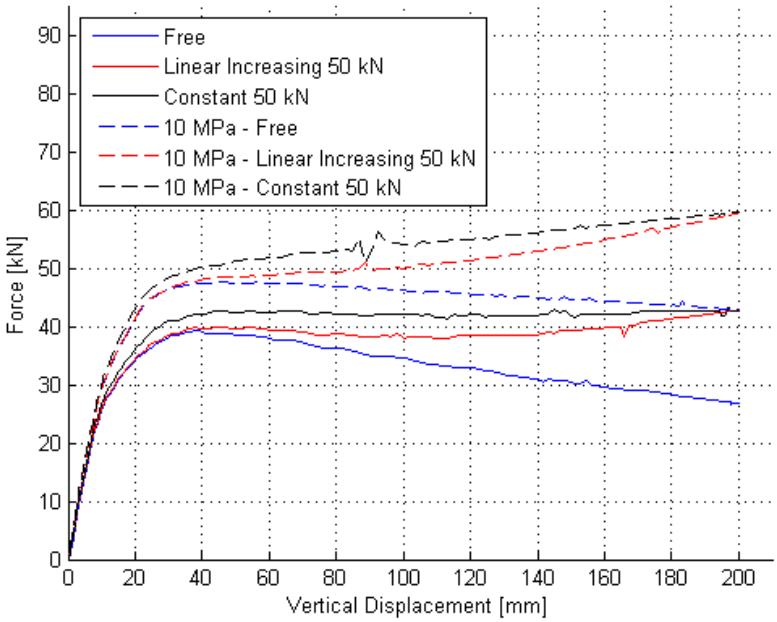

Figure 5.19: Force-vertical displacement plots of simulations 1, 2, 4, 6, 7 and 8.

In Figure 5.19 simulations 1, 2, 4, 6, 7 and 8 have been plotted. That is bending of the

free pipe with and without inner pressure, bending with a linear increasing load from 0 - 50 kN with and without inner pressure and bending with a constant load of 50 kN with and without pressure. It can be seen that the pressurized pipes have a larger peak force than the non-pressurized pipes. This is expected as the inner-pressure make the pipe more resistance against global bending.

A comparison of the peak-forces between the non-pressurized pipes and pressurized pipes with the same load levels can be seen in Table 5.4. As seen there is a significant difference in peak force for the simulations with equal horizontal loads applied, but with and without inner pressure applied. E.g. the peak force of the pressurized simulation of the free pipe is 21.4 % higher than the simulation of the free pipe without pressure. This indicates that the global response of the pipes are highly dependent on being pressurized or not.

Table 5.4: Comparison of peak forces for pipes with the same load levels.

Load	Free		C 50 kN		LI 50 kN	
Simulation	1	6	2	7	4	8
Pressure [MPa]	-	10	-	10	-	10
Peak force [kN]	39.2	47.6	42.7	51.5	39.9	48.5
Increase	-	21.4%	-	20.6 %	-	21.6%

It is of interest to see how different loading conditions will affect the deformation of the cross-section of the pipes at the midpoint and how the distribution of the equivalent plastic strains are. In Figure 5.20 the equivalent plastic strains of simulation 1, 4 and 8 can be seen. These are the pipes with no horizontal load, linear increasing horizontal load from $0 - 50\ kN$, and $10\ MPa$ inner pressure with linear increasing horizontal load from $0 - 50\ kN$, respectively.

It can be seen that simulation 1 and 4 are almost equal both regarding the equivalent plastic strains and the deformation mode. Simulation 8 has a less deformed cross section than simulation 1 and 4 and the equivalent plastic strains are smaller. The distribution of the plastic strains are equal for simulation 1 and 4 while it is spread more backward in the pipe for simulation 8, indicating more local deformation for this simulation. These observations are expected as the inner pressure gives more resistance against global deformation, so simulation 8 will have different local deformation than simulation 1 and 4.

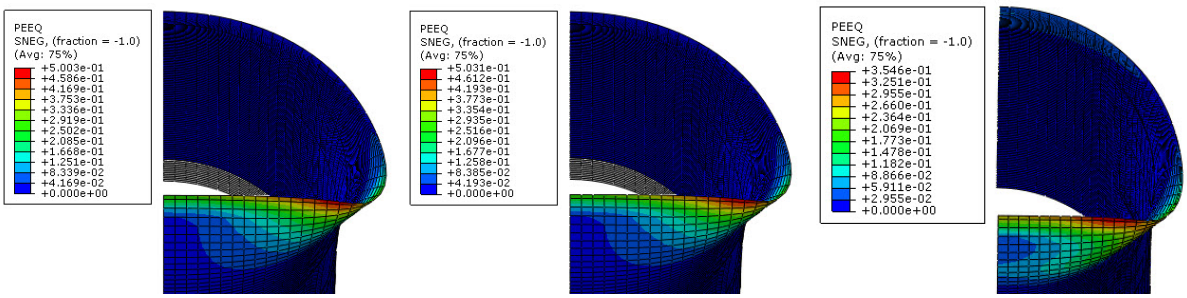

(a) Simulation 1. *(b) Simulation 4.* *(c) Simulation 8.*

Figure 5.20: Deformed cross-section at mid-point of simulation 1, 4 and 8 showing the equivalent plastic strain on the inside of the pipe.

Chapter 6

Experimental Testing

Experimental testing has been performed on three pipes. The experiments have been carried out by deforming the pipes laterally with different horizontal loading conditions. As these experiments are a continuation of the work carried out by Asheim and Mogstad [6] the pipes have been labeled pipe 4-6. Digital Image Correlation have been utilized to monitor the strains near the dent outside of the pipes. Data registered during experiments will later be used for validation of numerical models.

6.1 Measurements of the Pipes

The thickness and the inner diameter of the pipes have been measured before testing. An overview of where the thickness measurements have been done can be seen in Figure 6.1. The thickness has been measured at 8 positions along the circumference of the pipe. This has been done at 5 locations, marked as 1-5, over the length of the pipe. Measurements of the inner diameter were performed at 4 positions, on both ends, marked as end 1 and end 2.

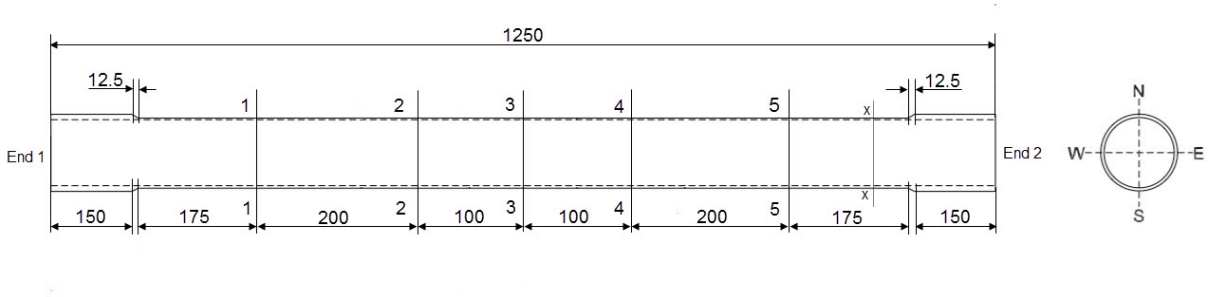

Figure 6.1: Overview of locations of measurements.

Before measuring the thickness it could be seen that pipe 5 had been lathed extra thin over a certain area. It was therefore decided to do extra measurements in this area.

An x can be seen in Figure 6.1, where the extra measurements were conducted. This was done to see how much this would affect the average thickness. In total, 8 extra measurements were done. Table 6.1 and Table 6.2 shows the average thicknesses and inner diameters of the pipes, respectively. The variance and standard deviation can also be seen.

A certain deviation can be seen for the average thicknesses of the pipes. It is specially the average thickness of pipe 6 that is deviating from the average thickness of the other pipes. For pipe 5 with the extra measurement, it can be seen that the difference is not significant whether the extra measurements are included or not. This indicates that the area that was lathed extra, should not affect the results of the experiments in particular.

Since the flange was already welded onto pipe 4 before measuring, it was not possible to measure the inner diameter. It can however be seen that the average inner diameter of pipe 5 and 6 are very similar. So it is reasonable to assume that pipe 4 will have an inner diameter that is similar.

It is referred to Appendix A for all the measurements of the pipes.

*Table 6.1: Measurements of thickness of pipe 4-6. * includes the extra measurements of pipe 5.*

Pipe	4	5	5*	6
t_{avg}(mm)	4.20	4.19	4.16	4.06
Var(t)[mm^2]	0.0368	0.0652	0.0656	0.0508
St.dev(t)[mm]	0.1918	0.2553	0.2560	0.2253

*Table 6.2: Measurements of diameters of pipe 4-6. * not possible to measure.*

Pipe	4*	5	6
Inner Diameter$_{avg}$	-	122.41	122.20
Var(D)[mm^2]	-	0.0158	0.0547
St.dev(D)[mm]	-	0.1260	0.2339

6.2 Digital Image Correlation

It was decided to utilize Digital Image Correlation (DIC) during the experimental testing in the stretch bending rig. This will give the opportunity to monitor the strains near the dent at the outside of the pipes, which will give the oppurtunity to compare this with the numerical results and validate them. The following short review about DIC is based on two publications by E. Fagerholt [23, 24].

The basic principle of DIC is based on finding the correlation between a reference image (undeformed state) of the specimen and the current image (deformed state) of the specimen, i.e. an image at a deformed stage. By optimizing a set of degress of freedom for a pixel subset, correlation is found. This is done by minimizing the sum of gray value differences between two images within the particular subset. Instead of finding the correlation for each point (or subset) individually, which is the traditional DIC approach, correlation can be carried out globally for a set of nodes contained in a "finite element" mesh [23]. Here the grayscale residuals within the region covered by the mesh, have been minimized, by optimizing the nodal displacements. In Figure 6.2 the experimental setup with the cameras used to capture the images for DIC and the pipe with the gray painted area, can be seen.

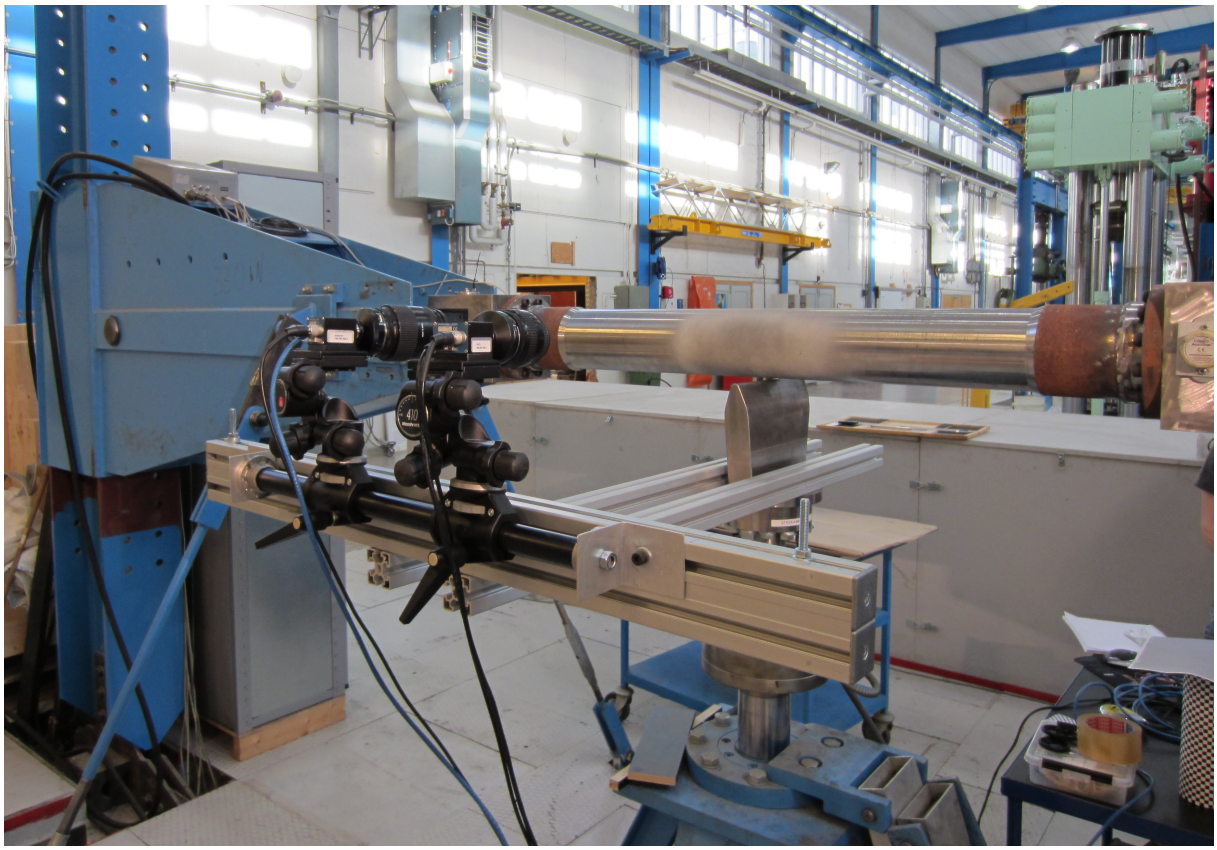

Figure 6.2: Overview of the setup for Digital Image Correlation.

The post-processing of the image series from the experimental testing were carried out by using an in-house DIC code (at SIMLab), which provided displacement and strain fields of the specimen surface near the dent. Due to some experimental issues with the cameras, when monitioring pipe 4, these results were not very good. However, the results for pipe 5 and 6 was reasonably good. The lighting was not optimal so it became some shading on the DIC images, however without degrading the results noticeably.

6.3 Experiments

The tests have been carried out at the stretch bending rig at the test laboratory of SIMLab at Department of Structural Engineering, NTNU. For a review of the stretch bending rig and bending of the pipes in the rig, see Section 5.1. Three tests were carried out, one on each of the pipes. The pipes were bent laterally to a deformation of 200 mm with different horizontal loading conditions. In Figure 6.3, pipe 4 can be seen while it is being bent by the indenter. It should be noted that the horizontal load is not following the rotation of the pipe, so it is not equal to the axial load in the pipes.

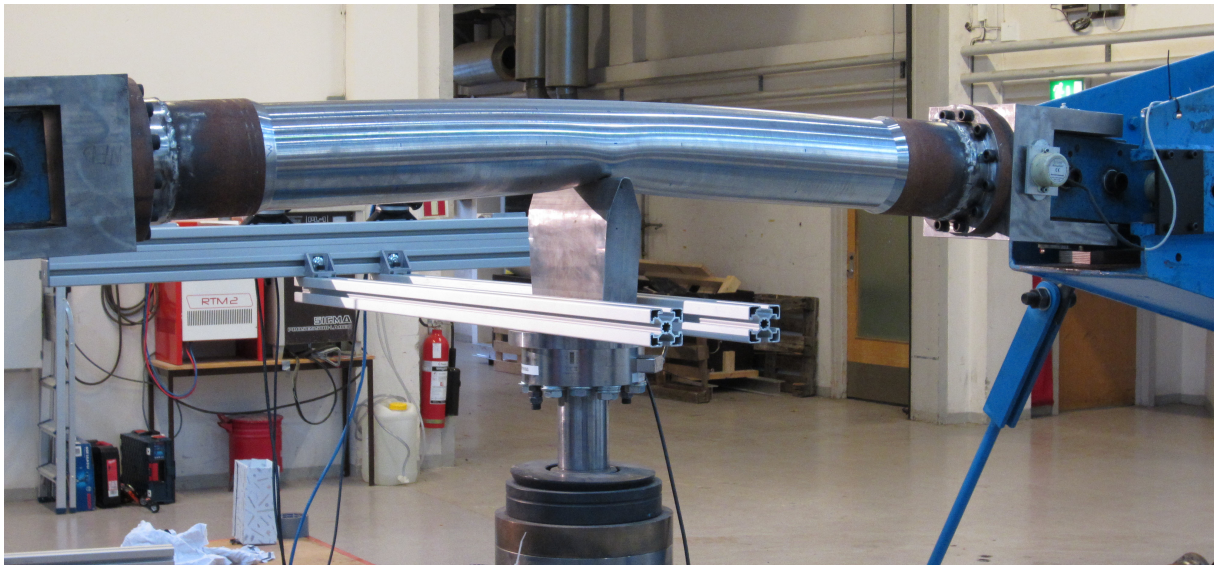

Figure 6.3: Bending of pipe 4.

Pipe 4 was deformed 200 mm with a deformation rate of 25 mm/min. The pipe was free to move horizontally and no horizontal load were applied during the deformation. After the final deformation was reached the horizontal actuators were fixed and the indenter was lowered back to initial position. Then the horizontal actuators were released and the pipe could deform into the final deformed shape.

Pipe 5 was deformed 200 mm with a deformation rate of 25 mm/min. A horizontal load of 50 kN was initially planned, but due to some small issues with the stretch-bending rig a horizontal load of 53 kN was applied instead. This load was then held constant during deformation. After the final deformation was reached the horizontal actuators were fixed and the indenter was lowered back to initial position. Then the horizontal actuators were released and the pipe could deform into the final deformed shape.

Pipe 6 was deformed 200 mm with a deformation rate of 25 mm/min. The pipe was initially planned to be subjected to a linearly increasing horizontal load from 0 - 50 kN during bending. Due to some small issues with the stretch-bending rig a linearly increasing load from 0 - 53.1 kN was applied instead. After final deformation was

reached the horizontal actuators were fixed and the indenter was lowered back to initial position. Then the horizontal actuators were released and the pipe could deform into the final deformed shape.

The most important parameters that have been logged against time, are the vertical and horizontal forces and vertical and horizontal displacements. In addition, the angle of the rotational joints was logged. A summary of the parameters used in the experimental tests can be seen in Table 6.3.

Table 6.3: Experimental parameters. C-constant and LI-linear increasing.

Pipe	4	5	6
Horizontal load [kN]	-	LI 53	C 53.1
Deformation rate [mm/min]	25	25	25
Deformation [mm]	200	200	200

6.4 Results

In Figure 6.4, the force-vertical displacement curves from the experimental testing of pipe 4-6 are shown. It can be seen that the curves are similar in the beginning of the deformation, but as test 4 and 6 are starting to deflect and reach peak force, test 5 continue to rise. Test 4 and 6 have peak forces of 40.7 kN and 40.6 kN, respectively, while test 5 has a significantly higher peak force of 45.9 kN. After peak force are reached the force of test 4 decreases constant until final deformation are reached. The force of test 6 decreases before it starts to increase and ends up with a load level that are almost equal to the one of test 5. Test 5 have an almost constant force level after peak force.

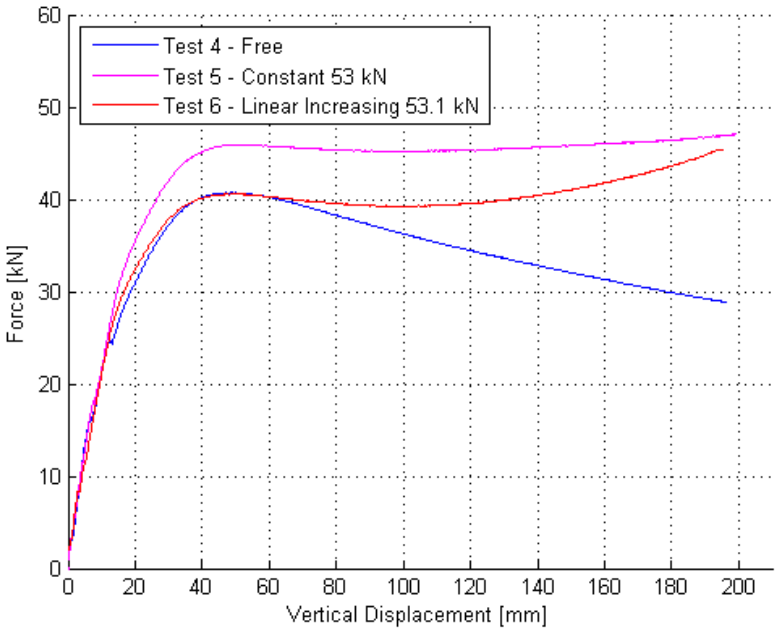

Figure 6.4: Force-vertical displacement curves for pipe 4-6.

In Figure 6.5, the pipes can be seen next to eachother after they have been deformed in the stretch bending rig. No external fracture could be observed when doing a visual inspection of the outside of the pipes after bending. A photo series from one of the DIC cameras capturing the bending of pipe 5 at different deformations levels throughout the bending of the pipe can be seen in Figure 6.6.

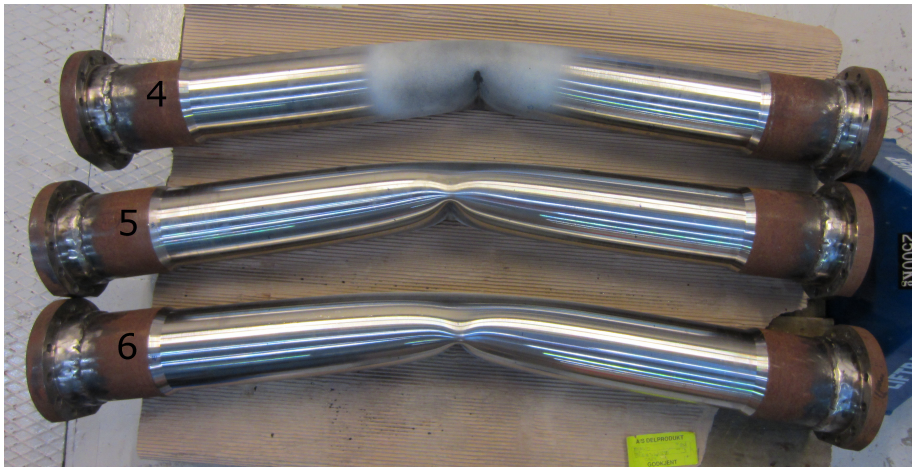

Figure 6.5: Pipe 4-6 seen after the experimental testing.

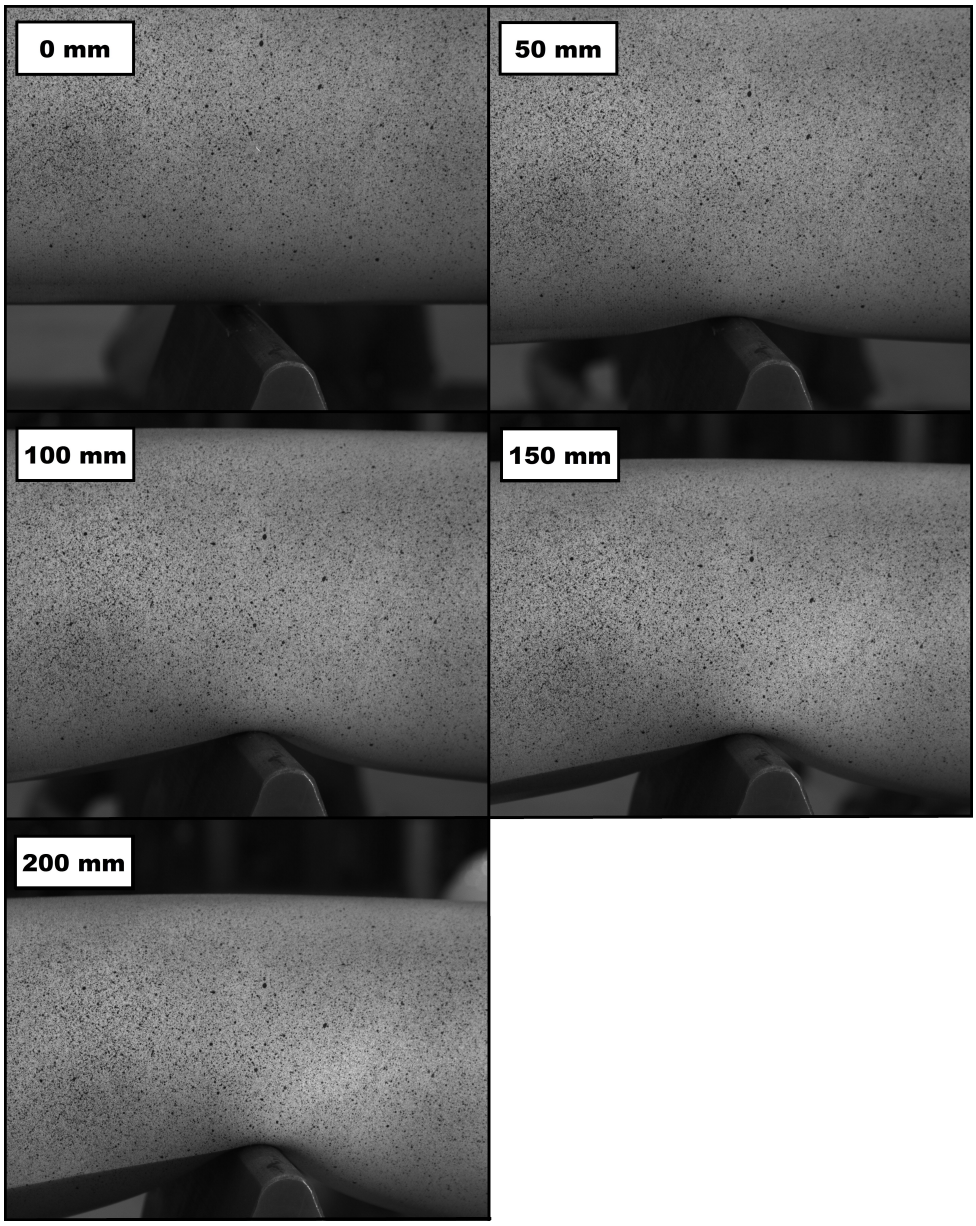

Figure 6.6: Photo series of the bending of pipe 5 at different deformation levels.

Chapter 7

Finite Element Analysis

It has first been done a comparison between the preliminary numerical simulations with the results from the experimental testing on the pipes. This has been done to highlight any differences that are significance. To get further knowledge about how different parameters influence the results, it has been carried out parameter studies. Based on this, optimized numerical models was established and simulations were carried out to validate the finite element method approach to the problem. It was carried out one simualtion specified for each of the pipe with it's corresponding horizontal loading. Shell elements were used for the simulations.

For a review of the most important theory related to FEM, it is reffered to the other theses [3, 4, 5, 6], as they have covered this topic very well.

7.1 Comparison of Preliminary Numerical Simulations with Experimental Results

A comparison between the results from the experimental testing and preliminary numerical simulation of pipe 4 can be seen in Figure 7.1. The curves are identical in the beginning before the curve oftest 4 has two places where it flattens out a bit. The reason for the flattening is thought to be either local buckling of the pipe, or issues with the experimental setup since this was the first experimental test to be carried out. The issue with the experimental setup can be problems with the boundary conditions e.g. sliding of the horizontal fastening of the pipe. This will not affect the global response to any certain degree.

The peak force of test 4 and the numerical simulation are 40.7 kN and 39.2 kN, respectively. A reasonable explanation for this insignificant difference can be explained

by the fact that the average measured thickness of pipe 4 is 4.20 mm, while the numerical simulation was carried out with a thickness of 4.15 mm. This means that the pipe in the test, probably will have higher stiffness than the pipe in the numerical simulation. After peak force, the curves behave similary.

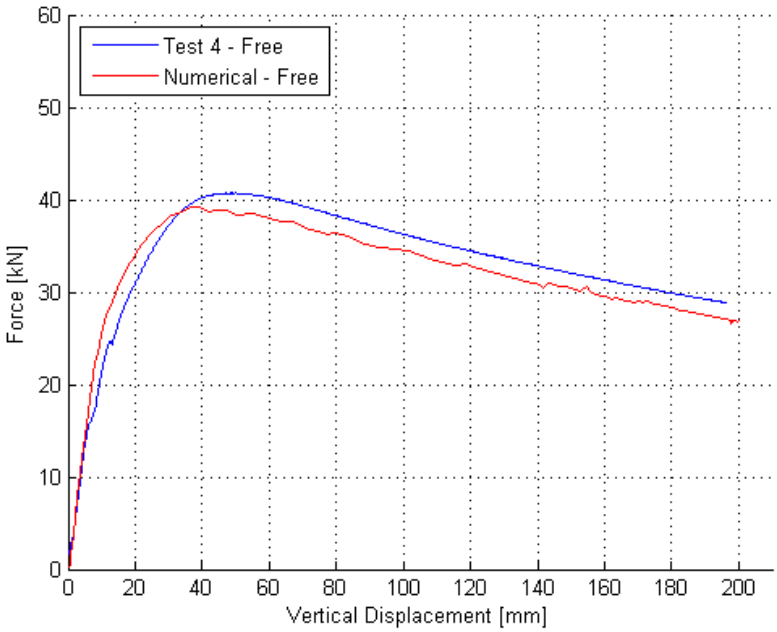

Figure 7.1: Comparison between experimental testing and preliminary numerical simulation of pipe 4.

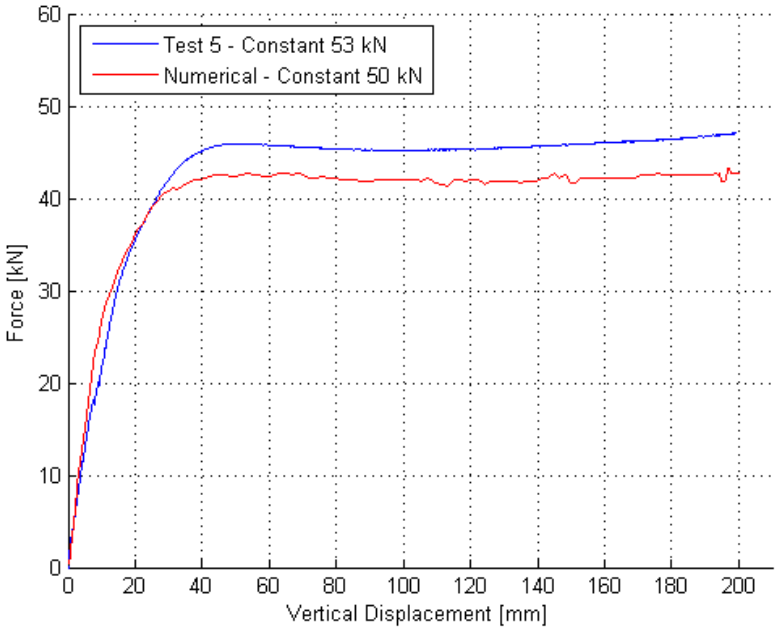

Figure 7.2: Comparison between experimental testing and preliminary numerical simulation of pipe 5.

In Figure 7.2, a comparison between the results from the experimental testing and the preliminary numerical simulation of pipe 5 can be seen. In the beginning the numerical simulation has a slightly stiffer behaviour than the test. The peak forces of test 5 and the numerical simulation are 45.9 kN and 42.7 kN, respectively. So the test has a considerable stiffer behaviour than the simulation. The stiffer behaviour have two reasonable contributions. The test was conducted with a constant load level of 53 kN, and the numerical simulation was conducted with a constant load level of 50 kN. The average measured thickness of the pipe are 4.19 mm and 4.16 mm with and without the extra measurement, respectively, while a thickness of 4.15 mm has been used in the numerical simulation. After peak force the curves decrease slightly before they slightly increase. The test curve increase a bit more than the numerical curve, this is probably due to the higher constant applied horizontal load.

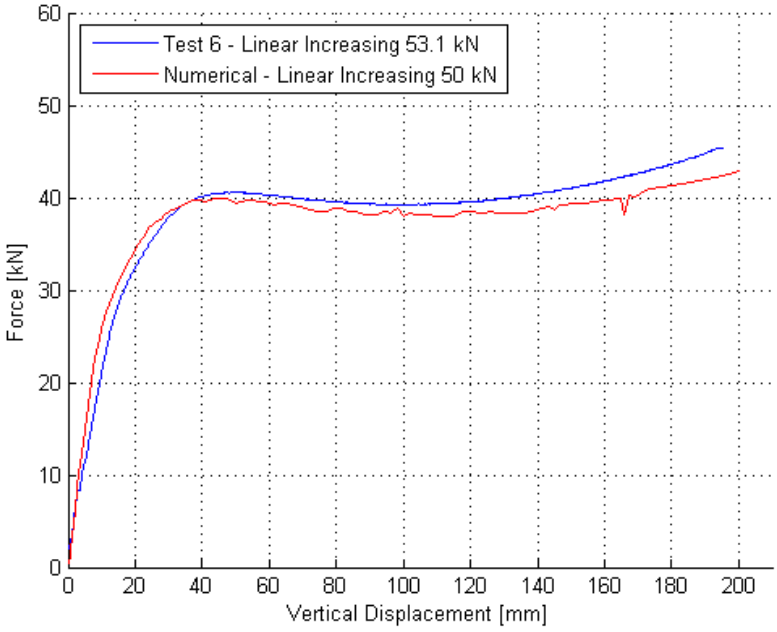

Figure 7.3: Comparison between experimental testing and preliminary numerical simulation of pipe 6.

A comparison between the results of the experimental testing and preliminary numerical simulation of pipe 6 can be seen in Figure 7.3. Up to peak force, the numerical simulation has a slightly stiffer behaviour. The peak force is 40.6 kN and 39.9 kN for the test and the numerical simulation, respectively. A difference that is not significant. An average measured thickness of 4.06 mm should indicate that the peak force of the test should be lower than the peak force of the numerical simulation, since the numerical simulation was conducted with a thickness of 4.15 mm. But, since the test was carried out with a linear increasing load from 0-53.1 kN and the numerical with a linear increasing load from 0-50 kN, it seems to contribute to a higher peak force for the test. After peak force, both curves decrease, before they increase. The test increase slightly

more than the numerical simulation because of a higher load applied.

In Table 7.1, a comparison between the peak forces of the experimental test and the corresponding numerical simulations can be seen. The difference in peak forces of the free and linear increasing 0-50 kN numerical simulations compared to the experimental test result are 3.7 % and 1.7 %, respectively. This is not significant. The difference in peak force of 7.0 % between the numerical simulation with constant horizontal 50 kN load applied and test 5 is however significant. A thicker pipe and higher applied horizontal load are pointed out to be the reason for this difference.

Table 7.1: Comparison of peak forces from numerical simulations and experimental testing. C - constant and LI - linear increasing. The difference in % is the numerical simulation compared with its corresponding experimental test.

	Test 4	Free	Test 5	C 50 kN	Test 6	LI 50 kN
Peak force [kN]	40.7	39.2	45.9	42.7	40.6	39.9
Difference	-	3.7 %	-	7.0 %	-	1.7 %

7.2 Concluding Remarks to the Experiments

Force-vertical displacement curves from the experimental testing of the pipes are in overall approximately similar with the results from the numerical simulation. The deviations can be explained by the fact that some of the parameters in the numerical simulations differ from the one in the experiments. Both thickness and applied horizontal load have been different. The behaviour of the numerical simulations after the peak force is very similar to the tests. This shows that the material model used in the numerical simulations capture the material behaviour in a satisfying manner.

7.3 Parameter Studies

In Section 7.1, where the results from the preliminary numerical simulations have been compared to the experimental results, it was observed that some parameters have a high influence on the results. It is of interest to investigate this further by performing parameter studies to see how different parameters will affect the results of the simulations. The examined parameters have been changed one at a time while the rest of the parameters have been kept constant. The parameters that have been studied are the element size, pipe thickness, friction between pipe and indenter and the amplitude of the load and deformation of the indenter. The three first studies have been conducted on simulation 1, while the last have been conducted on simulation 4.

Element Size

The preliminary numerical simulations were carried out with 4 mm S4R elements giving 5 712 elements on the deformable part. Simulation 1 have been carried out with 3 mm and 2 mm S4R elements, giving 10 112 and 22 848 elements on the deformable part, respectively. This has been done to see if the result will show convergence.

It could be seen from the results shown in Figure 7.4 that the curves are very similar. This shows that the mesh size has little influence on the global response, below a certain element size. This is supported by the mesh sensitivity analysis conducted by Slåttedalen and Ørmen [3].

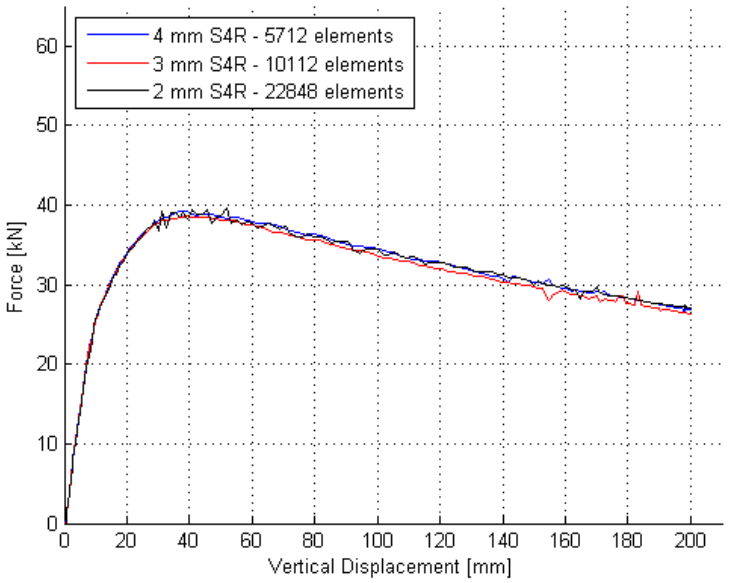

Figure 7.4: Mesh sensitivity study of simulation 1.

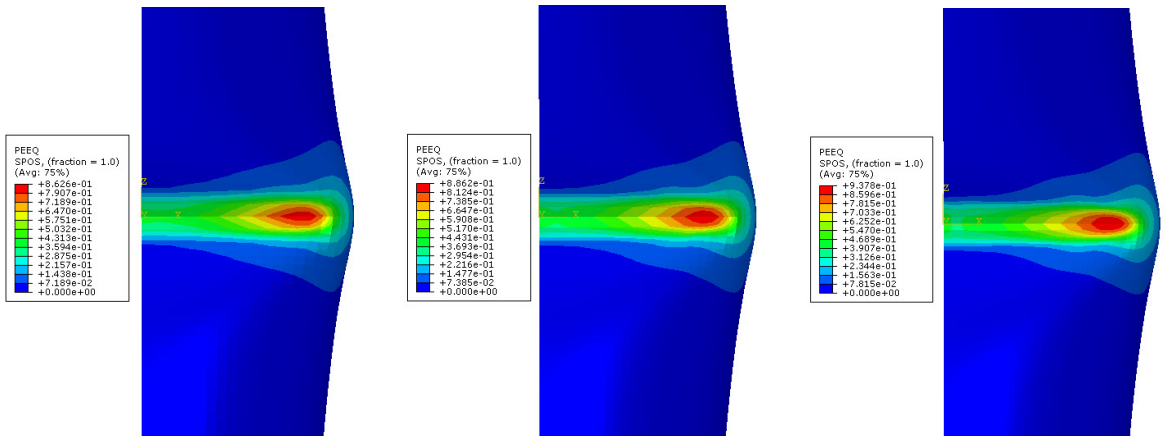

(a) 4 mm *(b) 3 mm* *(c) 2 mm*

Figure 7.5: Equivalent plastic strain from the outer surface of the deformed pipe for simulation 1.

However, an analysis of the plastic equivalent strain, reveals that the magnitude of

equivalent plastic strain is sensitive to the element size. The plastic equivalent strain of the mid-section of the deformed pipe, with different element sizes, can be seen in Figure 7.5. It can be seen that the magnitude of plastic equivalent strain increase as the element size decrease.

Thickness of Pipe

The numerical simulations were carried out with a thickness of 4.15 mm. To see how a variation in thickness will influence the results, simulation 1 has been carried out with a thickness of 3.90 mm and 4.40 mm. This is $\pm$ one standard deviation of pipe 6 from the thickness of 4.15 mm. The vertical force-displacement plots can be seen in Figure 7.6.

As seen, the thickness of the pipe have a highly significant influence on the force-displacement curve from the numerical simulation. In the beginning, the curves have the same slope, but they start to differ, as the slope starts to decrease. The peak forces differ significantly. After peak force, the curves are similar in shape but the force level is higher for the pipe with thickness 4.40 mm and lower for the pipe with thickness 3.90 mm, when compared to the simulation with thickness 4.15 mm, which is according to the expectations.

Table 7.2 provides an overview over the differences in thickness and peak forces. It can e.g. be seen that a 6.0 % increase in thickness of the pipe gives an increase in the peak force of 8.7 %.

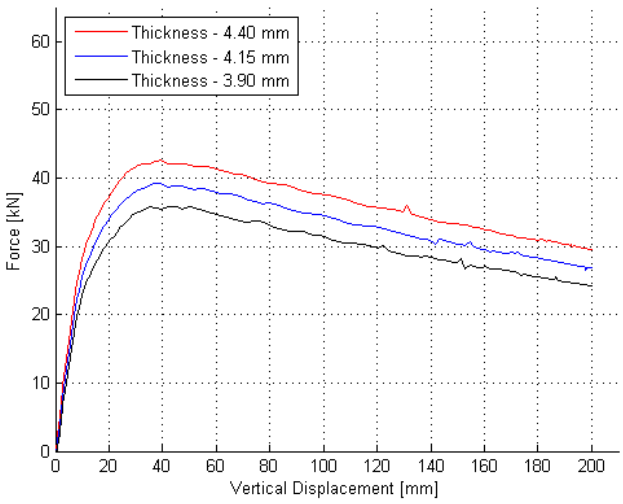

Figure 7.6: Simulation 1 carried out with three different thicknesses.

Table 7.2: Simulation 1 carried out with different thicknesses.

Thickness [mm]	3.90	4.15	4.40
Difference Thickness	-6.0 %	-	6.0 %
Peak force [kN]	35.8	39.2	42.6
Difference Peak Force	-8.7%	-	8.7%

Friction

The numerical simulations have been carried out without friction in the interaction between the indenter and the deformable part. To see if friction will affect the numerical results, simulation 1 was carried out with friction applied to the interaction between the indenter and deformable part. The friction coefficient was set to be 0.42 and 0.78. This is the kinetic and static friction coefficients for steel against steel [25], respectively. The results shown in Figure 7.7 indicate that applying friction has no influence on the global response as the curves are almost identical.

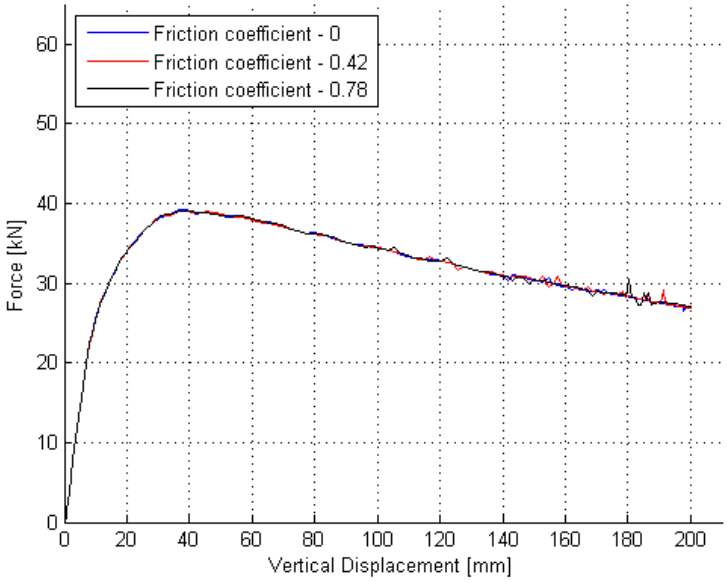

Figure 7.7: Simulation 1 performed with three different friction coefficients.

Smooth and Linear Amplitude

It was of interest to see if there would be any difference in the results when comparing smooth and linear amplitude applied to the linear load and to the deformation with the indenter. It is reffered to Abaqus user manual [17] for a review of the smooth amplitude.

Simulation 4, bending with linear increasing horizontal load from 0 - 50 kN, has been carried out with a smooth amplitude of the linear load. The horizontal linear load in the experiments was performed with linear amplitude. It is therefore of interest to see if the numerical results will differ in terms of what kind of amplitude that has been applied to

the horizontal load. In Figure 7.8a, simulation 4 can be seen carried out with linear and smooth amplitude and the result from the experimental testing. The curves from the simulations are almost identical up to the peak forces that are 39.9 kN and 40.5 kN, for the simulation with smooth and linear amplitude, respectively. In the last half of the deformation range the curves starts to differ from each other, and in the end, the slope of the linear amplitude curve is higher than the slope of the smooth amplitude curve. To see which of these amplitudes that captures the behaviour of the experimental test in a best manner, the results have to be compared with the experimental results of pipe 6. It can be seen that the simulation with the smooth amplitude is closer to the test in the last half of the deformation range, but the linear amplitude captures the behaviour of the test in a better way.

The amplitude of the bending of the pipe with the indenter, have been carried out with a smooth amplitude in the preliminary studies. Since the experiments were carried out with a linear amplitude applied to the indenter, it is of interest to see if the result will deviate with different amplitudes. In Figure 7.8b, simulation 1 have been carried out with smooth and linear amplitude applied to the deformation with the indenter. The corresponding experimental test result have also been plotted. It can be seen that the force-displacement curves for smooth and linear amplitude are identical. This means that the response of the pipe is captured equally, independent of which of the two amplitudes that are applied.

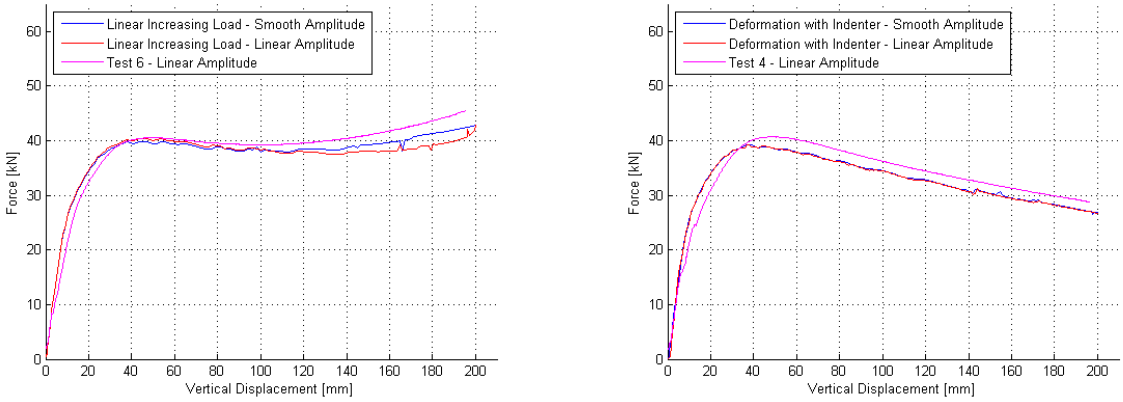

(a) Horizontal load. *(b) Deformation with indenter.*

Figure 7.8: Parameter studies of smooth and linear amplitude.

7.4 Final Numerical Analyses on Optimized Models

Based on the preliminary studies, experimental results and the parameter studies, it will be established and carried out numerical simulations of optimized models. It will be done one simulation for each of the three experiments with the objective of finding

the best solution in terms of recreating the experimental results in the best possible way.

7.4.1 Optimized Models

To establish the optimized models, the basis model that was used in the preliminary studies, established in Section 5.1.2, will be used as a base. There will be done some changes, and to obtain better numerical results it will be made one specific model for each of the load cases.

From the parameter study it was observed that the thickness had a significant influence on the global response. It was therefore decided to use the average measured thickness of each pipe, as seen in Table 4, to the associated numerical simulation. The inner diameter varies little between the pipes and it does not affect the results significantly, so it is kept at 122.3 mm.

Since the local plastic equivalent strain is much more sensitive to the mesh size than the global response its decided to have a refined mesh at the middle of the pipe where the plastic strains are of significance. An overview of the mesh can be seen in Figure 7.9. The coarse part with length 320 mm was meshed with 4 mm S4R elements while the fine part with length 150 mm was meshed with 2 mm S4R elements. A transition zone was seeded with single bias to get a smooth transition from the coarse to the fine part of the mesh. The total number of elements for the different optimized models can be seen in Table 7.3.

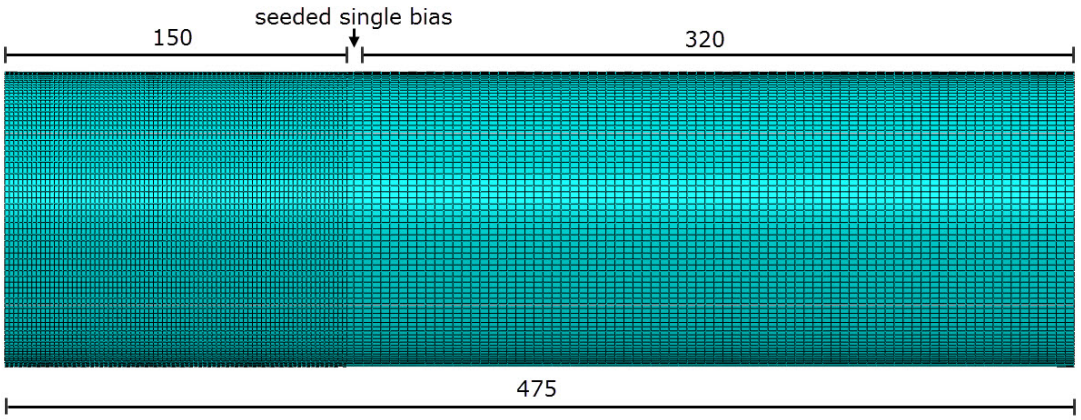

Figure 7.9: Mesh of the deformable part for the optmized model. Measurements in mm.

The load levels have been changed according to the experimental testing. So a constant load of 53 kN will be applied to pipe 5, while pipe 6 will be applied a linear increasing load from 0-53.1 kN. For the numerical simulation of pipe 5 the loading of the linear increasing load will be performed with a linear amplitude instead of the

smooth amplitude that was used in the preliminary studies. It was seen in the parameter studies that the linear amplitude captures the behaviour of the experiment better than the smooth amplitude in the last half of the deformation range. The deformation of the indenter will also be performed with a linear amplitude. The parameter study did not show any difference between linear and smooth amplitude, but as the experiments were performed with a linear amplitude, will this be most similar to the experiments.

The material parameters, seen in Table 7.3, will be the same as used in the preliminary numerical simulations.

A summary of the parameters that have been changed w.r.t the basis model are given in Table 7.3.

Table 7.3: Overview of parameters that have been changed in the optimized numerical models. C - constant and LI - linear increasing.

Simulation	I	II	III
Pipe	4	5	6
Horizontal load [kN]	-	C 53	LI 0 - 53.1
Thickness [mm]	4.20	4.19	4.06
Deformation [mm]	200	200	200
# Elements	11 775	11 775	11 618

It is referred to Section 5.3 for further details on the basis model.

7.4.2 Results of the Final Numerical Simulations

There has been carried out numerical simulations of the pipes as established in Section 7.4.1.

As noted in Section 5.3.6 the kinetic energy should only be a small fraction, up to 5 %, of the internal energy for the deforming material. This has been checked for the numerical simulations I-III, and have proved to be satisfying for all the analyses. An example can be seen in Figure 7.10 where the kinetic and internal energy of simulation III have been plotted as a function of the step time. The internal energy have been multiplied with 0.05 to get a curve representing 5 $\%$ of the internal energy, which the kinetic energy should be below. Except in the very beginning, it can be seen that the kinetic energy is below the 5 % fraction of the internal energy throughout the analysis.

The reason why the kinetic energy is higher than the internal energy in the beginning is probably due to the fact that a linear amplitude is being used instead of a smooth amplitude. The preliminary studies was run with a smooth amplitude, meaning the

initial velocity of the indenter is zero. In this case the kinetic energy was lower than the internal energy initially in the simulation, this can e.g. be seen in Figure 5.13b.

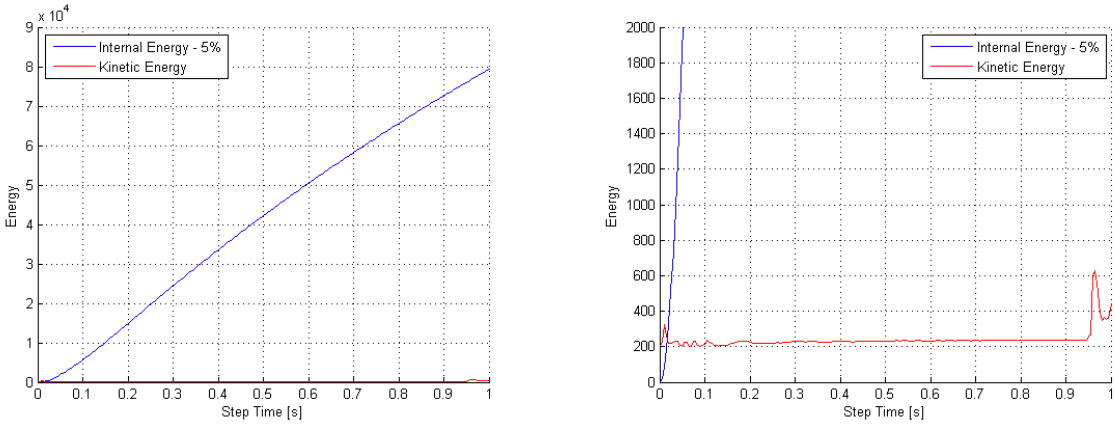

(a) Whole plot. *(b) Partial plot for simplicity.*

Figure 7.10: 5 % of the internal energy vs the kinetic energy for simulation III.

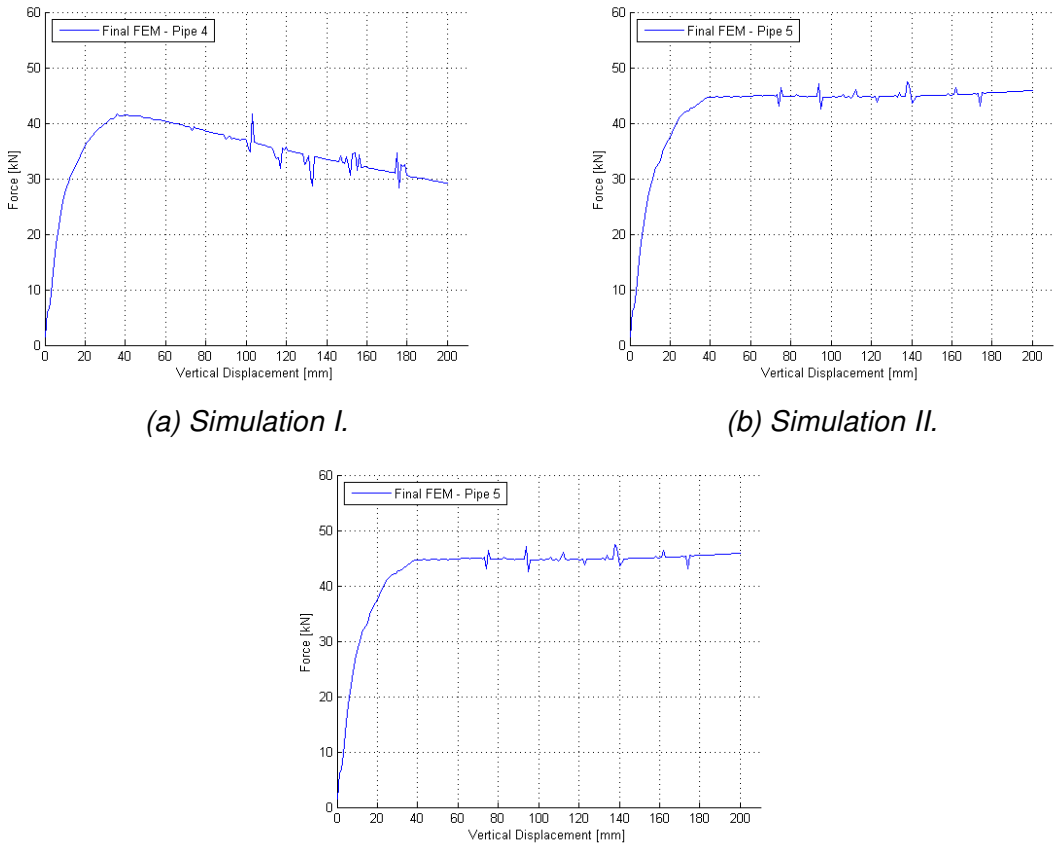

(a) Simulation I. *(b) Simulation II.*

(c) Simulation III.

Figure 7.11: Final numerical simulations of the pipes.

Force-vertical displacement curves for the simulations can be seen in Figure 7.11. It can be observed that the curves have some instabilities in the last half of the deformation range. This is numerical noise which do not effect the global response of the

simulations. It is thought that the noise has something to do with the contact between the indenter and the deformable part of the pipe.

Force-vertical displacement curves of the experimental test of pipe 4 plotted with the corresponding optimized and preliminary numerical simulations can be seen in Figure 7.12. The numerical simulations have a higher initial stiffness than the experimental test. As mentioned in Section 7.1 this is probably due to local buckling of the pipe or issues with the experimental testing. The preliminary and final numerical simulation are equal in the beginning but moves away from each other and they have different peak forces. After the peak force they have an equal behaviour, but there is an approximately constant difference in the load level at a given displacement. It can be seen that the optimized simulation I captures the behaviour of test 4 better than the preliminary numerical simulation.

The peak force of simulation I is 41.4 kN which is 1.7 % higher than the peak force of test 4 of 40.7 kN. Simulation I captures the behaviour of the test very well after peak force and there is only a slight difference between the results.

This means that the changes made on basis of the parameter studies and the actual testing parameters were successful and the final FEM with the optimized model simulates the test in a satisfactory manner.

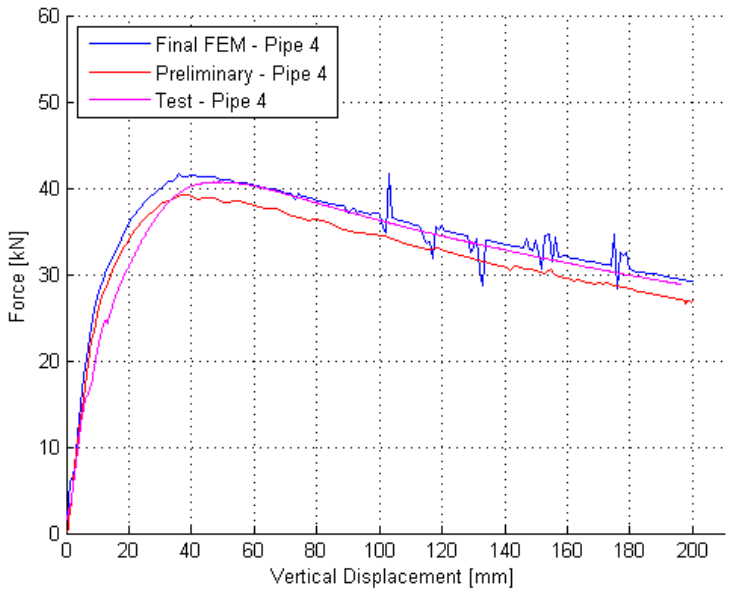

Figure 7.12: Force-displacement curves of numerical simulations compared with the test results of pipe 4.

In Figure 7.13, force-vertical displacement curves of the experimental test of pipe 5 are plotted with the corresponding optimized and preliminary numerical simulations. The numerical simulations are almost identical in the beginning. As the slope of the

preliminary simulation starts to decrease towards the peak force, the final numerical simulation and the test result rise to a higher peak force. After peak force the final and preliminary numerical simulations have an equal behaviour, but there is an approximately constant difference in the load level at a given displacement. It can be seen that the optimized simulation II captures the behaviour of test 5 much better than the preliminary numerical simulation.

The peak force of simulation II is 44.8 kN which is 2.4 % lower than the peak force of test 5 of 45.9 kN. Beside the small deviation in peak force, which is insignificant, the curves are almost identical, and there is only a slight difference between the results. This means that the changes made on basis of the parameter studies and the actual testing parameters were successful and the final FEM with the optimized model simulates the test in a satisfactory manner.

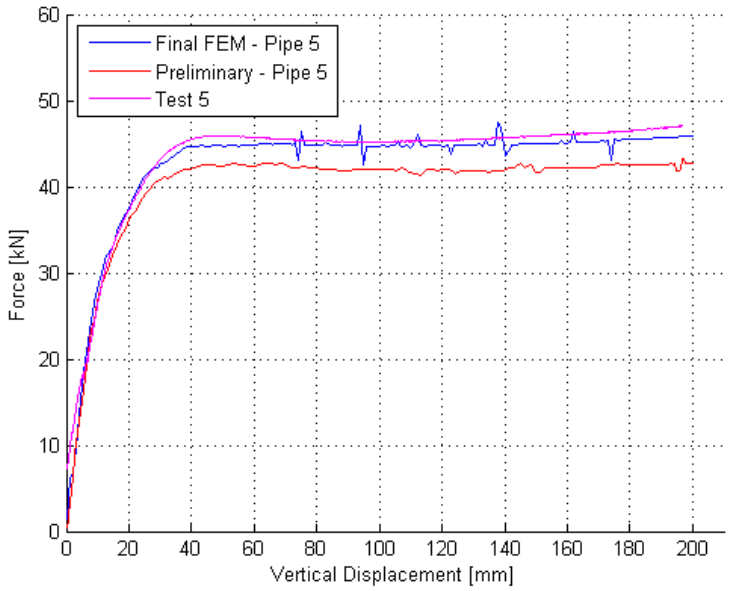

Figure 7.13: Force-displacement curves of numerical simulations compared with the test results of pipe 5.

Force-vertical displacement curves of the experimental test of pipe 6 plotted with the corresponding optimized and preliminary numerical simulations can be seen in Figure 7.14. The numerical simulations have a slightly higher initial stiffness than the experimental test. The preliminary and final numerical simulation are almost identical up to the peak force. After peak force they start to deviate and this continues until final deformation is reached. It can be seen that the optimized simulation III captures the behaviour of the test 6 better than the preliminary numerical simulation. This applies from the peak force.

The peak force of simulation III is 40.3 kN which is 0.7 % lower than the peak force of test 6 of 40.6 kN. This is an insignificant difference and the curves are almost

identical except for the last part of the deformation range where a little deviation can be seen. The final FEM with the optimized model simulates the test in a highly satisfactory manner meaning that the changes made on basis of the parameter studies and the actual testing parameters improved the numerical results.

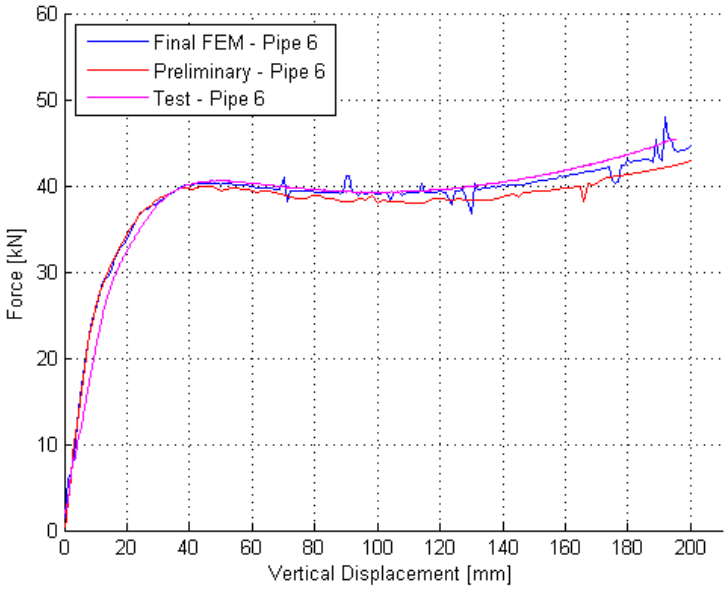

Figure 7.14: Force-displacement curves of numerical simulations compared with the test results of pipe 6.

In Table 7.4 there is an overview of peak forces from the preliminary and final numerical simulations and the experimental tests. The percentage difference in peak forces compared to the peak force of the test is also presented.

Table 7.4: Overview and differences of peak forces for preliminary and final numerical simluations compared with the experimental test.

	Pipe 4		Pipe 5		Pipe 6	
	Peak force [kN]	Difference	Peak force [kN]	Difference	Peak force [kN]	Difference
Test	40.7	-	45.9	-	40.6	-
Preliminary	41.4	3.7 %	42.7	7.0 %	39.9	1.7 %
Final	39.2	1.7 %	44.8	2.4 %	40.3	0.7 %

The equivalent plastic strain ε^p_{eq} is an indicator for where fracture will initiate. It is therefore of high interest to see how it will evolve during the bending of the pipe and where the maximum value will occur.

For the numerical simulations the highest ε^p_{eq} was observed in an element along the cross-section in the middle of the pipe, on the outer surface. This was identical for all the three numerical simulations. The plastic equivalent strain for the bending step has therefore been plotted for some elements, including the element with highest ε^p_{eq}, along

this edge. Then the evolution of the plastic strain can be studied. In Figure 7.15 the edge of the mid cross-section of the pipe containing the studied elements can be seen. For better visibility only one-half of the pipe is shown.

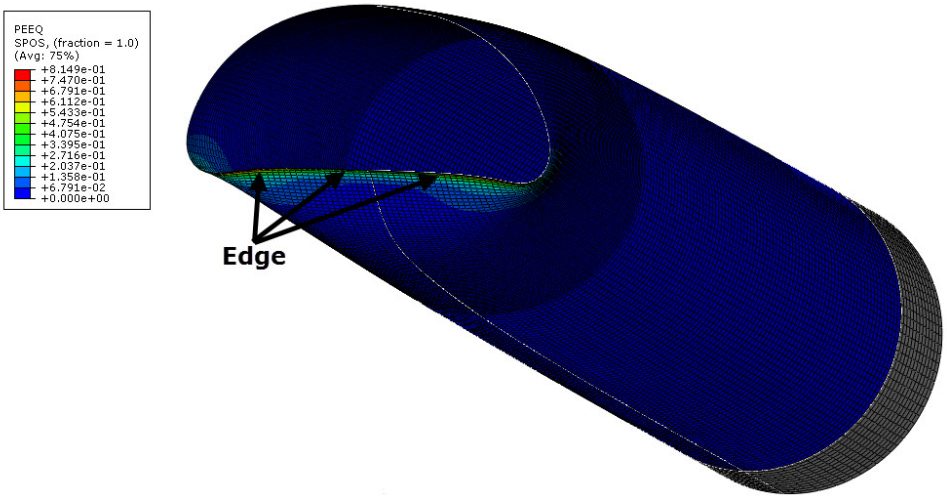

Figure 7.15: Figure of pipe 6 showing the edge of the midpoint cross-section, on the outer surface, where the equivalent plastic strain were taken from.

In Figure 7.16a, Figure 7.17a and Figure 7.18a the chosen elements in pipe 4, 5 and 6 can be seen, respectively, with the ε_{eq}^{p} at outer surface plotted at the final deformation. The evolution of the ε_{eq}^{p} for the selected elements in the pipes can be seen in Figure 7.16b, Figure 7.17b and Figure 7.18b, where they have been plotted for the bending step. It can be seen that the elements are situated at almost the same places in the pipes, to make a comparison between the ε_{eq}^{p} valid. The same behaviour for all three ε_{eq}^{p} plots can be observed. In the beginning of the deformation, the element which is closest to the bottom of the pipe (the point that the indenter comes in contact with first) has the highest ε_{eq}^{p}. Then, as the deformation continues, the following element, e.g. element 11713 and 11719 for pipe 4 has the highest ε_{eq}^{p}. When the final deformation is reached, the element that is second farthest away from the bottom of the pipe, e.g. element 11728 for pipe 4, that has the highest value. The element highest up on the pipe wall have a different shape on the ε_{eq}^{p} curve with a steady increase in ε_{eq}^{p}, up to a ε_{eq}^{p} value that are lower than for the other elements. This can e.g. be seen for element 11728 in pipe 4.

This shows that the localization of the ε_{eq}^{p} starts at the bottom of the pipe where the indenter first hits the pipe and then translates towards the sides of the pipe as the bending takes place and the cross-section goes from an undeformed to a deformed shape. This can be seen as a plastic hinge that travels along the cross-section.

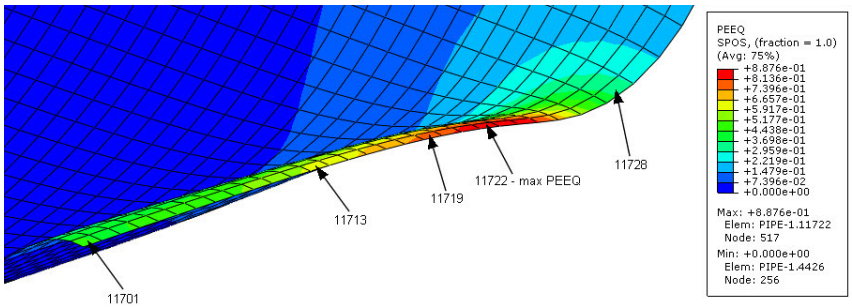

(a) Selected elements with equivalent plastic strain at final deformation.

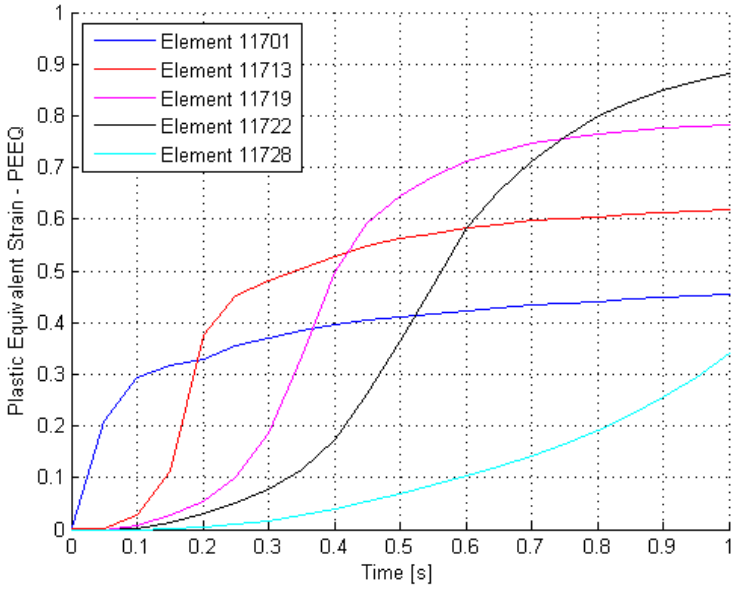

(b) Evolution of plastic equivalent strains for selected elements.

Figure 7.16: Equivalent plastic strains at outer surface for simulation I - pipe 4.

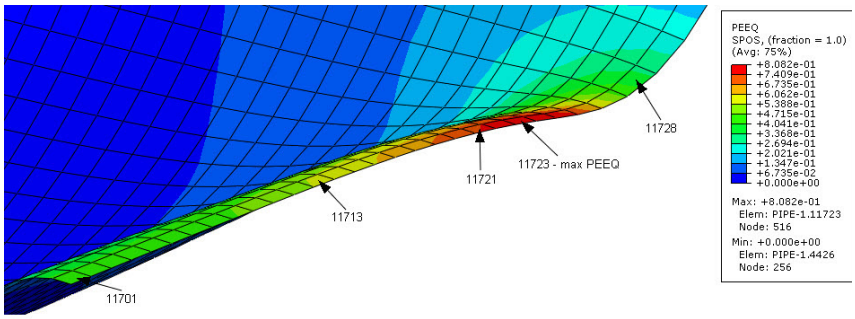

(a) Selected elements with equivalent plastic strain at final deformation.

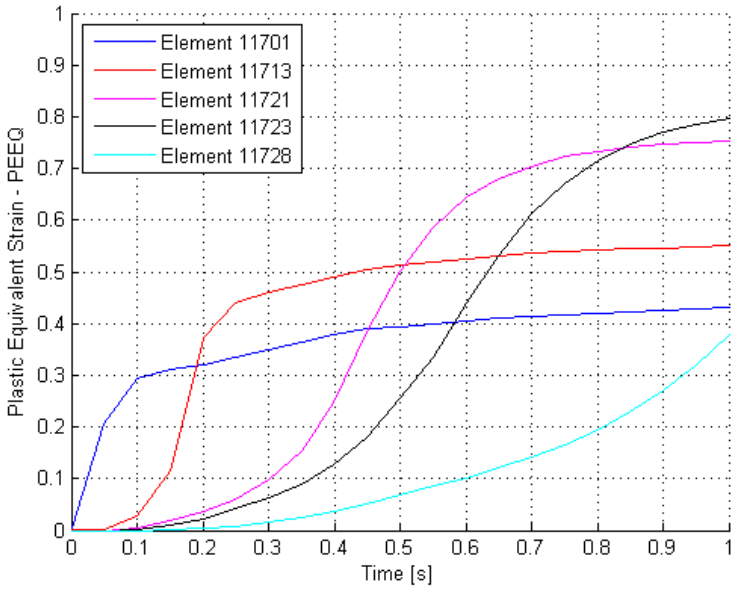

(b) Evolution of plastic equivalent strains for selected elements.

Figure 7.17: Equivalent plastic strains at outer surface for simulation II - pipe 5.

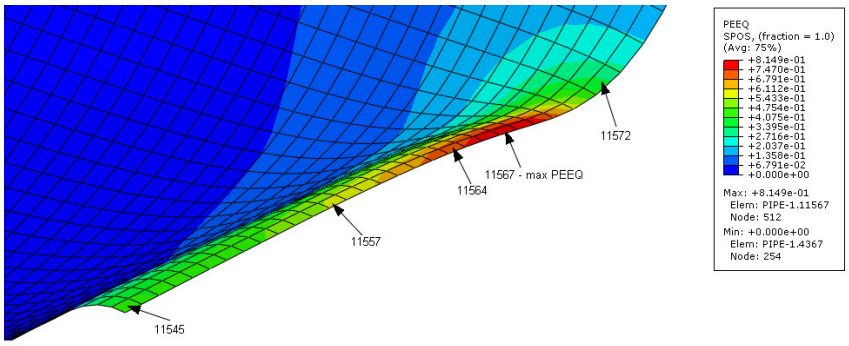

(a) Selected elements with equivalent plastic strain at final deformation.

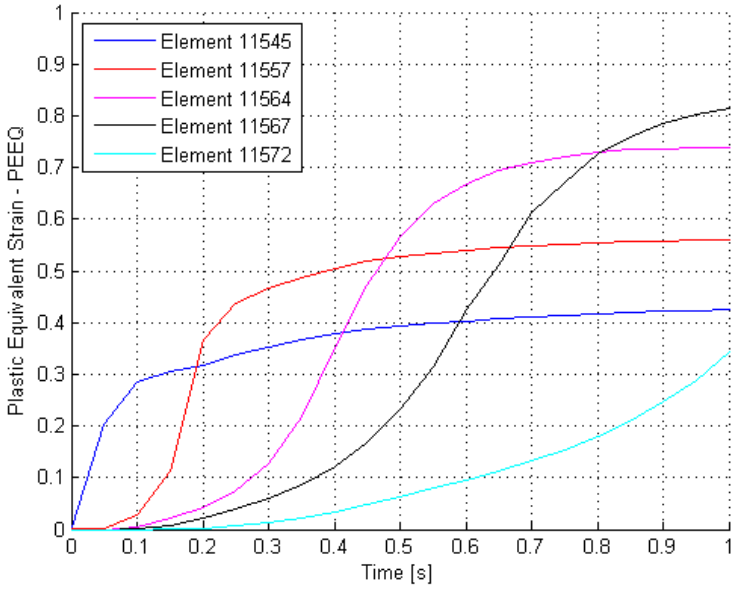

(b) Evolution of plastic equivalent strains for selected elements.

Figure 7.18: Equivalent plastic strains at outer surface for simulation III - pipe 6.

Figure 7.19 and Figure 7.20 shows a comparison of equivalent plastic strains between DIC and numerical simulations for pipe 5 and 6, respectively. No results have been obtained for pipe 4, as the images were insufficient due to experimental issues with the cameras. It can be seen that it is a reasonably well match between the strains obtained from the numerical simulations and DIC. DIC is also able to capture how the strains are distributed in a decent way, especially for pipe 6. It should be noted that there is some shadow in the pictures, making it a bit difficult to see the contours of the pipes.

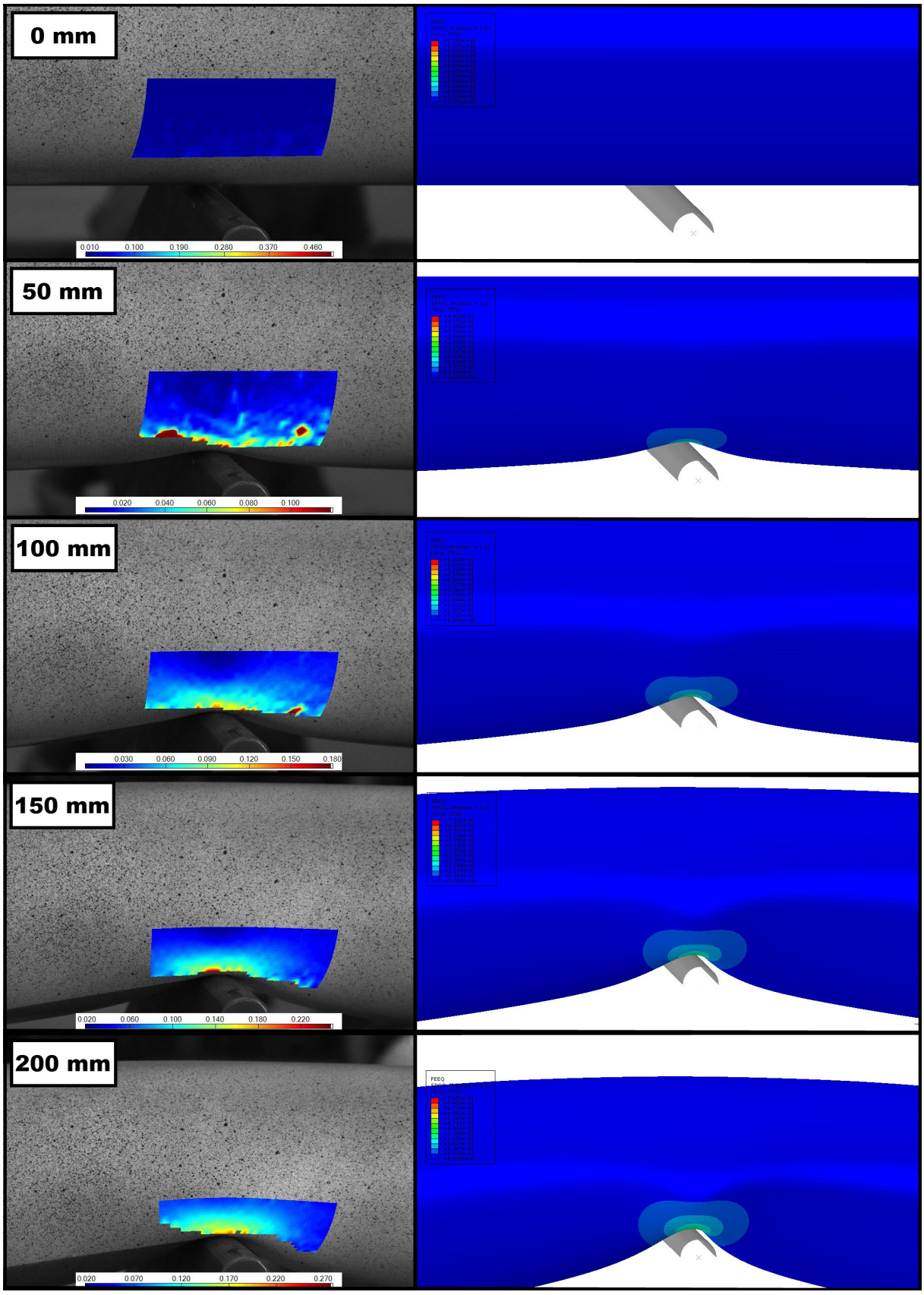

Figure 7.19: Equivalent plastic strains from DIC and numerical simulations obtained at different deformation levels for pipe 5.

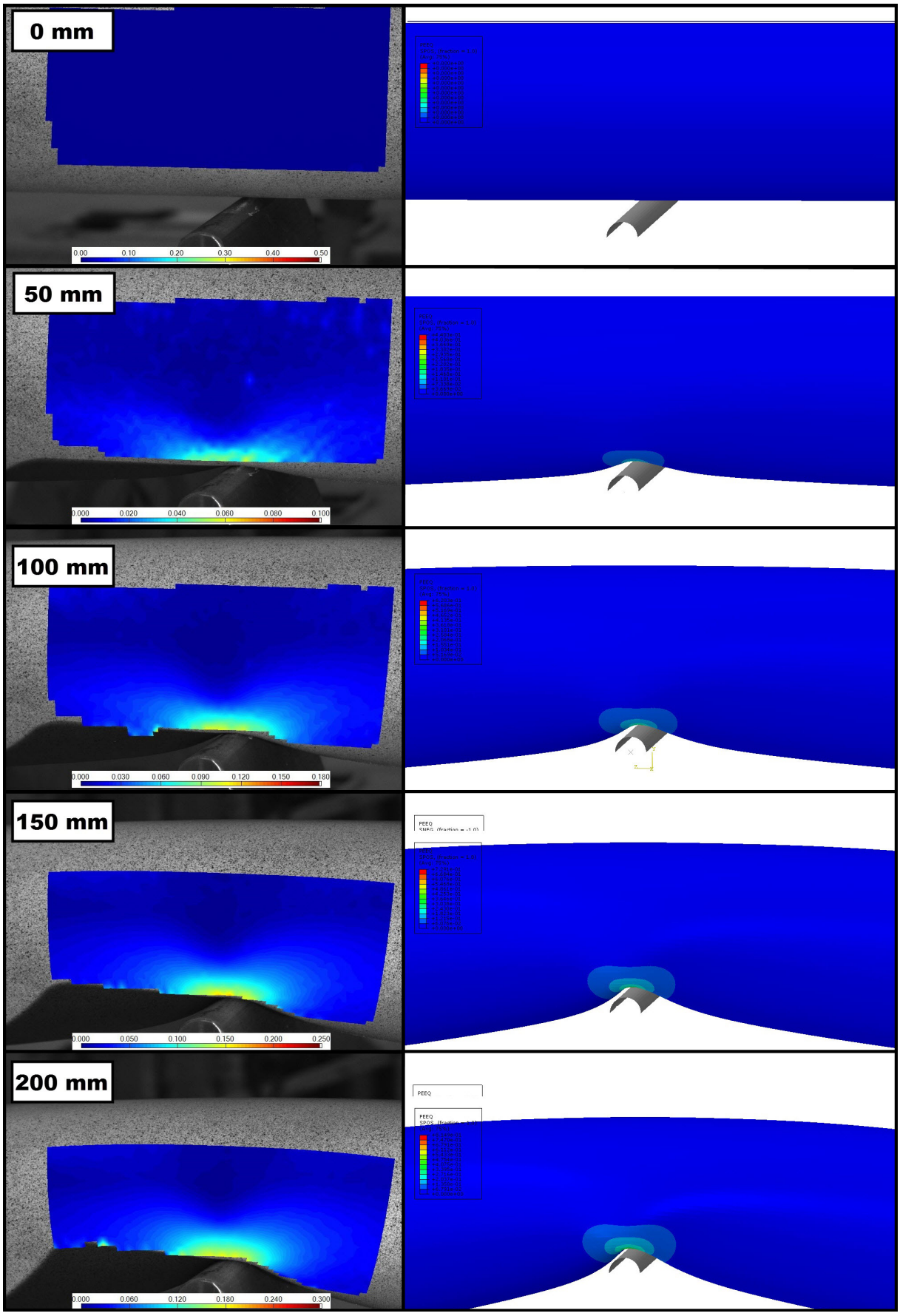

Figure 7.20: Equivalent plastic strains from DIC and numerical simulations obtained at different deformation levels for pipe 6.

Chapter 8

Discussion

Preliminary numerical simulations were performed to get a sense of how the experiments in the stretch bending rig would behave. The simulations were carried out with and without inner pressure applied to the pipes. Some of the results from the preliminary simulations can be seen in Figure 8.1.

The peak force of the simulations with linear increasing load and no horizontal load applied are approximately equal with a value of 39.9 kN and 39.2 kN, respectively. The simulation with constant horizontal load has a peak force of 42.7 kN, which is 7.0 $\%$ and 8.9 $\%$ higher than the peak forces of the simulations with linear increasing and no horizontal load applied, respectively. At the end of deformation, the simulation with constant horizontal load has the same vertical force as the linear increasing load. This is expected since the horizontal load is equal at the end of deformation. These observations are the same for both simulations with and without applied pressure. The difference is that the simulations with inner pressure have approximately 21 $\%$ higher peak forces than the corresponding simulations without inner pressure, which is significant. As shown in the preliminary numerical simulations, the cross-section of a pressurized pipe will deform less than for a non-pressurized pipe. This will maintain a larger 2nd moment of area, which makes a larger force needed for a given deformation.

For the pressurized pipes the simulation with linear increasing and no load applied, have peak forces of 48.5 kN and 47.5 kN, respectively. The simulation with constant horizontal load has a peak force of 51.5 kN, which is respectively 6.2 $\%$ and 8.4 $\%$ higher than the peak forces of the simulations with linear increasing and no horizontal load applied.

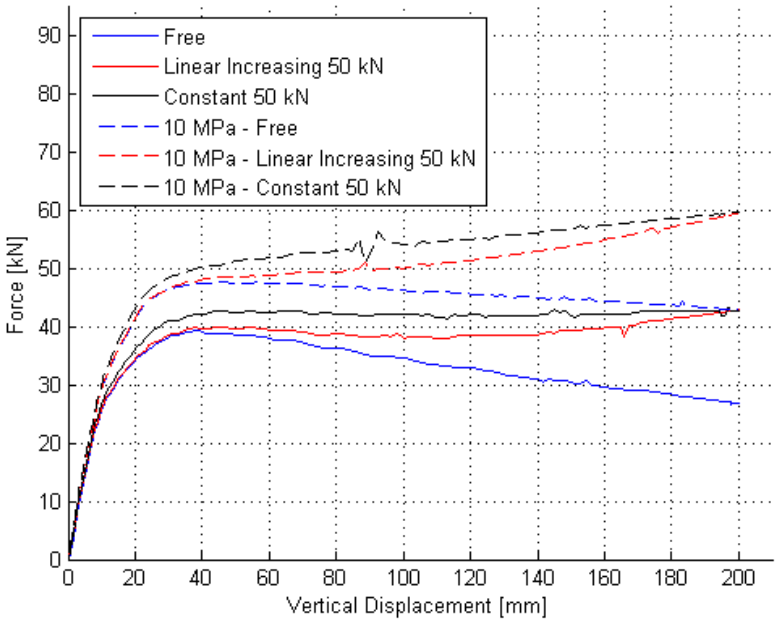

Figure 8.1: Force-vertical displacement plots of preliminary simulations with and without inner pressure.

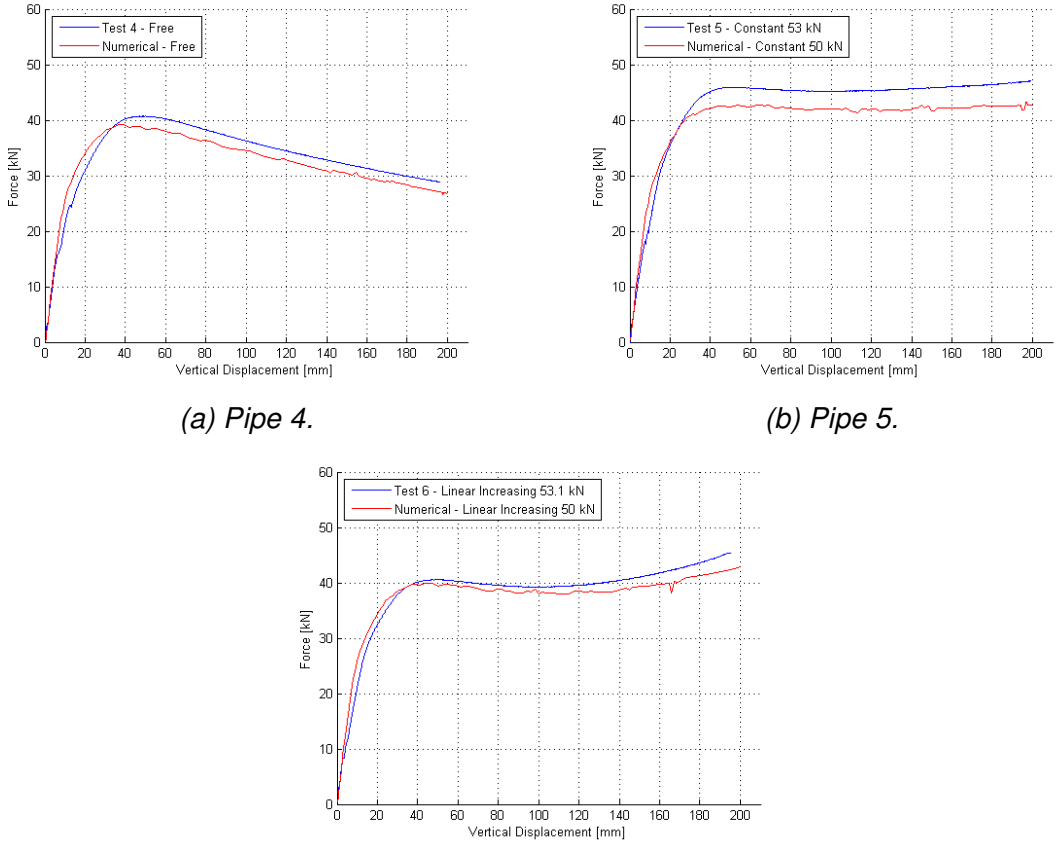

(a) Pipe 4.

(b) Pipe 5.

(c) Pipe 6.

Figure 8.2: Force-vertical displacement plots of the preliminary numerical simulations and the experimental test.

Figure 8.2 shows the experimental results from pipes 4-6 compared with their corresponding preliminary numerical simulation. It can be observed that there is in overall, a good similarity between the force-vertical displacement curves from the simulations and experiments. The behaviour of the numerical simulations after peak force is in very good agreement with the experiments. This shows that the numerical model captures the pipes' behaviour in a satisfying manner.

To improve the results from the preliminary numerical simulations, parametric studies were conducted. It was primarily the thickness of the pipe that proved to affect the results significantly, while the equivalent plastic strain was highly dependent on the element size.

When it comes to the thickness of the pipe, the average measured thickness does not necessarily represent the true average thickness, and there can be a high variance in the thickness over the length of the pipe. As the bending of the cross-section is local and most of the pipe exhibit only rigid-body motion, it is the thickness at the midpoint of the pipe that really affect the global response. As the thickness has shown to vary a lot over the length of the pipe it should be of interest to model the pipe with a function that describes the thickness field, in particular at the midpoint of the pipe in a better way than using the average measured thickness.

For the equivalent plastic strain it could be of interest to model a shell model and use a fine mesh in the midpart of the pipe, as done in the final numerical simulations in this thesis. This would probably make the equivalent plastic strain results better, and the modeling of a possible fracture more precise.

Final numerical simulations numbered I-III were carried out on optimized models, one for each of the experiment on pipes 4-6.

A comparison between the preliminary and final numerical simulation and the experimental test on each pipe can be seen in Figure 8.4. It can be observed that the final numerical simulations represents the experimental results better than the corresponding preliminary simulation. This is mainly because of the thickness adjustment and the use of the exact horizontal loads that were applied in the experiments.

Simulation I on pipe 4 seen in Figure 8.3a has higher initial stiffness than the experimental result. This is also to a certain degree the case of simulation III on pipe 6. This is probably due to local buckling in the pipe not captured by the shell model or issues with the experimental setup during the test. The difference in the peak forces are insignificant with a maximum deviation of 2.4 $\%$ for simulation II on pipe 5.

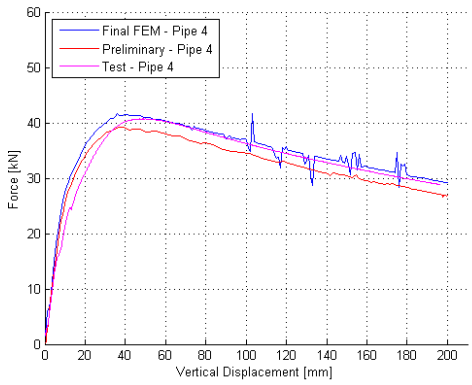

(a) Simulation I - pipe 4.

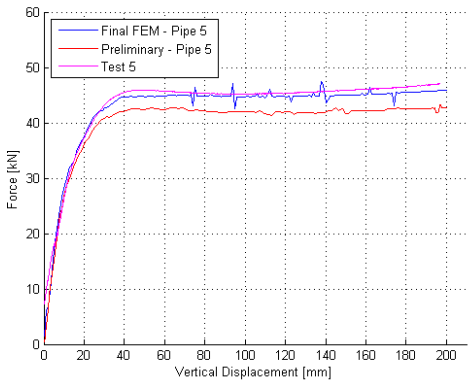

(b) Simulation II - pipe 5.

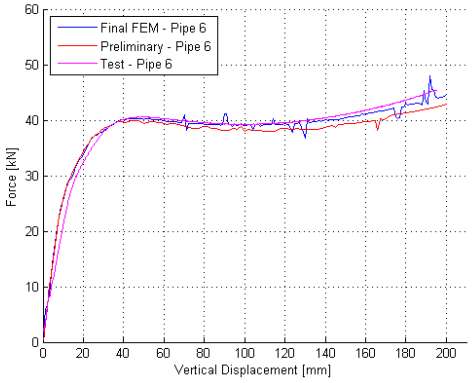

(c) Simulation III - pipe 6.

Figure 8.3: Force-vertical displacement curves of the final numerical simulations compared with the experimental test results.

Slåttedalen and Ørmen [3] conducted dynamic impact tests on pipe A and B with velocities of 3.24 m/s and 5.13 m/s, respectively, see Section 3.3.1 for more details about the tests. An experiment similar to the one performed in this thesis on pipe 4 was carried out by Asheim and Mogstad [6] on pipe 1. The force-displacement curves from these experiments and a nondimensional plot can be seen in Figure 8.4a and Figure 8.4b, respectively.

As seen, it is a very good global correlation between pipe 1 and 4, deformed quasi-statically, and between pipe A and B, deformed dynamically. The peak force of the dynamic and quasi-static tests, are approximately $70\ kN$ and $40\ kN$, respectively. The reason for a higher peak force in the dynamic tests compared to the quasi-static tests, is mainly due to a shorter span of the pipes, increasing the plastic bending capacity. Two other contributions to the difference in peak force is strain-rate sensitivity and inertia forces. Slåttedalen and Ørmen [3] carried out dynamic tensile tests, see Section 3.1.2, which showed that the material is strain-rate sensitive.

To make the comparison of the dynamic and quasi-static results independent of specimen length and thickness, nondimensional plots are shown in Figure 8.4b. The nondi-

mensional plots shows the force divided by the plastic bending capacity, see Section 5.2.2, plotted against the displacement divided by the thickness. The values have been calculated individually for each pipe by use of measured values e.g. the average pipe thickness. Here it can be seen that the quasi-static result are higher than the dynamic results, which was not expected. The strain-rate sensitivity was believed to make the dynamic result higher, as this will increase the strength of the material, when compared with a quasi-static analysis. It is believed that the unexpected result is due to different modes of deformation, as a dynamic bending of specimen can give a totally different deformation mode than a quasi-static bending.

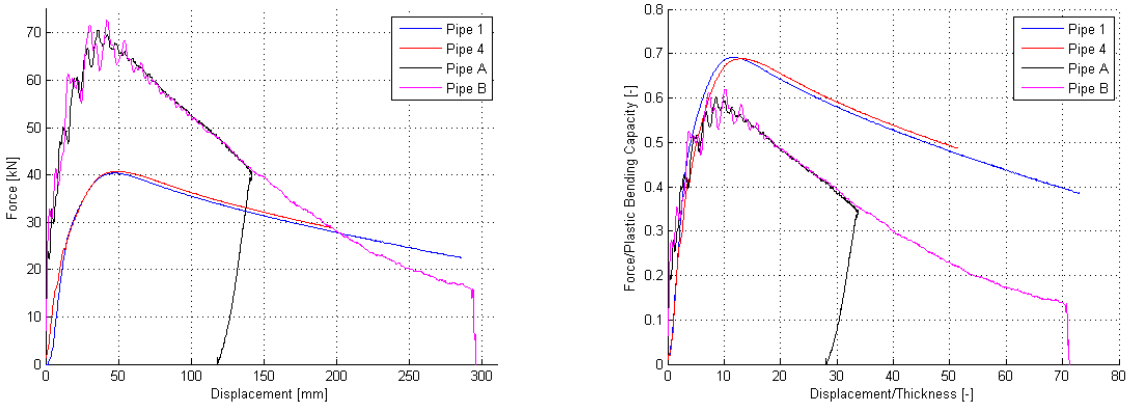

(a) Force-vertical displacement. *(b) Non-dimensional.*

Figure 8.4: Experimental dynamic and quasi-static bending of pipes.

In Table 8.1 an overview of the peak forces and the nondimensional results can be seen.

Table 8.1: An overview of the peak forces and plastic bending capacity of pipe A, B, 1 and 4. The peak force has been normalized by dividing it by the plastic bending capacity of the pipes.

Pipe	**A**	**B**	**1**	**4**
Peak force (pf) [kN]	70.7	72.5	40.4	40.7
Plastic bending capacity (pbc) [kN]	117.47	116.95	58.41	59.15
pf/pbc [-]	0.6	0.62	0.69	0.69
Normalized	0.87	0.90	1	1

The evolution of the elements with the maximum equivalent plastic strain (ε^p_{eq}) values when the final deformation is reached has been plotted in Figure 8.5 and the maximum values of ε^p_{eq} are presented in Table 8.2. These three elements are situated at approximately the same place in the pipes.

For all three simulations the curves of the element with maximum ε^p_{eq} are similar to eachother. There is a slight increase in the beginning, then there is a rapid increase in the

ε^p_{eq} before the slope decreases when the final deformation is approaching. Simulation I, the pipe with no horizontal load applied, has the highest ε^p_{eq} value of 0.8876. Simulation II and III have a maximum ε^p_{eq} of 0.8082 and 0.8149, respectively. When compared with simulation I, this is 8.9 $\%$ and 8.2 $\%$ lower. A lower ε^p_{eq} may reduce the possibility or give no initiation of fracture, but it is not possible to conclude, as the initiation of fracture also depends on the stress state.

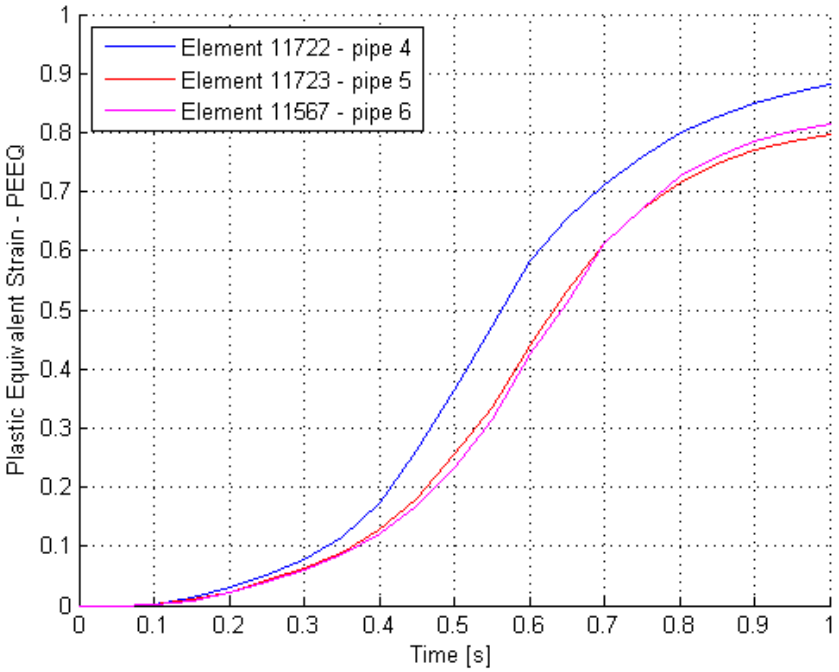

Figure 8.5: Critical elements regarding equivalent plastic strains in the pipes.

Table 8.2: Overview of maximum plastic strains in critical elements.

Simulation	I	II	III
Max ε^p_{eq}	0.8876	0.8082	0.8149
Difference	-	8.9 $\%$	8.2 $\%$

In Figure 8.6, the development of the plastic equivalent strain has been plotted for different deformation levels. A cut has been made in the numerical model, by removing the upper half of the pipe, making it possible to see the bottom of the pipe from the inside. It should be noted that the strains are taken from the outer surface. It can be seen that two plastic hinges develope, symmetric about the longitudinal axis, when the pipe deforms. This is where the maximum plastic strains are during deformation, and a clearer view of the progress of plastic strains is obtained. As seen in the previous work there is a good correlation of where fracture and cracks have been observed and where in the pipe the maximum plastic strains are.

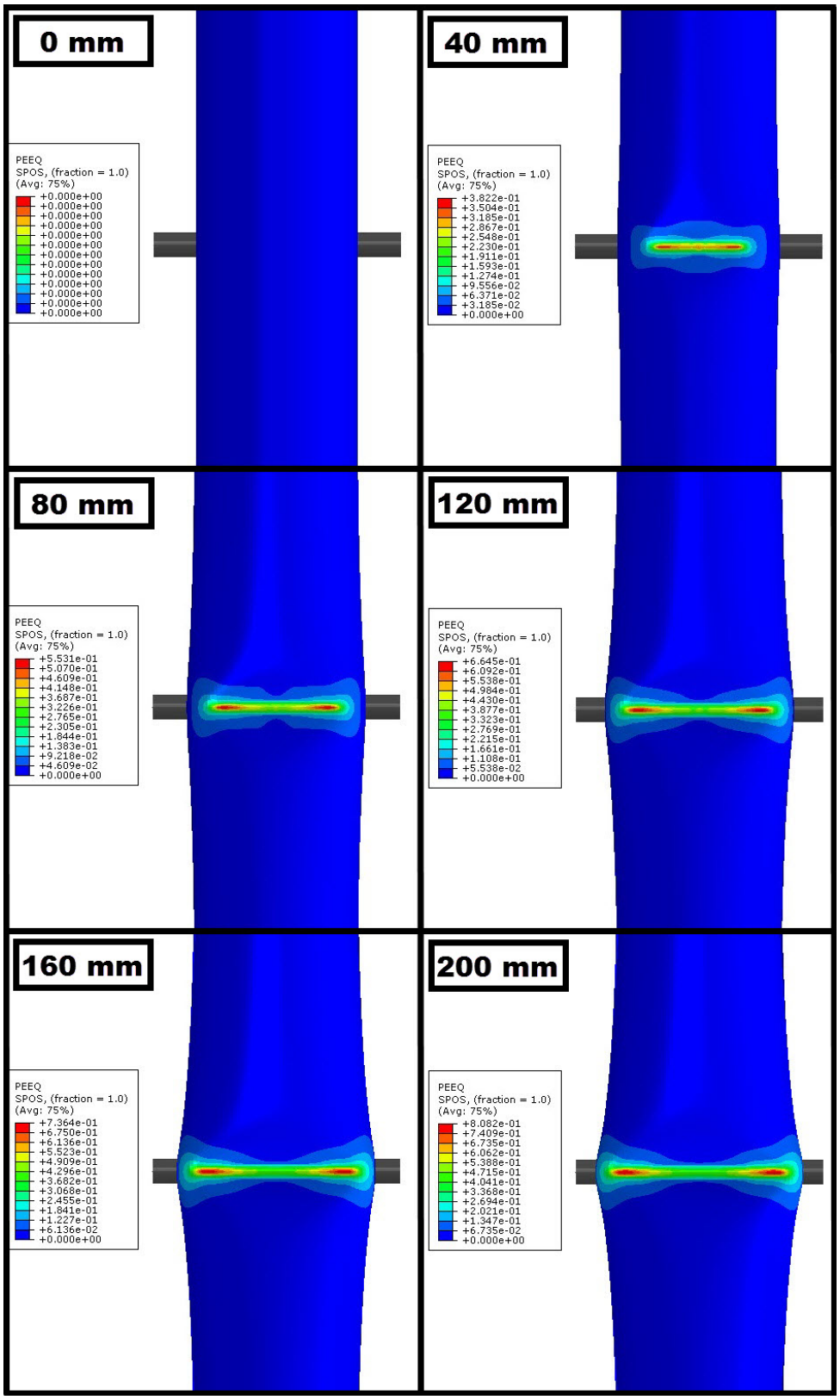

Figure 8.6: Plastic hinges at different deformation levels in pipe 5.

The pipes that are simulated will in real life have a fluid, e.g. oil streaming inside, which creates an inner pressure. It is therefore very interesting to see how inner pressure will affect the deformation and stretching of the pipe. Since there is a very good fit

between the experimental and numerical simulations, regarding global response, for pipes without pressure, it is believed that the preliminary numerical simulations with inner pressure should give an reasonable indication of the global response for the pressurized pipes.

In Figure 8.1, the results from the preliminary simulations, including the one with inner pressure, can be seen. The curves for the simulations with inner pressure are quite similar to the one without pressure, but they have, in general a higher force level. As mentioned, the differences in peak forces are approximately 21 % higher, for the pressurized pipes when compared to pipes with no inner pressure. This is very reasonable, as the inner pressure will give more resistance to bending, i.e. a higher force is needed to deform the pipes to the same deformation.

As for pipes without inner pressure the plastic strains gives an indication of where fracture will occure first. In Table 8.3, an overview of the equivalent from the preliminary numerical studies can be seen. The ε_{eq}^{p} have also been compared, where the ε_{eq}^{p} of the free pipe, simulation 1, has been used as a basis. It can be seen that the plastic strains of the pressurized pipes are lower than the plastic strains for the non-pressurized pipes. This indicates that it is important to do experimental testing of pressurized pipes as plastic strain is an very important parameter for fracture.

Table 8.3: Comparison of the equivalent plastic strains in the preliminary simulations with and without inner pressure.

Load	Free		C 50 kN		LI 50 kN	
Simulation	1	6	2	7	4	8
Pressure [MPa]	-	10	-	10	-	10
Max ε_{eq}^{p}	0.8626	0.7079	0.8419	0.6973	0.8129	0.6916
Difference	-	17.9 %	2.4 %	19.1 %	5.8 %	19.8 %

Chapter 9

Conclusion

The most important observations in this thesis are listed below.

- The experimental testing was performed in a satisfying manner. The only minor difference compared to the initially planned experiments, was a slightly higher applied horizontal load level for pipe 5 and 6.
- When comparing force-displacement plots, it can be seen that the final numerical simulations captured the global behaviour of its corresponding experiment in a highly satisfactory manner, which validates the numerical model.
- A parameter study showed that the global response is highly dependent on the pipe thickness and that the local plastic strain is highly dependent on the element size.
- Equivalent plastic strain is an important parameter for initiation of fracture in ductile materials. It was seen that the equivalent plastic strain localized in the contact area between the indenter and pipe, indicating fracture will occure here. This is supported by the work in previous thesis.
- The DIC measurements gave decent results when comparing the plastic strains with the ones from the final numerical simulations.

Chapter 10

Further work

This chapter presents suggested further work on the topic of this theses. The suggestions are as follows:

- Conduct metallurgical investigations of pipe 4-6, mainly to see if fracture is initiated.
- Carry out quasi-static testing of pressurized pipes with the same load procedure as suggested herein. This allows direct comparison with and without pressure.
- See how a surrounding fluid will interact with the pipe and what affections that might have, when bending the pipe. This could be done by looking into a fluid structure interaction (FSI) analysis.
- Establish a procedure to utilize DIC, during experimental testing, in a best possible way. Both to be able to measure, mainly strains, without the necessity of numerical simulations, and to be able to validate numerical simulations against DIC.
- Use micro-mechanical modeling to calibrate a macroscopic fracture criteria.
- Look more closely at how to model the pipe's thickness more precisely, e.g by using a thickness field. This is especially important for the middle part of the pipe where the deformation occurs when bending the pipe, as the global response is highly affected by the thickness.
- Use FSI to model pressure and compare to a uniformly distributed load and validate against experimental testing.
- Include kinematic hardening in the material model.
- Look more into a dimensional analysis of the pipes, as this will assure that pipes with e.g. different lengths and thicknesses can be compared to eachother. This is

highly relevant for comparison of dynamic impacted and quasi-statically deformed pipes.

Bibliography

[1] Statoil. *Annual Report 2008 Operations North Sea*. Statoil `http://www.statoil.com/AnnualReport2008/en/CountrySpotlight/Norway/Pages/3-1-7-1_OperationsNorthSea.aspx`, Cited date: [04.09.2013].

[2] Petroleumstilsynet v/Rune Solheim. *Presentasjon sikkerhetsforum 29.11.2007 alvorlige hendelser*. Petroleumstilsynet, `http://www.ptil.no/getfile.php/Tilsyn%20p%C3%A5%20nettet/vrige/5_07_siforum_alvorlige_hendelser.pdf`, Cited date: [04.09.2013].

[3] K. Slåttedalen and A. Ørmen. *Impact Against Offshore Pipelines*. Master thesis, Norwegian University of Science and Technology, 2010.

[4] J. Fornes and S. Gabrielsen. *Impact Against Offshore Pipelines*. Master thesis, Norwegian University of Science and Technology, 2011.

[5] V. Aune and M. Hovdelien. *Impact Against Offshore Pipelines*. Master thesis, Norwegian University of Science and Technology, 2012.

[6] T. Asheim and I. Mogstad. *Impact Against Offshore Pipelines*. Master thesis, Norwegian University of Science and Technology, 2013.

[7] O.S. Hopperstad and T. Børvik. *Lecture Notes in TKT4135 Mechanics of Materials*. Department of Structural Engineering, Norwegian University of Science and Technology, 2012.

[8] S.G. Thomas, S.R. Reid, and W. Johnson. *Large deformations of thin-walled circular tubes under transverse loading - I*. International Journal of Mechanical Science, Vol.18, page 325-333, 1976.

[9] M. Langseth and A.G. Hansen. *Lecture Notes on Crashworthiness of Aluminium Structures*. Structural Impact Laboratory, Department of Structural Engineering, Norwegian University of Science and Technology, 2002.

[10] G.E. Dieter. *Bend, and Shear Testing Mechanical Behavior Under Tensile and Compressive Loads*. ASM Handbook: Mechanical Testing and Evaluation, 8:99-108 edition, 2000.

[11] M. Kristoffersen, T. Børvik, I. Westermann, M. Langseth, and O.S. Hopperstad. *Impact against X65 steel pipes - An experimental investigation*. 2013.

[12] G.R. Johnson and W.H. Cook. *A Constitutive Model and Data for Metals Subjected to Large Strains, High Strain Rates and High Temperatures*. Proceedings of the 7th International Symposium on Ballsistics, Hague, 1983.

[13] G.R. Johnson and W.H. Cook. *Fracture Characteristics of Three Metals Subjected to Various Strains, Strain Rates, Temperatures and Pressures*. Proceedings of the 7th International Symposium on Ballsistics, Hague, 1983.

[14] A.G. Hansen, T. Auestad, T. Tryland, and M. Langseth. *The Kicking Machine: A Device for Impact Testing of Structural Components*. International Journal of Crashworthiness, 8 (4):385-392 edition, 2003.

[15] Det Norske Veritas. *Interference between Trawl Gear and Pipelines*. *DNV-RP-F111. DNV*, 2010.

[16] Structural Impact Laboratory. *Simlab Metal Model Theory Manual*. Structural Impact Laboratory, Department of Structural Engineering, Norwegian University of Science and Technology, rev 10.05.13 edition, 2013.

[17] SIMULIA. *Abaqus Analysis Users Manual*. SMULIA, Abaqus Documentation Collection, 6.11 edition, 2013.

[18] Properties of steel grade x65. `http://www.ehow.com/list_7492075_properties-steel-grade-x65.html`. Cited date: [November 2013].

[19] A.H. Clausen, O.S. Hopperstad, and M. Langseth. *Stretch Bending Rig. Experimental Set-Up*. Report R-9-96, Department of Structural Engineering, Norwegian University of Science and Technology, 1996. revised 1999.

[20] A. Manes. *The Behaviour of an Offshore Steel Pipeline Subjected to Bending and Stretching*. Structural Impact Laboratory, Department of Structural Engineering, Norwegian University of Science and Technology, Politecnico di Milano, Department of Mechanical Engineering, 2009.

[21] Plastic section modulus. `http://en.wikipedia.org/wiki/Section_modulus`. Cited date: [October 2013].

[22] Quasi-static analyses. `http://imechanica.org/files/l5-quasi-static.pdf`. Cited date: [December 2013].

[23] E. Fagerholt, T. Børvik, and O.S. Hopperstad. *Measuring Discontinuous Displacement Fields in Cracked Specimens Using Digital Image Correlation with Mesh Adaptation and Crack-Path Optimization*. Structural Impact Laboratory, Depart-

ment of Structural Engineering, Norwegian University of Science and Technology, 2012.

[24] E. Fagerholt, E. Østby, T. Børvik, and O.S. Hopperstad. *Investigation of Fracture in Small-Scale SENT Tests of a Welded X80 Pipeline Steel Using Digital Image Correlation with Node Splitting*. Structural Impact Laboratory, Department of Structural Engineering, Norwegian University of Science and Technology, 2012.

[25] Coefficient of friction. `http://www.engineershandbook.com/Tables/frictioncoefficients.htm`. Cited date: [October 2013].

Appendices

Appendix A

Pipe Measurements

The following appendix contains all measurements of the thicknesses and inner diameters of pipe 4-6. The thickness measurements are found in Table A.1a for pipe 4, Table A.2a for pipe 5 and in Table A.3a for pipe 6. The average thickness, variance and standard deviation are found in Table A.1b for pipe 4, Table A.2b for pipe 5 and in Table A.3b for pipe 6. In Table A.4 the measurements of the inner diameters of the pipes can be seen. The average inner diameter, variance and standard deviation can be seen in Table A.5.

The abbreviations used in the tables are avg - average, var - variance and st.dev - standard deviation.

Pipe 4					
Position	1	2	3	4	5
N	4.08	3.98	3.92	4.10	4.17
N-E	4.62	4.48	4.35	4.28	4.46
E	4.45	4.39	4.12	4.10	4.33
S-E	4.46	4.48	4.42	4.21	4.26
S	4.11	4.32	4.26	4.17	4.01
S-W	3.99	4.12	4.30	4.19	3.99
W	3.80	3.83	4.01	4.12	4.01
N-W	4.08	3.99	4.08	4.30	4.32

(a) Thickness measurements in mm.

Pipe 4	
t_{avg}[mm]	4.19
Var(t)[mm^2]	0.0368
St.dev(t)[mm]	0.1918

(b) Average thickness, variance and standard deviation.

Table A.1: Pipe 4.

Pipe 5						
Position	1	2	3	4	5	x
N	4.66	4.66	4.48	4.35	4.39	4.21
N-E	4.30	4.47	4.39	4.30	4.19	3.95
E	4.04	4.17	4.30	4.21	4.08	3.81
S-E	3.69	3.86	3.97	4.06	3.90	3.71
S	3.91	3.86	4.06	4.15	4.21	3.92
S-W	3.89	3.69	3.74	3.9	4.07	3.92
W	4.48	4.19	4.24	4.28	4.48	4.30
N-W	4.63	4.44	4.24	4.20	4.37	4.22

(a) Thickness measurements in mm. x is extra measurements

Pipe 5		
	without x	with x
t_{avg}[mm]	4.19	4.16
Var(t)[mm^2]	0.0652	0.0656
St.dev(t)[mm]	0.2553	0.2560

(b) Average thickness, variance and standard deviation.

Table A.2: Pipe 5.

Pipe 6					
Position	1	2	3	4	5
N	4.08	4.17	4.29	4.39	4.46
N-E	4.04	3.86	3.95	4.15	4.26
E	4.46	4.12	4.08	4.08	4.21
S-E	4.08	3.95	3.69	3.63	3.86
S	4.08	4.05	4.01	3.78	3.86
S-W	3.72	3.89	3.78	3.68	3.70
W	4.08	4.26	4.39	4.38	4.12
N-W	3.88	4.05	4.21	4.35	4.21

(a) Thickness measurements in mm.

Pipe 6	
t_{avg}[mm]	4.06
Var(t)[mm^2]	0.0508
St.dev(t)[mm]	0.2253

(b) Average thickness, variance and standard deviation.

Table A.3: Pipe 6.

Pipe	4*		5		6	
End	1	2	1	2	1	2
N-S	-	-	122.21	122.24	122	122.06
E-W	-	-	122.42	122.39	122.08	122.26
NE-SW	-	-	122.52	122.56	121.84	122.56
NW-SE	-	-	122.41	122.56	122.51	122.27

*Table A.4: Measurements of the inner diameter of the pipes in mm. * not able to measure.*

Pipe	4*	5	6
D_{avg} [mm]	-	122.41	122.20
Var(D)[mm^2]	-	0.0158	0.0547
St.dev(D)[mm]	-	0.1260	0.2339

*Table A.5: Average inner diameter, variance and standard deviation. * not able to measure.*

Appendix B

Material Card

```
*Material, Name = x65
*Density
 7.85000e-9
*Include, input = depvar_SMM.inc
*User material, Constants = 23
**   EFLAG,  YFLAG,  RMAPFLAG,  HFLAG,  VFLAG,
       1,      1,       0,        1,      0,

**   TFLAG,   DFLAG,   SFLAG,   STFLAG,      E,
       0,       1,       0,        0,   2.08000e+05,

**   PR,           SIGMA0,       THETAR1,      QR1,       THETAR2,
    3.00000e-01, 4.65500e+02, 3.79500e+02, 6.27100e+02, 2.20700e+03,

**   QR2,         THETAR3,       QR3,         DINIT,        BETA0,
   1.27100e+02, 0.00000e+00,  0.00000e+00,  0.00000e+00,  0.00000e+00,

**   DCR,           s0,          Phi,        Gamma
   1.00000e+00, 1.59500e+03, 1.00000e+00, 1.00000e+00
```